Starbursts and active nuclei in galaxies

Dissertation

zur Erlangung des Doktorgrades
der Mathematisch-Naturwissenschaftlichen Fakultät
der Christian-Albrechts-Universität zu Kiel

vorgelegt von

Marvin Blank

Kiel, 2014

Erster Gutachter:	Prof. Dr. Wolfgang J. Duschl
Zweiter Gutachter:	Prof. Dr. Holger Kersten
Tag der mündlichen Prüfung:	01.12.2014
Zum Druck genehmigt:	01.12.2014

gez. Prof. Dr. Wolfgang J. Duschl, Dekan

Abstract: Starbursts and active nuclei in galaxies

Starbursts and active galactic nuclei (AGN) are predominantly driven by galaxy mergers, i.e., the collision of two galaxies, but isolated galaxies, e.g., our Milky Way, can also be subject to these phenomena. Therefore this thesis is divided into two parts: in part I we investigate starbursts and AGN due to galaxy mergers and in part II we examine the Galactic Center (GC), i.e., the center of our Milky Way.

In part I we will focus in particular on the timing of starbursts and AGN activity during a merger event. Recent observations indicate a time lag between these two phenomena in the sense that first the merger produces a starburst, followed by, after a time span of 200-300 million years, an episode of AGN activity. To explain this time lag we develop a scenario where the galaxies' gas, after having formed stars, first forms an accretion disk around the central black hole due to its angular momentum. The gas then loses its angular momentum due to viscous forces and is finally accreted by the black hole, causing the galactic nucleus to become active. Thus the observed time lag is related to the viscous timescale the gas needs, after having formed stars, to move through the accretion disk before reaching the black hole. We develop a new subgrid model to account for the gas forming an accretion disk and for the subsequent evolution of this disk. Our numerical simulations of galaxy mergers reproduce the observed time lag between starburst and AGN activity and fulfill further observational constraints, like the well known correlation between black hole mass and the stellar velocity dispersion of the host galaxy.

In part II we will investigate the center of the Milky Way. The GC hosts a black hole that is surrounded by a gaseous disk, the so-called circumnuclear disk (CND). This disk has an inner cavity with a radius of 1 parsec which is populated by a stellar cluster that launches a strong spherical wind. The GC is currently in a quiescent state where no significant star formation or black hole accretion is taking place, but there is evidence that the GC experienced a starburst and AGN activity several million years ago. We will perform magnetohydrodynamical simulations of the CND to investigate the interaction of the stellar cluster's wind with the CND. It has previously been argued that this wind is responsible for the quiescent state of the GC by pushing the disk's gas outwards and thus preventing accretion of gas onto the black hole. Our results disprove this scenario, invoking only the wind actually leads to a collapse of the inner cavity within a short period of time. However, including the effects of magnetic fields, which are observed in the CND, stabilizes the inner cavity against collapse. Thus our results explain why the GC is currently in a quiescent state. Furthermore we discuss whether the fading of the stellar winds will subsequently lead to the accretion of gas by the black hole, which in turn could trigger an episode of star formation and AGN activity.

Zusammenfassung: Starbursts und aktive Kerne in Galaxien

Starbursts und aktive galaktische Kerne (AGK) werden vorwiegend durch die Verschmelzung zweier Galaxien ausgelöst, aber auch in isolierten Galaxien, wie z. B. in unserer Milchstraße, können derartige Prozesse stattfinden. Daher gliedern wir diese Arbeit in zwei Teile: im ersten Teil untersuchen wir Starbursts und AGK, welche durch Galaxienkollisionen entstehen, im zweiten Teil widmen wir uns dem Galaktischen Zentrum (GZ), d. h. dem Zentrum unserer Milchstraße.

Im ersten Teil untersuchen wir insbesondere, in welcher zeitlichen Beziehung Starbursts und AGK zueinander stehen. Kürzlich durchgeführte Beobachtungen zeigen nämlich eine Zeitdifferenz zwischen diesen beiden Phänomenen, und zwar generiert die Galaxienkollision zunächst einen Starburst, gefolgt von, nach einer Zeitdauer von etwa 200-300 Myr, einer Episode erhöhter AGK Aktivität. Um diese Zeitdifferenz zu erklären entwickeln wir ein Szenario, in dem das Gas der Galaxien, nachdem es den Starburst erzeugt hat, infolge seines Drehimpulses zunächst eine Akkretionsscheibe um das zentrale Schwarze Loch bildet. Durch viskose Prozesse verliert das Gas dann diesen Drehimpuls und wird schließlich vom Schwarzen Loch verschluckt, dieser Prozess ist gekennzeichnet durch eine hohe Aktivität des galaktischen Kerns. Die beobachtete Zeitdifferenz ist also eine viskose Zeitskala, welche das Gas, nachdem es Sterne gebildet hat, zusätzlich benötigt um zum Schwarzen Loch zu gelangen. Wir entwickeln ein neues Subgrid-Modell, welches die Entstehung und die darauf folgende Entwicklung der Akkretionscheibe berücksichtigt. Die Ergebnisse unserer numerischen Simulationen von Galaxienkollisonen reproduzieren die beobachtete Zeitdifferenz zwischen Starburst und AGK Aktivität und erfüllen weitere Beobachtungsbefunde, wie die allgemein bekannte Korrelation zwischen der Masse des zentralen Schwarzen Loches und der stellaren Geschwindigkeitsdispersion der Galaxie.

Im zweiten Teil untersuchen wir das Zentrum unserer Milchstraße. Das GZ beherbergt ein Schwarzes Loch, welches von einer gasförmigen Scheibe umgeben ist. Diese Scheibe hat ein zentrales Loch mit einem Radius von etwa einem Parsec, darin befindet sich ein Sternhaufen, welcher einen starken, sphärischen Wind ausstößt. Das GZ befindet sich zur Zeit in einem Stadium geringer Aktivität, es gibt aber Hinweise auf Starbursts und AGK Aktivität, welche vor einigen Millionen Jahren stattfanden. Wir werden magnetohydrodynamische Simulationen durchführen, um die Interaktion des Innenrandes der Scheibe mit dem Wind des zentralen Sternhaufens zu untersuchen. Bisher wurde angenommen, dass dieser Wind für die derzeitige geringe Aktivität des GZs verantwortlich ist, indem dieser einen Druck auf das Gas der Scheibe ausübt und so die Akkretion des Gases auf das Schwarze Loch verhindert. Unsere Ergebnisse widerlegen dieses Szenario, berücksichtigt man nur die Interaktion der Scheibe mit dem Wind führt dies sogar zum Kollaps des inneren Loches. Nur die zusätzliche Berücksichtigung von Magnetfeldern stabilisiert das innere Loch gegen den Kollaps. Unsere Ergebnisse erklären somit, warum sich das GZ zur Zeit in einem Stadium geringer Aktivität befindet. Wir werden außerdem diskutieren, ob das Nachlassen des Windes vom zentralen Sternhaufen eine Phase erhöhter Akkretion und somit Starbursts und AGK Aktivität auslösen könnte.

Contents

1. Introduction **9**

I. Galaxy mergers 11

2. Introduction to part I **13**

3. Computational methods **17**
3.1. Smooth Particle Hydrodynamics 17
3.2. Gadget-2 21
3.3. Star formation 22
3.4. Black hole accretion 24
3.5. The Eddington limit 25
3.6. AGN feedback 27
3.7. Initial conditions and parameters 28

4. The general picture **31**
4.1. Time evolution of the merger event 31
4.2. Star formation and black hole accretion 31
4.3. The $M_{\rm BH}$-σ correlation 37
4.4. The timing of the starburst-AGN connection 37

5. Numerical Tests **41**
5.1. Star formation 41
5.2. The erratic nature of galaxy evolution 41
5.3. AGN particle 43
5.4. Two AGN particles 46
5.5. AGN feedback radius 48

6. Parameter study **51**
6.1. Effect of AGN feedback 51
6.2. Scaling of AGN size 55
6.3. AGN size 60
6.4. β-parameter 62
6.5. Gas content of the galaxies 64
6.6. Inclination 67

6.7. The M_{BH}-σ correlation 69
6.8. Discussion 71

7. Conclusions of part I **75**

II. The Galactic Center **77**

8. Introduction to part II **79**
8.1. Overview 79
8.2. Properties of the Galactic Center 79
8.3. Outline of part II 81

9. Computational methods **83**
9.1. Equations of ideal MHD 83
9.2. Additional numerical techniques 85
9.3. Initial conditions and parameters 86

10. Results **89**
10.1. Thermal properties of the CND 89
10.2. Magnetic fields 90
10.3. Interaction of the outflow with the inner rim 93
10.4. The effect of numerical viscosity 97
10.5. Full simulation 100
10.6. Clumping in the circumnuclear disk 100

11. Conclusions of part II **107**

12. Summary **109**

A. List of acronyms **111**

B. The stellar velocity dispersion **113**

Acknowledgements **125**

Erklärung **127**

1. Introduction

Many galaxies in our universe show the presence of starbursts or active nuclei, which count among the most energetic processes that can be observed in galaxies. The term 'starburst' denotes an explosive increase of star formation in a galaxy that is accompanied by an increase of the galaxy's luminosity. A further contribution to the luminosity of many galaxies is made by active galactic nuclei (AGN). An AGN, situated in the center of galaxies, consists of a central black hole surrounded by an accretion disk, a thin, disk-like structure consisting mainly of gas that orbits the black hole. The differential rotation of the disk in combination with the viscosity of the gas induces it to lose angular momentum due to frictional forces. The gas therefore spirals towards the center of the disk where it is accreted by the black hole. As a result the mass of the black hole increases during the accretion process and the gas of the accretion disk heats up due to the frictional forces. This energy is radiated away causing a high luminosity of the AGN, this is denoted as AGN activity.

These two phenomena, starbursts and AGN activity, are predominantly driven by galaxy mergers, i.e., the collision of two galaxies, as was first revealed by the infrared astronomical satellite (IRAS) in 1984. This satellite discovered many luminous infrared galaxies whose luminosity is caused by dust-obscured starbursts and AGN driven by strong interacting merger systems (Sanders et al., 1988; Genzel et al., 1998). In a galaxy merger the collision and compression of the galaxies' gas masses provokes enhanced star formation and thus triggers a starburst, furthermore tidal forces cause the inflow of gas towards the center of the newly forming galaxy, causing a high activity of the AGN. However, there are other processes that can produce moderate starbursts and AGN activity, e.g., Friedli and Benz (1995) have shown that galactic bars are capable in driving starbursts.

Not only do many galaxies show starbursts and AGN activity coexisting with each other, but they also show correlations between a starburst- and an AGN-related property. The most prominent one is the relation between the black hole mass M_{BH} and the velocity dispersion σ of the galaxy's stars[1]. This relation with approx. $M_{\mathrm{BH}} \sim \sigma^4$ was first discovered by Gebhardt et al. (2000). Wild et al. (2010) find a correlation between the time since the onset of a starburst and the accretion rate of the AGN's black hole with the accretion rate rising steeply about 250 Myr after the onset of the starburst. On the basis of these observed correlations it has been a long standing idea that starbursts and AGN share a connection with each other, but the nature of this connection remains unknown.

[1] In appendix B we explain the stellar velocity dispersion in more detail.

The aforementioned galaxy mergers produce large-scale starbursts, i.e., they occur on spatial scales of several kiloparsecs. However, Veilleux (2001) found strong evidence for circumnuclear starbursts in local AGN, that occur on spatial scales of only a few parsecs around the galaxy's center. To study circumnuclear starbursts and galactic nuclei in general, phenomena that occur on very small scales, it is essential to study the center of our own Galaxy, as due to its proximity this is the galactic center from which we have the most detailed information so far. The Galactic Center, i.e., the center of our Milky Way, shows neither AGN activity nor a starburst; it is currently in a quiescent state. However, it hosts a massive black hole, a gaseous disk that surrounds the black hole and a stellar cluster. Furthermore there is evidence for a recent episode of AGN activity and that the stars of the stellar cluster have been formed during a single starburst that happened a few million years ago. Morris et al. (1999) even propose a scenario where the Galactic Center is alternating between starbursts and AGN activity. Hence studying the Galactic Center provides a unique opportunity to understand starbursts and AGN, and how galactic centers form and evolve in general.

Thus the starburst-AGN connection on large scales is predominately driven by mergers, but isolated galaxies, like our Milky Way, can also host starbursts or AGN. Therefore this thesis consists of two parts.
In part I we will perform numerical simulations of galaxy mergers, focusing our investigations on the timing of the starburst-AGN connection. Time lags between starburst and AGN activity have been recently confirmed by observations, but so far no satisfying explanation has been provided. We will develop a model that explains such a time lag as the time the gas, after having formed stars, additionally needs to reach the central black hole.
In the second part we will turn our attention to the Galactic Center. We will perform magnetohydrodynamical simulations of the gaseous disk that surrounds the Milky Way's central black hole. Our results show that magnetic fields currently prevent the accretion of gas onto the central black hole and therefore prevent AGN activity, thus they answer the question why the Galactic Center is currently in a quiescent state. We will also elaborate on the implications for the starburst-AGN cycle proposed by Morris et al. (1999).

Part I.

Galaxy mergers

2. Introduction to part I

Over the last two decades mounting evidence has been collected indicating that starbursts and AGN are connected with each other, mostly through correlations between a starburst- and an AGN-related property. The AGN-related property is mostly the black hole mass, the starburst-related property is usually represented by a property of the galaxy's bulge[1], which is thought to be shaped by the starburst. The aforementioned M_{BH}-σ correlation is usually given in the form $M_{\mathrm{BH}} \sim \sigma^a$. The slope a has been estimated several times since the beginning of the millennium[2], resulting in a value of around 4 with an uncertainty of about 10%, but there are large deviations among the different observations and each observation shows a large intrinsic scatter. Other links between black hole mass and the stellar component of the host galaxy include the correlations between black hole mass and the mass of the galaxy's bulge (e.g., Kormendy and Richstone, 1995; Magorrian et al., 1998; Marconi and Hunt, 2003; Beifiori et al., 2012) and the correlation between black hole mass and bulge luminosity (e.g., Marconi and Hunt, 2003; Gültekin et al., 2009; Beifiori et al., 2012; Graham and Scott, 2013). However, the question remains whether these correlations imply a physical connection between starburst and AGN activity.

Recent theoretical work made important contributions to understanding the starburst-AGN connection. In simulations of major mergers[3] conducted by Di Matteo et al. (2005), the compression of the galaxies' gas masses and tidal forces produce a starburst and AGN activity. Furthermore they successfully reproduced the M_{BH}-σ correlation due to the implementation of AGN feedback. In their scenario the AGN's luminosity heats and thus expels the surrounding gas from the galaxy, and therefore quenches further star formation and AGN activity and determines the final black hole mass. More massive galaxies have a deeper gravitational potential well, thus the AGN has to be more luminous to expel the gas. As the AGN luminosity is proportional to the black hole mass[4], the black hole has to gain more mass before its luminosity is capable in expelling the gas and thus setting the final black hole mass. This leads the black hole mass to be linked to the mass of host galaxy and thus explains correlations between

[1] The bulge of a galaxy is defined as the galaxy's central region, which is spherically symmetric and consists predominantly of stars.

[2] 3.75 ± 0.3 (Gebhardt et al., 2000), 4.8 ± 0.5 (Ferrarese and Merritt, 2000), 4.72 ± 0.36 (Merritt and Ferrarese, 2001), 4.02 ± 0.32 (Tremaine et al., 2002), 3.68 ± 0.42 (Graham, 2008), 4.24 ± 0.41 (Gültekin et al., 2009)

[3] The term 'major merger' denotes a merger of galaxies with equal mass.

[4] This is only the case if the black hole is accreting at its Eddington limit, see section 3.5 for a detailed explanation.

black hole mass and stellar velocity dispersion or bulge mass. Whereas Di Matteo et al. (2005) only investigated major mergers of disk galaxies, Johansson et al. (2009) showed that equal- and unequal-mass mergers of disk and elliptical galaxies also reproduce the observed $M_{\rm BH}$-σ correlation.

An important question regarding the starburst-AGN connection concerns the timing of these two phenomena, i.e., whether the starburst precedes or follows AGN activity. Recent observations indicate a time lag between starburst and AGN activity (Davies et al., 2007; Schawinski et al., 2009; Wild et al., 2010) in the sense that first the galaxy experiences a starburst, followed by, after a time span of 200-300 Myr, an episode of AGN activity. Previous simulations of galaxy mergers successfully reproduced starbursts and AGN activity (e.g., Di Matteo et al., 2005; Johansson et al., 2009; Debuhr et al., 2011, 2012; Choi et al., 2012), but in all these simulations starburst and AGN activity occur simultaneously and thus fail to reproduce the observed time lag. The reason for this time lag is a matter of intense debate, but so far only a few attempts have been made to explain this phenomenon. Hopkins (2012) argues that such a time lag can occur for purely dynamical reasons. His high spatial resolution simulations of galaxy mergers show first an inward motion of gas towards the dynamical center of the newly forming galaxy, giving rise to a starburst. In these models, the gas flowing further inwards can do so only by losing angular momentum by gravitational instabilities, this process takes some time and thus gives rise to a time lag between starburst and AGN activity. This work highlights the essential aspect of the time lag, namely that the gas needs time to cover the distance to the black hole. However, it lacks some important physical mechanisms that are relevant in galactic centers. The gas flowing towards the center will form an accretion disk, where viscous processes will become relevant for angular momentum extraction and for the accretion of material towards the black hole. Wild et al. (2010) have argued that the black hole is fed with stellar winds and supernova ejecta provided from the stars that were formed during the starburst, and that the observed time lag is simply the timescale for star formation. However, it is unlikely that these processes can provide enough mass to explain the high black hole accretion rates of several solar masses per year that are known from both, observations and simulations.

In part I of this thesis we will simulate galaxy mergers and focus on the correct modeling of the time lag between starburst and AGN activity. We will develop a subgrid model that accounts for the formation of an accretion disk and the subsequent viscous evolution of the gas. Thus in our scenario the time lag between starburst and AGN activity is a viscous timescale the gas, after having formed stars, additionally needs to reach the central black hole. Our results reproduce the observed time lags and fulfill further observational constraints: they match the observed $M_{\rm BH}$-σ correlation and give an explanation for the large observed scatter of this correlation.

This part is organized as follows: The next chapter will be dedicated to our numerical methods and the galaxy model that we are using. In chapter 4 we will describe the general picture that results from our model setup, we will elaborate on the time sequence of the merger event, the properties of the time lag between starburst and AGN activity

and discuss the $M_{\rm BH}$-σ correlation that results from our simulations. In chapter 5 we will perform numerical tests of our algorithms. As our calculations depend on a number of parameters, some of which are not well constrained by observations, we will perform a parameter study in chapter 6 to test the robustness of our model against parameter changes. We will finally summarize our findings in chapter 7.

3. Computational methods

To simulate galaxy mergers we use the numerical technique of Smooth Particle Hydrodynamics (SPH) that we will introduce in section 3.1. We solve the equations of SPH with the simulation code GADGET-2, developed by Springel (2005), an overview of which is given in section 3.2. In sections 3.3-3.6 we introduce additional algorithms to account for star formation, black hole accretion and AGN feedback that are not part of the official version of GADGET-2. We will close this chapter with section 3.7, where we describe our galaxy model and give the initial conditions and parameters of our simulations.

3.1. Smooth Particle Hydrodynamics

Smooth Particle Hydrodynamics (SPH) is a Lagrangian particle method for solving the equations of hydrodynamics. Originally developed by Lucy (1977) and Gingold and Monaghan (1977), a detailed review of this method can be found in Monaghan (1992), Springel (2010) or Price (2012). In the following we will first derive a density estimate for an ensemble of particles, then we will derive the equations of motion and the energy equation in the SPH formalism and finally elaborate on the conservation properties of these equations.

Calculating the density

In SPH the fluid is represented by an ensemble of particles with positions $\vec{r}_\mathrm{i}$ and masses m_i. The density at the position of particle i is then calculated as

$$\rho_i = \sum_{k=1}^{N} m_k W(|\vec{r}_i - \vec{r}_k|, h_i) \tag{3.1}$$

where N is the number of neighbors of particle i, W is a weight function (the so-called kernel function) and h_i is the so-called smoothing length. The kernel function can have different forms, as long as it is positive, normalized, decreases monotonically with distance and has smooth derivatives. The simulation code GADGET-2 uses the following kernel function:

$$W(r,h) = \frac{8}{\pi h^3} \begin{cases} 1 - 6(\frac{h}{r})^2 + 6(\frac{h}{r})^3, & 0 \leq \frac{h}{r} \leq \frac{1}{2} \\ 2(1 - \frac{h}{r})^3, & \frac{1}{2} < \frac{h}{r} \leq 1 \\ 0, & \frac{h}{r} > 1 \end{cases} \tag{3.2}$$

The smoothing length h_i of each particle is defined such that its volume contains a constant mass, thus it fulfills the equation

$$\frac{4\pi}{3} h_i^3 \rho_i = N\overline{m}\,, \tag{3.3}$$

where $\overline{m}$ is the average particle mass. The number of neighbors N is a free parameter of the numerical method, we will use $N_{\mathrm{sph}} = 40$ throughout this thesis. As ρ_i also depends on h_i (due to eq. 3.1) eq. 3.3 is an implicit equation that can be solved for h_i with standard root-solving methods.

The equations of motion

To derive the equations of motion we start with the Lagrangian of the system

$$L = K - V \tag{3.4}$$

with the kinetic energy K and the potential Energy V. The Lagrangian fulfills the Euler-Lagrange equation

$$\frac{d}{dt}\frac{\partial L}{\partial \dot{q}_i} - \frac{\partial L}{\partial q_i} = 0\,. \tag{3.5}$$

For a system of point masses with positions $\vec{r}_j$ as generalized coordinates, velocities $\vec{v}_j$, masses m_j and internal energies per unit mass u_j we have

$$L = \sum_j m_j \left[\frac{1}{2}\vec{v}_j^{\,2} - u_j(\rho_j, s_j)\right] \tag{3.6}$$

and

$$\frac{d}{dt}\frac{\partial L}{\partial \vec{v}_i} - \frac{\partial L}{\partial \vec{r}_i} = 0\,, \tag{3.7}$$

where u_j is a function of the density ρ_j and the entropy s_j. From eq. 3.6 we get

$$\frac{\partial L}{\partial \vec{v}_i} = m_i \vec{v}_i \tag{3.8}$$

and

$$\frac{\partial L}{\partial \vec{r}_i} = -\sum_j m_j \frac{\partial u_j}{\partial \vec{r}_i} = -\sum_j m_j \left.\frac{\partial u_j}{\partial \rho_j}\right|_s \frac{\partial \rho_j}{\partial \vec{r}_i} \tag{3.9}$$

where we assume constant entropy (i.e., no dissipation). To find an expression for the partial derivative of the internal energy per unit mass to the density in eq. 3.9 we use the first law of thermodynamics, where the change in internal energy is the sum of the heat added to the system and the work done by compression and expansion,

$$du = Tds - Pdv\,. \tag{3.10}$$

Here P is the pressure and v the volume per unit mass (i.e., the inverse density), thus dv can be written as $dv = -d\rho \cdot \rho^{-2}$ resulting in

$$du = Tds + \frac{P}{\rho^2} d\rho \,. \tag{3.11}$$

This gives, considering the constant entropy

$$\left.\frac{\partial u}{\partial \rho}\right|_s = \frac{P}{\rho^2} \,. \tag{3.12}$$

The partial derivative of the density to the position in eq. 3.9 can be written, using eq. 3.1 and the notations $W_{jk} \equiv W(|\vec{r}_j - \vec{r}_k|, h_j)$ and $\vec{r}_{jk} \equiv \vec{r}_j - \vec{r}_k$, as

$$\begin{aligned}
\frac{\partial \rho_j}{\partial \vec{r}_i} &= \sum_k m_k \left(\frac{\partial W_{jk}}{\partial \vec{r}_{jk}} \frac{\partial \vec{r}_{jk}}{\partial \vec{r}_i} + \frac{\partial W_{jk}}{\partial h_j} \frac{\partial h_j}{\partial \vec{r}_i} \right) \\
&= \sum_k m_k \left(\frac{\partial W_{jk}}{\partial \vec{r}_{jk}} (\delta_{ij} - \delta_{ik}) + \frac{\partial W_{jk}}{\partial h_j} \frac{\partial h_j}{\partial \rho_j} \frac{\partial \rho_j}{\partial \vec{r}_i} \right) \\
&= \sum_k m_k \frac{\partial W_{jk}}{\partial \vec{r}_{jk}} (\delta_{ij} - \delta_{ik}) + \frac{\partial \rho_j}{\partial \vec{r}_i} \frac{\partial h_j}{\partial \rho_j} \sum_k m_k \frac{\partial W_{jk}}{\partial h_j} \,.
\end{aligned} \tag{3.13}$$

Rearranging for the density derivative gives

$$\frac{\partial \rho_j}{\partial \vec{r}_i} = \frac{1}{\Omega_j} \sum_k m_k \frac{\partial W_{jk}}{\partial \vec{r}_{jk}} (\delta_{ij} - \delta_{ik}) \tag{3.14}$$

with

$$\Omega_j \equiv \left[1 - \frac{\partial h_j}{\partial \rho_j} \sum_k m_k \frac{\partial W_{jk}}{\partial h_j} \right] \,. \tag{3.15}$$

Using eq. 3.3 the derivative of the smoothing length to the density can be expressed as

$$\frac{\partial h_j}{\partial \rho_j} = -\frac{1}{3} \frac{h_j}{\rho_j} \,. \tag{3.16}$$

Inserting eqs. 3.12 and 3.14 into eq. 3.9 yields

$$\begin{aligned}
\frac{\partial L}{\partial \vec{r}_i} &= -\sum_j m_j \left.\frac{\partial u_j}{\partial \rho_j}\right|_s \frac{\partial \rho_j}{\partial \vec{r}_j} = -\sum_j \frac{m_j}{\Omega_j} \frac{P_j}{\rho_j^2} \sum_k m_k \frac{\partial W_{jk}}{\partial \vec{r}_{jk}} (\delta_{ij} - \delta_{ik}) \\
&= -\sum_k \frac{m_i}{\Omega_i} \frac{P_i}{\rho_i^2} m_k \frac{\partial W_{ik}}{\partial \vec{r}_{ik}} + \sum_j \frac{m_j}{\Omega_j} \frac{P_j}{\rho_j^2} m_i \frac{\partial W_{ji}}{\partial \vec{r}_{ji}} \\
&= -\sum_j m_i m_j \left(\frac{P_i}{\Omega_i \rho_i^2} + \frac{P_j}{\Omega_j \rho_j^2} \right) \frac{\partial W_{ij}}{\partial \vec{r}_{ij}} \,.
\end{aligned} \tag{3.17}$$

The eqs. 3.8 and 3.17 finally yield, when inserting into the Euler-Lagrange equation 3.7,

$$\frac{d}{dt}\left(m_i\vec{v}_i\right) = -\sum_j m_i m_j \left(\frac{P_i}{\Omega_i\rho_i^2} + \frac{P_j}{\Omega_j\rho_j^2}\right)\frac{\partial W_{ij}}{\partial \vec{r}_{ij}} \tag{3.18}$$

and thus give the acceleration of the particle i due to hydrodynamical forces:

$$\boxed{\left.\frac{d\vec{v}_i}{dt}\right|_{\text{hydr}} = -\sum_j m_j \left(\frac{P_i}{\Omega_i\rho_i^2} + \frac{P_j}{\Omega_j\rho_j^2}\right)\frac{\partial W_{ij}}{\partial \vec{r}_{ij}}} \tag{3.19}$$

The energy equation

The change of the internal energy can be considered by taking the time derivative of the internal energy of particle i, using eq. 3.12 gives

$$\frac{du_i}{dt} = \frac{du_i}{d\rho_i}\frac{d\rho_i}{dt} = \frac{P_i}{\rho_i^2}\frac{d\rho_i}{dt}\,. \tag{3.20}$$

The density's time derivative can be calculated in the same manner as its spatial derivative in eq. 3.14:

$$\frac{d\rho_i}{dt} = \frac{1}{\Omega_i}\sum_k m_k \frac{\partial W_{ik}}{\partial \vec{r}_{ik}}\frac{d\vec{r}_{ik}}{dt} = \frac{1}{\Omega_i}\sum_k m_k \frac{\partial W_{ik}}{\partial \vec{r}_{ik}}\left(\vec{v}_i - \vec{v}_k\right) \tag{3.21}$$

Thus we get

$$\boxed{\frac{du_i}{dt} = \frac{du_i}{d\rho_i}\frac{d\rho_i}{dt} = \frac{P_i}{\Omega_i\rho_i^2}\sum_k m_k \frac{\partial W_{ik}}{\partial \vec{r}_{ik}}\left(\vec{v}_i - \vec{v}_k\right)}\,. \tag{3.22}$$

We close the system of equations by using the equation of state for an ideal gas

$$P = (\gamma - 1)\rho u\,. \tag{3.23}$$

By specifying the initial positions, velocities, masses and internal energies of all particles and choosing a kernel function, eqs. 3.19 and 3.22 allow us to calculate the change of the velocity and the internal energy. Thus by integrating these equations with a given time step Δt, the time evolution of the system can be calculated.

Conservation properties

We investigate the conservation properties of eqs. 3.19 and 3.22 regarding the conservation of linear momentum, angular momentum and energy. First, we note that

$$\frac{\partial W_{ij}}{\partial \vec{r}_{ij}} = \frac{\partial W_{ij}}{\partial |\vec{r}_{ij}|}\frac{\partial |\vec{r}_{ij}|}{\partial \vec{r}_{ij}} = \frac{\partial W_{ij}}{\partial |\vec{r}_{ij}|}\frac{\vec{r}_{ij}}{|\vec{r}_{ij}|} = \alpha_{ij}\vec{r}_{ij} \tag{3.24}$$

with

$$\alpha_{ij} \equiv \frac{1}{|\vec{r}_{ij}|}\frac{\partial W_{ij}}{\partial |\vec{r}_{ij}|} \tag{3.25}$$

and because $\alpha_{ij} = \alpha_{ji}$ and $\vec{r}_{ij} = -\vec{r}_{ji}$ the kernel gradient is antisymmetric regarding transposition of the indices ij. Calculating the time derivative of the total linear momentum gives, using eq. 3.19,

$$\frac{d}{dt}\sum_i m_i \vec{v}_i = \sum_i m_i \frac{d\vec{v}_i}{dt} = -\sum_{ij} m_i m_j \left(\frac{P_i}{\Omega_i \rho_i^2} + \frac{P_j}{\Omega_j \rho_j^2}\right)\frac{\partial W_{ij}}{\partial \vec{r}_{ij}} = 0 \tag{3.26}$$

which is zero because of the antisymmetry of the kernel gradient. The time derivative of the total angular momentum gives

$$\begin{aligned}\frac{d}{dt}\sum_i \vec{r}_i \times m_i \vec{v}_i &= \sum_i m_i \vec{r}_i \times \frac{d\vec{v}_i}{dt} = -\sum_{ij} m_i m_j \left(\frac{P_i}{\Omega_i \rho_i^2} + \frac{P_j}{\Omega_j \rho_j^2}\right)\vec{r}_i \times \frac{\partial W_{ij}}{\partial \vec{r}_{ij}} \\ &= -\sum_{ij} m_i m_j \alpha_{ij}\left(\frac{P_i}{\Omega_i \rho_i^2} + \frac{P_j}{\Omega_j \rho_j^2}\right)\vec{r}_i \times \vec{r}_{ij} = \sum_{ij} m_i m_j \alpha_{ij}\left(\frac{P_i}{\Omega_i \rho_i^2} + \frac{P_j}{\Omega_j \rho_j^2}\right)\vec{r}_i \times \vec{r}_j = 0\end{aligned} \tag{3.27}$$

which is again zero because $\vec{r}_i \times \vec{r}_j = -\vec{r}_j \times \vec{r}_i$. Finally, we examine the total energy using eqs. 3.19 and 3.22:

$$\begin{aligned}\frac{dE}{dt} &= \sum_i m_i \left(\vec{v}_i \frac{d\vec{v}_i}{dt} + \frac{du_i}{dt}\right) \\ &= \sum_i m_i \left(-\vec{v}_i \sum_j m_j \left(\frac{P_i}{\Omega_i \rho_i^2} + \frac{P_j}{\Omega_j \rho_j^2}\right)\frac{\partial W_{ij}}{\partial \vec{r}_{ij}} + \frac{P_i}{\Omega_i \rho_i^2}\sum_j m_j (\vec{v}_i - \vec{v}_j)\frac{dW_{ij}}{d\vec{r}_{ij}}\right) \\ &= -\sum_{ij} m_i m_j \left(\vec{v}_i \frac{P_j}{\Omega_j \rho_j^2} + \vec{v}_j \frac{P_i}{\Omega_i \rho_i^2}\right)\frac{dW_{ij}}{d\vec{r}_{ij}} = 0\end{aligned} \tag{3.28}$$

which is likewise zero, because the kernel gradient is antisymmetric and the term in brackets is symmetric regarding transposition of the indices ij. Thus the basic equations of SPH, eqs. 3.19 and 3.22, conserve total linear momentum, total angular momentum and total energy exactly.

3.2. Gadget-2

To simulate galaxy mergers we use the TreeSPH code GADGET-2 that was developed by Springel (2005). GADGET-2 in general differentiates between two types of particles: gas particles and collisionless particles. The latter can be further divided into, e.g., dark matter particles or star particles. It considers gravitational forces between all particles using a tree algorithm. This method groups distant particles into ever larger

cells, their gravitational force on one particle is then calculated as a single multipole force. Thus instead requiring the calculation of $N-1$ forces per particle, where N is the total number of particles, only $\log N$ forces have to be calculated. To account for hydrodynamical forces this code additionally solves the SPH equations that we derived in section 3.1 for the gaseous particles. Radiative cooling of an optically thin primordial gas in ionization equilibrium is taken into account following Katz et al. (1996). GADGET-2 is fully parallelized and uses individual time steps for each particle, making it very efficient. The accuracy and performance of GADGET-2 has been verified using a number of standard test problems. We additionally include algorithms for star formation, black hole accretion and AGN feedback as described in the following subsections.

3.3. Star formation

According to the framework of SPH the gaseous part of our galaxies consists of a particular number of SPH particles. With our parameter choices (see section 3.7) one SPH particle has a mass of about $6 \cdot 10^5\,\mathrm{M}_\odot$, so one SPH particle can be regarded as a giant molecular cloud. It is supposed that most of a galaxy's gas is located in such clouds and that stars are predominantly born in these giant molecular clouds due to gravitational fragmentation and gravitational collapse of the gas.

To account for star formation in our simulations we have to develop an algorithm that determines if a giant molecular cloud is subject to star formation, and if so, what the star formation rate is. The star formation algorithm presented in this section is based on the papers from Katz (1992), Springel and Hernquist (2003) and Scannapieco et al. (2005) and was implemented by Xiang-Grüß (2009).

Observations from Kennicutt (1989) suggest that star formation is almost completely suppressed at densities below a certain threshold density, so one criterion for the onset of star formation is that the density ρ_i of the gas particle i has to exceed this threshold density ρ_crit, which is a free parameter of our algorithm. We choose a value of $\rho_\mathrm{crit} = 0.45\,\mathrm{M}_\odot\,\mathrm{pc}^{-3}$ unless stated otherwise; in section 5.1 we will test our star formation algorithm and show that our parameter choices produce realistic star formation rates. Furthermore star formation only occurs in regions that are in a state of collapse, therefore the second criterion for the onset of star formation is that the velocity divergence of the gas particle i has to be less than zero. If these two conditions

$$\begin{aligned} \rho_i &> \rho_\mathrm{crit} \\ \nabla \cdot \vec{v}_i &< 0 \end{aligned} \tag{3.29}$$

are fulfilled the gas particle i, i.e., the giant molecular cloud, is subject to star formation, we now have to determine the amount of mass that is converted into stars.

We assume that the star formation rate inside the giant molecular cloud is proportional to its mass M_g divided by the time the cloud needs for a free-fall collapse. According to

Hopkins et al. (2011) the latter can be calculated as

$$t_* = \sqrt{3\pi/32G\rho}\,. \tag{3.30}$$

Thus the star formation rate is

$$\dot{M}_* = c_* \frac{M_\mathrm{g}}{t_*} \tag{3.31}$$

with the star formation efficiency c_* which can be derived from observations, we adopt a value of $c_* = 0.1$ (Katz, 1992). Note that the star formation rate eq. 3.31 is proportional to $\rho^{1.5}$. This is the same relation that is suggested by the Kennicutt-Schmidt law (Schmidt, 1959; Kennicutt, 1998), an empirical relation that describes how the star formation rate is connected to the gas density. The gas mass that is converted into stars within the time step Δt is then

$$M_* = c_* M_\mathrm{g} \frac{\Delta t}{t_*}\,. \tag{3.32}$$

One could now create a new star particle with this mass in each time step and reduce the mass of the gas particle accordingly. But as this mass is usually a few percent of the gas particles mass, this would lead to the creation of a very large number of new star particles and thus slow down the computation. Instead, we fix the mass M_* of a new star particle to

$$M_* = \frac{M_\mathrm{g0}}{N_\mathrm{g}} \tag{3.33}$$

where M_g0 is the initial mass of the gas particle and N_g is the number of star particles that can be formed from one gas particle, which is $N_\mathrm{g} = 2$ for our algorithm. Then the quotient of eq. 3.32 and eq. 3.33 can be interpreted as the probability

$$p_* = c_* N_\mathrm{g} \frac{M_\mathrm{g}}{M_\mathrm{g0}} \frac{\Delta t}{t_*} \tag{3.34}$$

that a gas particle with mass M_g forms a star particle with mass M_*. Each time step we check for all gas particles if the conditions 3.29 apply and if p_* is larger than a random number that is drawn from the interval $[0, 1]$. If these conditions are fulfilled a new star particle with mass M_* is created with the same position and velocity as the parent gas particle. The mass of the gas particle is reduced by M_*, or it is removed completely if its mass equals the new star particle's mass.

More advanced algorithms have been developed that include the effects of supernovae and stellar winds on the star formation rate. These feedback processes tend to mitigate excessive star formation, resulting in slightly less pronounced starbursts. However, stellar feedback does not change the outcomes that are crucial for our scenario, namely first that a merger event produces a starburst at all and second, the point in time the starburst occurs. Thus we neglect the effects of stellar feedback in our simulations.

3.4. Black hole accretion

The galaxy's central black hole can be modeled as a sink particle (Bate et al., 1995), that only interacts with its environment via gravitation and that accretes gas particles. Whenever a gas particle is accreted its mass and momentum is added to the sink particle and the gas particle is removed from the simulation. Due to the limited resolution of merger simulations the accretion flow onto black holes, that occurs on scales of the Schwarzschild radius, usually cannot be resolved. Thus it is necessary to apply a subgrid model to calculate the accretion rate of the black hole.

A model often used (e.g., in Springel et al., 2005; Johansson et al., 2009; Choi et al., 2012) is the so-called Bondi-Hoyle-Lyttleton parametrization (Hoyle and Lyttleton, 1939; Bondi and Hoyle, 1944; Bondi, 1952). Here a gas cloud with velocity v, density ρ and sound speed c_s moves across a black hole with mass M_BH, leading to spherical accretion of the gas by the black hole. For this scenario an analytical formula for the black hole accretion rate $\dot{M}_\mathrm{BHL}$ can be derived:

$$\dot{M}_\mathrm{BHL} = \frac{4\pi\alpha G^2 M_\mathrm{BH}^2 \rho}{(c_\mathrm{s}^2 + v^2)^{3/2}} \tag{3.35}$$

The dimensionless parameter α is not part of the original formula but was first introduced by Springel et al. (2005), and it is usually set to values of about 100. Choi et al. (2012) justify this parameter due to numerical resolution effects, because "the low spatial resolution currently available would otherwise limit the accretion rate to lower than the true value". However, the Bondi-Hoyle-Lyttleton parametrization contains several inadequacies:

(I) It is now widely accepted that gas, before it is accreted by a black hole, forms an accretion disk due to its angular momentum. The Bondi-Hoyle-Lyttleton parametrization assumes spherical accretion and thus completely neglects the angular momentum of the gas.

(II) It is further assumed that the accretion disk's gas loses angular momentum due to viscous forces and then is accreted by the black hole. Viscous processes are also not considered in the above-mentioned approach.

(III) Due to the limited resolution changes in quantities like density or sound speed, that occur within $\sim 100\,\mathrm{pc}$ around the black hole, will instantly affect the accretion rate of the black hole. But it is reasonable to assume that such changes need some time to reach the black hole and to affect its accretion rate. This is a very important point, as in part I of this thesis we investigate time lags between starbursts and the black hole accretion rate.

(IV) The above-mentioned accretion rate depends on the artificial parameter α, that is a priori unknown and depends on the numerical resolution, and without this parameter fails to produce realistic results.

In this thesis we will use a different approach to account for the angular momentum and the viscous evolution of the gas. Following Power et al. (2011) the sink particle of our simulations, instead of representing just the black hole, represents the entire AGN, i.e., the black hole and the accretion disk that surrounds the black hole.

All gas particles that are within a specific radius, the so-called AGN radius R_{AGN}, are swallowed by the sink particle, which we from now on denote as 'AGN particle'. R_{AGN} is a free parameter of our model. We use the implementation of Jappsen et al. (2005) to account for the accretion of gas particles by the sink particle. This swallowed mass is added to the outer rim of the accretion disk, which conforms with the AGN radius, and is then accreted towards the black hole.

To calculate this accretion process we assume that the disk that is hosted by the AGN particle is axisymmetric and geometrically thin, and that the disk evolves slowly enough that we can neglect the time derivative of its angular frequency. According to Pringle (1981) these assumptions lead to a single equation that describes the time dependent evolution of such an accretion disk:

$$\frac{\partial \Sigma}{\partial t} + \frac{1}{s}\frac{\partial}{\partial s}\left[\frac{\frac{\partial}{\partial s}\left(s\nu\Sigma s^2\frac{\partial \omega}{\partial s}\right)}{\frac{\partial (s^2\omega)}{\partial s}}\right] = 0 \tag{3.36}$$

Here s is the distance to the black hole and Σ is the surface density of the disk. ω is the angular frequency which we calculate through a balance between centrifugal and gravitational forces. ν is the turbulent viscosity of the gas that we parametrize with the β-viscosity (Duschl et al., 2000)

$$\nu = \beta s^2 \omega\,. \tag{3.37}$$

β has values of 10^{-3} to 10^{-2}, we use a value of 0.004 unless stated otherwise. In Blank (2010) we developed the software package 'Hedis' that solves eq. 3.36 by using a finite difference method and an implicit Crank-Nicolson time integration scheme (Crank et al., 1947). For further details of the disk model and the numerical scheme we refer to Blank (2010). Solving eq. 3.36 provides the mass flow $\dot{M}_{\mathrm{d}}$ over the inner edge of the accretion disk, that yields the accretion rate of the black hole (see section 3.6). We still have to specify initial conditions for the accretion disk and for the black hole mass. For simplicity we choose a constant initial surface density profile. As the disk's outer radius is already set by R_{AGN}, we only have to specify the initial disk mass $M_{\mathrm{d},0}$ and the initial black hole mass $M_{\mathrm{BH},0}$, which we will do in section 3.7.

3.5. The Eddington limit

To estimate the luminosity of an AGN we consider a test particle that is part of the accretion disk and that orbits the AGN's central black hole. By moving from radius r_2 to radius r_1 the particle with mass m releases the energy

$$E = \frac{1}{2} G M_{\mathrm{BH}} m \left(\frac{1}{r_1} - \frac{1}{r_2}\right) \tag{3.38}$$

with the black hole mass M_{BH}. This energy is converted into radiation due to viscous forces, thus replacing the mass m by the mass flow onto the black hole $\dot{M}_{\mathrm{BH}}$ and assuming $r_2 \gg r_1$ yields the luminosity of the AGN:

$$L = \frac{GM_{\mathrm{BH}}\dot{M}_{\mathrm{BH}}}{2r_1} \tag{3.39}$$

The radius r_1 corresponds to the inner radius of the accretion disk which is, for accretion disks around black holes, a multiple[1] of the black hole's Schwarzschild radius r_{S}, thus

$$r_1 = \epsilon r_{\mathrm{S}} = \epsilon \frac{2GM_{\mathrm{BH}}}{c^2}\,, \tag{3.40}$$

where c is the speed of light. Therefore the AGN's luminosity is

$$L = \eta \dot{M}_{\mathrm{BH}} c^2 \tag{3.41}$$

with $\eta = 1/4\epsilon$. A value of $\eta = 0.1$ is usually chosen for standard accretion disks (Shakura and Sunyaev, 1973). Thus an amount of energy equivalent to 10% of the rest mass energy of the gas is released, making accretion one of the most efficient processes in the universe.

The AGN's intensity $I = L/4\pi r^2$ results in radiation pressure P_{rad}, that causes a force

$$F_{\mathrm{rad}} = P_{\mathrm{rad}}\sigma_{\mathrm{T}} = \frac{I}{c}\sigma_{\mathrm{T}} = \frac{L}{4\pi r^2}\frac{\sigma_{\mathrm{T}}}{c} = \frac{\eta \dot{M} c^2}{4\pi r^2}\frac{\sigma_{\mathrm{T}}}{c} \tag{3.42}$$

on a hydrogen atom, where σ_{T} is the Thomson cross section and r is the distance to the black hole. If this radiation force exceeds the gravitational force, accretion is halted. Thus equating both forces

$$\frac{\eta \dot{M}_{\mathrm{EDD}} c^2}{4\pi r^2}\frac{\sigma_{\mathrm{T}}}{c} = \frac{GM_{\mathrm{BH}} m_{\mathrm{H}}}{r^2}\,, \tag{3.43}$$

where m_{H} is the hydrogen mass, gives the highest possible accretion rate $\dot{M}_{\mathrm{EDD}}$, the so-called Eddington limit (Eddington, 1921). It has the final form

$$\dot{M}_{\mathrm{EDD}} = \frac{4\pi G M_{\mathrm{BH}} m_{\mathrm{H}}}{\eta c \sigma_{\mathrm{T}}} = \frac{M_{\mathrm{BH}}}{\tau_{\mathrm{S}}} \tag{3.44}$$

with the Salpeter-timescale (Salpeter, 1964)

$$\tau_{\mathrm{S}} = \frac{\eta c \sigma_{\mathrm{T}}}{4\pi G m_{\mathrm{H}}} = \eta \cdot 4.5 \cdot 10^8\,\mathrm{yr}\,. \tag{3.45}$$

The black hole accretion rate can never exceed the Eddington limit. Thus if the mass flow $\dot{M}_{\mathrm{d}}$ from the accretion disk is larger than the Eddington limit, the black hole accretion rate has to be limited accordingly.

[1] The value ϵ depends on the properties of the black hole, e.g., $\epsilon = 3$ for a non-rotating black hole.

3.6. AGN feedback

An AGN releases huge amounts of energy and thus has a large effect on its host galaxy. This energy is injected into the galaxy's gas that then gets expelled, thus star formation and black hole growth are quenched. These processes must be considered in merger simulations to yield the correct M_{BH}-σ correlation.

To account for AGN feedback we follow the model developed by Debuhr et al. (2011, 2012). The radiation pressure caused by the AGN's luminosity L injects energy in the form of momentum into the gas that surrounds the AGN resulting in a force

$$\dot{p}_{\mathrm{rad}} = \tau_{\mathrm{rad}} \frac{L}{c} \,, \tag{3.46}$$

where τ_{rad} is the optical depth of the gas, following Debuhr et al. (2011) we choose a value of $\tau_{\mathrm{rad}} = 25$. Furthermore the AGN feedback launches a wind that likewise injects momentum into the surrounding gas and thus results in a force

$$\dot{p}_{\mathrm{w}} = \tau_{\mathrm{w}} \frac{L}{c} \,, \tag{3.47}$$

the free parameter τ_{w} was adjusted by Debuhr et al. (2012) to normalize the M_{BH}-σ correlation. We do the same and set $\tau_{\mathrm{w}} = 3$. Thus the total force acting on the surrounding gas is

$$\dot{p} = \dot{p}_{\mathrm{rad}} + \dot{p}_{\mathrm{w}} \,. \tag{3.48}$$

Using eq. 3.47 we can calculate the mass flow of the wind

$$\dot{M}_{\mathrm{w}} = \tau_{\mathrm{w}} \frac{L}{c v_{\mathrm{w}}} \tag{3.49}$$

where v_{w} is the wind speed. We use a value of $v_{\mathrm{w}} = 10\,000\,\mathrm{km\,s^{-1}}$ as suggested by Debuhr et al. (2012); Moe et al. (2009) also observed galaxies with such high velocity outflows.

The wind reduces the mass flow $\dot{M}_{\mathrm{d}}$ that is provided by the accretion disk, thus the black hole accretion rate reads

$$\dot{M}_{\mathrm{BH}} = \dot{M}_{\mathrm{d}} - \dot{M}_{\mathrm{w}} \,. \tag{3.50}$$

Inserting eqs. 3.49 and 3.41 and rearranging for $\dot{M}_{\mathrm{BH}}$ yields

$$\dot{M}_{\mathrm{BH}} = \frac{\dot{M}_{\mathrm{d}}}{1 + \tau_{\mathrm{w}} \eta c / v_{\mathrm{w}}} \,. \tag{3.51}$$

The black hole accretion is limited to the Eddington rate, thus the black hole accretion rate has the final form

$$\dot{M}_{\mathrm{BH}} = \min \left(\frac{\dot{M}_{\mathrm{d}}}{1 + \tau_{\mathrm{w}} \eta c / v_{\mathrm{w}}}, \dot{M}_{\mathrm{EDD}} \right) \,. \tag{3.52}$$

In each time step Δt of the code we calculate the AGN luminosity with eqs. 3.41 and 3.52, then we calculate the total momentum $\dot{\vec{p}}\Delta t$ and the total mass $\dot{M}_{\rm w}\Delta t$ of the feedback. We then distribute these quantities to the gas particles that surround the AGN, namely to all gas particles within $2\,R_{\rm AGN}$ of the AGN particle. In section 5.5 we will show that the choice of this radius is not crucial for our results.

3.7. Initial conditions and parameters

In the standard model of galaxy formation (e.g., Mo et al., 1998) gravitational instabilities in the early universe amplify weak density perturbations, thus the dark matter, the main component of matter in our universe, aggregates into clumps (so-called dark matter halos) that provide the seeds for galaxy formation. The gas then cools and condenses within the dark matter halos, and settles down into a disk.

We model our disk galaxies as described by Springel and White (1999) and Springel (2000) based on the analytical model of Mo et al. (1998). In this framework a dark matter halo is defined as a sphere with a radius $R_{\rm vir}$ (the so-called virial radius) whose mean density is 200 times the cosmological critical density, thus it contains the virial mass

$$M_{\rm vir} = 200\rho_{\rm c}\frac{4\pi}{3}R_{\rm vir}^3 \tag{3.53}$$

with the cosmological critical density

$$\rho_{\rm c} = \frac{3H^2}{8\pi G}\,, \tag{3.54}$$

the gravitational constant G and the Hubble constant H, we use a value of $H = 70\,{\rm km\,s^{-1}\,Mpc^{-1}}$ throughout this thesis. We furthermore define the circular velocity at the virial radius

$$v_{\rm vir}^2 = \frac{GM_{\rm vir}}{R_{\rm vir}}\,. \tag{3.55}$$

Combining eqs. 3.53, 3.54 and 3.55 gives

$$R_{\rm vir} = \frac{v_{\rm vir}}{10H} \tag{3.56}$$

and

$$M_{\rm vir} = \frac{v_{\rm vir}^3}{10GH}\,. \tag{3.57}$$

The equations 3.55, 3.56 and 3.57 form the basis of our galaxy model. Any of the parameters $v_{\rm vir}$, $M_{\rm vir}$ or $R_{\rm vir}$ can be used to characterize a galaxy, as specifying one of them directly yields the others; throughout this thesis we will use the virial velocity.

The other components of the galaxy are then modeled as follows. A fraction m_d of the virial mass forms a thin galactic disk with a profile

$$\rho_\mathrm{d}(R,z) = \rho_0 \exp\left(-\frac{R}{R_\mathrm{d}}\right) \mathrm{sech}^2\left(\frac{z}{z_0}\right) . \tag{3.58}$$

The disk's scale height z_0 is a fraction f_d of the disk's scale radius R_d. A fraction f_g of the disk consists of gas, the rest consists of an old stellar population. Another fraction m_b of the virial mass forms a spherical bulge with a Hernquist (1993) profile

$$\rho_\mathrm{b} = \rho_\mathrm{b0} \frac{1}{r/r_\mathrm{b}\,(1+r/r_\mathrm{b})^3} \tag{3.59}$$

whose scale radius r_b is again a fraction f_b of the disk's scale radius R_d. The rest of the total mass forms the above-mentioned dark matter halo with a Navarro et al. (1996, 1997) profile

$$\rho_\mathrm{h} = \rho_\mathrm{h0} \frac{1}{r/r_\mathrm{h}\,(1+r/r_\mathrm{h})^2} \tag{3.60}$$

whose scale radius r_h is a fraction c_h^{-1} of the virial radius, where c_h is the halo concentration. The angular momentum of the halo is characterized by a dimensionless spin parameter λ. Setting the disk's angular momentum to a fraction j_d of the halo's angular momentum determines the disk's scale radius R_d.

Thus our galaxy model depends on nine parameters which we list in Table 3.1, we choose our values following Springel and White (1999) and Di Matteo et al. (2005). In our numerical framework of SPH our galaxy consists of an ensemble of particles, we choose 30 000 particles for the halo, 10 000 for the bulge, 20 000 for the stellar disk and 20 000 for the gaseous disk. This or a similar resolution is widely used in SPH simulations of galaxies and galaxy mergers. Springel and Hernquist (2003) use 40 000 SPH particles for the galactic disk, with the dark matter represented by a static gravitational potential. With a resolution study they demonstrate that a galaxy with this resolution level is well posed. Di Matteo et al. (2005) use 30 000 dark matter particles, 20 000 particles for the stellar disk, 20 000 particles for the gaseous disk and 10 000 bulge particles for their merger simulations. Johansson et al. (2009) use 20 000 disk particles, 10 000 bulge particles and 30 000 dark matter particles for their merger simulations and confirm the robustness of their results with resolution tests. Choi et al. (2012) use 20 000 particles for the galactic disk that consists to 20% of gas and 30 000 dark matter particles. They also justify their choice with resolution tests.

v_vir	$160\,\mathrm{km\,s^{-1}}$
m_d	0.041
m_b	0.0137
f_g	0.3
f_d	0.2
f_b	0.1
c_h	15
λ	0.05
j_d	0.041

Table 3.1.: Parameters of our standard galaxy.

In the following we denote a galaxy modeled as described above with parameters as in Table 3.1 as a 'standard galaxy'. Our standard galaxy represents a typical disk galaxy. For example, our Milky Way has a virial velocity of about $142\,\mathrm{km\,s^{-1}}$ (Smith et al., 2007), thus our standard galaxy is slightly more massive than our Milky Way. Furthermore, according to Ostriker et al. (1974), the average mass of a disk galaxy is $10^{12}\,\mathrm{M_\odot}$, our standard galaxy with $v_{\mathrm{vir}} = 160\,\mathrm{km\,s^{-1}}$ has about the same virial mass.

The merger scenario we set up as follows: According to Khochfar (2003) merging dark matter halos are mostly on parabolic orbits. For our merger simulations we therefore set two standard galaxies on a parabolic orbit with a periapsis of $r_{\mathrm{p}} = 5\,\mathrm{kpc}$ and an initial distance of $r_0 = 300\,\mathrm{kpc}$. Thus initially the galaxies are at the positions $\vec{r}_1 = (-150, 0, 0)\,\mathrm{kpc}$ and $\vec{r}_2 = (150, 0, 0)\,\mathrm{kpc}$, respectively. The galactic plane of the second galaxy is parallel to the x-y plane, the first galaxy's galactic plane is rotated by an inclination of $\theta = 30°$ around the y-axis. We will investigate the effects of changing the inclination in section 6.6. In the second galaxy's center we place an AGN particle with mass $10^6\,\mathrm{M_\odot}$, which is equally divided between initial black hole mass and initial accretion disk mass. The size of the AGN particle is set to $R_{\mathrm{AGN}} = 200\,\mathrm{pc}$ where viscous processes start to play a dominant role for the accretion of material onto the black hole. We denote this merger setup as our 'standard model'.

Furthermore we construct a set of 12 merger simulations with different initial galaxy masses, which we denote as our 'standard sample'. These galaxies have virial velocities between $100\,\mathrm{km\,s^{-1}}$ and $320\,\mathrm{km\,s^{-1}}$ in steps of $20\,\mathrm{km\,s^{-1}}$, corresponding to virial masses of $(3\,...\,110) \cdot 10^{11}\,\mathrm{M_\odot}$. This roughly corresponds to observed galaxy masses: Ostriker et al. (1974) measure the mass of dark matter halos of disk galaxies and get values of $(0.1\,...\,100) \cdot 10^{11}\,\mathrm{M_\odot}$. Van der Kruit and Searle (1982) measure the visible component of disk galaxies (i.e., the galactic disk and the bulge) with values of $(11.1\,...\,260) \cdot 10^9\,\mathrm{M_\odot}$. This translates to virial masses of about $(2.2\,...\,52) \cdot 10^{11}\,\mathrm{M_\odot}$ if one assumes that the galactic disk and the bulge contribute to about 5% to the total mass, as is the case for our standard galaxy (see table 3.1).

In this thesis we will focus on equal-mass mergers, i.e., two merging galaxies with the same initial mass. We calculate the AGN masses of these galaxies according to

$$M_{\mathrm{AGN}} = M_{\mathrm{AGN,std}} \frac{M_{\mathrm{vir}}}{M_{\mathrm{vir,std}}} \tag{3.61}$$

where $M_{\mathrm{AGN,std}}$ is the AGN mass and $M_{\mathrm{vir,std}}$ the virial mass of our standard model, respectively. The AGN size and the critical density for the onset of star formation are rescaled in the same manner. In section 5.1 we verify this choice for the critical density, and in section 6.2 we investigate different scaling relations for the AGN size.

4. The general picture

In this chapter we present the general outcome of galaxy mergers using our methodology and our standard sample that we developed in chapter 3. In our discussion we will focus on time lags between starburst and AGN activity and on the M_{BH}-σ correlation.

4.1. Time evolution of the merger event

The time evolution of the merger event is shown in Fig. 4.1 and in Fig. 4.2 we show a compilation of observed galaxy mergers. The galaxies experience their first close passage about 0.7 Gyr after the start of the simulation (Fig. 4.1 B). Due to their gravitational interaction a bridge of gas forms between the two galaxies (Fig. 4.1 C). The galaxies finally merge at about 1.8 Gyr (Fig. 4.1 E).

As the galaxies merge, the gas masses hosted by the galaxies collide and are therefore compressed; the increasing density of the gas encourages star formation and therefore triggers a starburst. Not all of the gas is converted into stars, a fraction of it moves towards the center of the newly forming galaxy, where it forms an accretion disk around the black hole. The gas then needs some time to lose its angular momentum due to the accretion disk's viscosity, it finally arrives at the center where it is swallowed by the black hole.

The luminosity of AGN is proportional to the accretion rate of their central black hole, thus the accretion of the disk's matter by the black hole leads to the activity of the AGN. Therefore the AGN ejects a large amount of energy, that is absorbed by the gas surrounding the AGN. This feedback expels much of the gas from the galaxy, thus quenching further star formation and accretion of material towards the galaxy's center. The feedback shapes the merger remnant into its final form, a gas poor elliptical galaxy (Fig. 4.1 F).

4.2. Star formation and black hole accretion

Fig. 4.3 shows the star formation rate (SFR), the accretion rate of the AGN (AGNAR), and the black hole accretion rate (BHAR) as functions of time for our standard model, i.e., for two merging galaxies with $v_{\rm vir} = 160\,{\rm km\,s^{-1}}$. The merger event is indeed capable

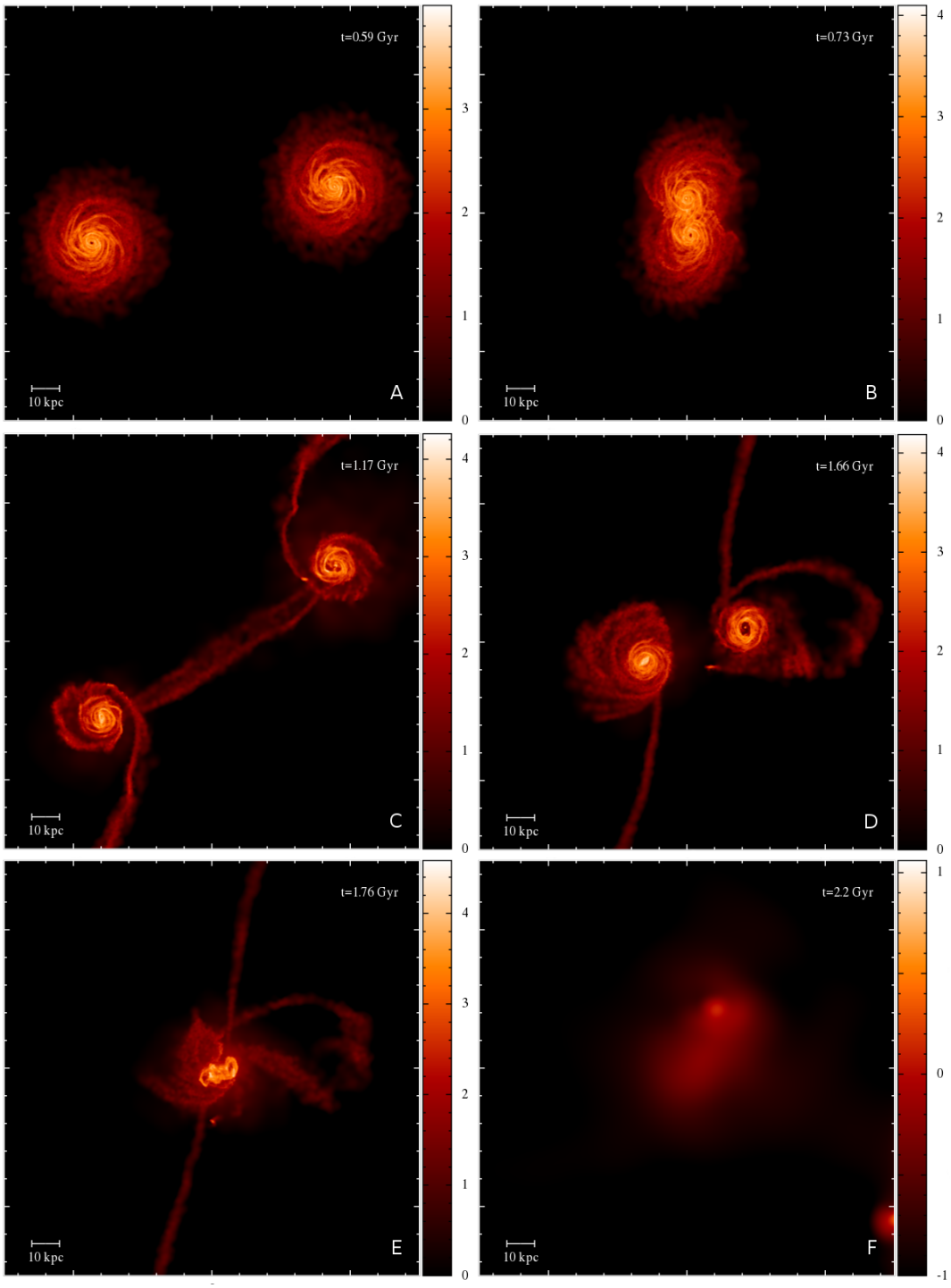

Figure 4.1.: Time development of the merger event. A: the galaxies approach each other; B: galaxies at their periapsis; C: galaxies at their apoapsis; D: the galaxies are just about to merge; E: the galaxies are merging; F: the merger remnant is a gas poor, elliptical galaxy. The color code shows the logarithmic gas density in units of $10^5\,M_\odot\,kpc^{-3}$. The figures were created with the software SPLASH (Price, 2007).

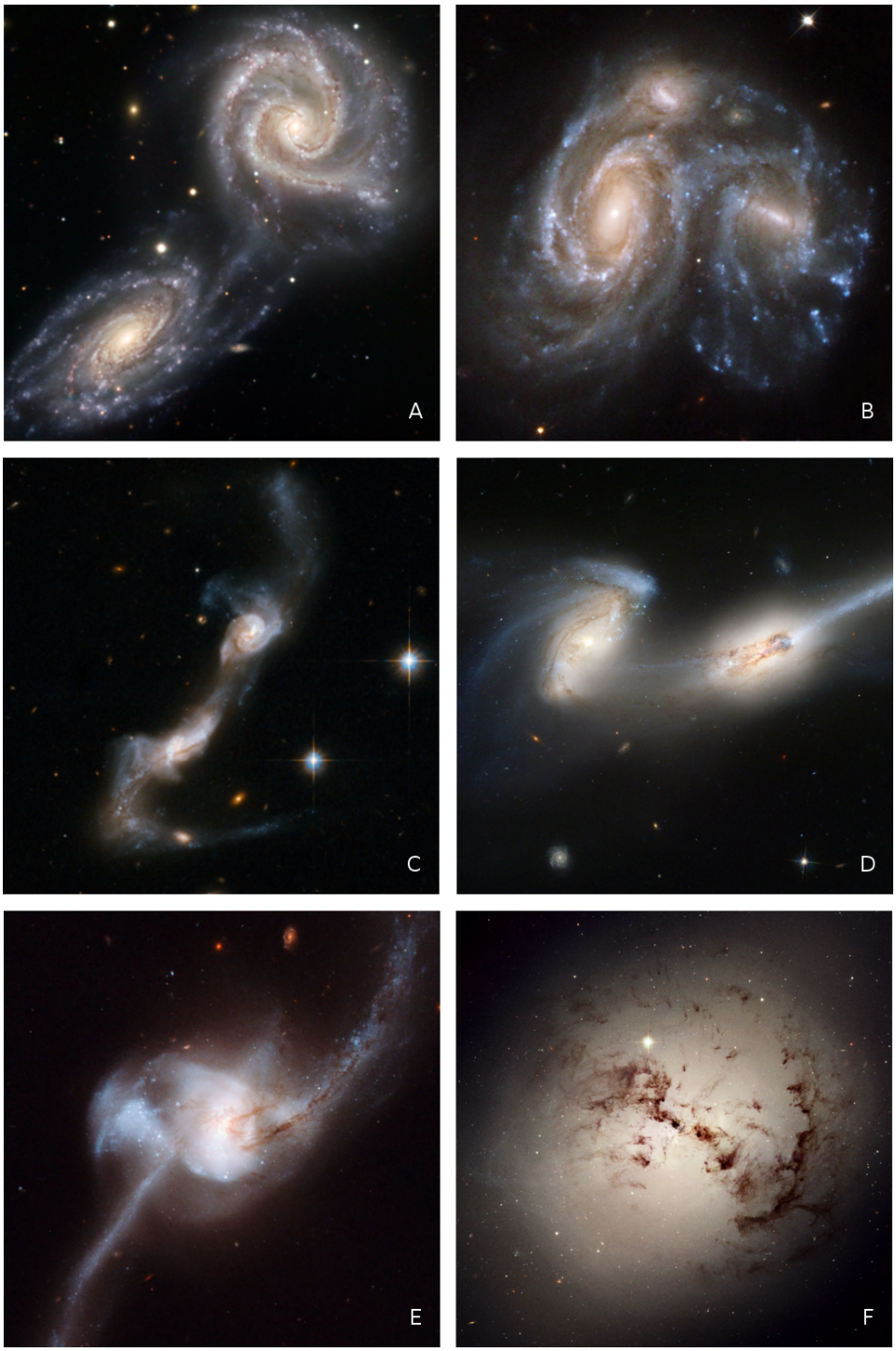

Figure 4.2.: Merging galaxies at approx. the same stages than shown in Fig. 4.1. A: Arp 271; B: Arp 272; C: Arp 238; D: the Mice Galaxies; E: NGC 2623; F: Fornax A. Credits: ESO (Fig. A), NASA/ESA (Figs. B-F).

of producing a starburst (i.e., a peak in the SFR) and AGN activity (i.e., a peak in the BHAR), as has been shown in earlier merger simulations. The starburst has a lifetime of about 200 Myr, in accordance with the observations of Wild et al. (2010) and the simulations of Di Matteo et al. (2005). Also note that at about 0.8 Gyr the first close encounter of the galaxies causes a starburst, but the tidal forces are not strong enough to cause a significant increase in the BHAR.

Contrary to previous merger simulations, the SFR and the BHAR do not peak simultaneously, but Fig. 4.3 shows a time lag between starburst and AGN activity of about 200 Myr that is in agreement with observations. The black line in Fig. 4.3 shows the accretion rate of the AGN, i.e., the mass per time that is swallowed by the AGN particle and added to the outer rim of the accretion disk. The time lag between starburst and AGN activity equals the time lag between the peak of the AGNAR and the peak of the BHAR. This indicates that the time lag between starburst and AGN activity is indeed the time the gas needs to flow through the AGN's accretion disk, thus the time lag can be interpreted as a viscous timescale

$$\tau_{\mathrm{visc}} = \frac{s^2}{\nu} = \frac{1}{\beta\omega} = \frac{1}{\beta}\sqrt{\frac{s^3}{GM}}\,, \tag{4.1}$$

where we have used the β-viscosity prescription (see eq. 3.37 and Duschl et al., 2000), s is the distance to the black hole, i.e., the outer radius of the accretion disk, and M is the mass enclosed by the radius s, i.e., the BH mass plus the mass of the accretion disk.

The AGN feedback quenches the SFR and further inflow of gas towards the center of the newly forming galaxy, noticeable as a quenching of the AGNAR. However, contrary to previous results the BHAR is not quenched, because before the quenching of the AGNAR a huge amount of mass gets inserted into the accretion disk. Thus the disk serves as a reservoir that feeds the BH, even after SFR and AGNAR have been quenched by the AGN feedback. Note that feedback given to the accretion disk is considered by reducing the BHAR according to eq. 3.50.

Fig. 4.4 again shows the star formation rate, the accretion rate of the AGN, and the black hole accretion rate as functions of time, but this time simulated without any AGN feedback. In the absence of feedback SFR and AGNAR are not quenched, thus more mass is inserted into the AGN. The time lag between starburst and AGN activity decreases, because the viscous timescale is proportional to $M^{-0.5}$ and thus decreases with increasing mass. This results in a much larger BHAR[1] compared to the simulation with AGN feedback and thus in a much larger final black hole mass. Indeed, without AGN feedback the final black hole mass far exceeds the BH mass that is suggested by the M_{BH}-σ correlation (see section 6.1).

In Figs. 4.5 and 4.6 we show SFR, BHAR and AGNAR for merging galaxies with $v_{\mathrm{vir}} = 100\,\mathrm{km\,s^{-1}}$ and $v_{\mathrm{vir}} = 320\,\mathrm{km\,s^{-1}}$, respectively. The general picture does not change, SFR and BHAR both peak and AGN activity is delayed with respect to the

[1]Note that in Fig. 4.3 we multiplied the BHAR by 50.

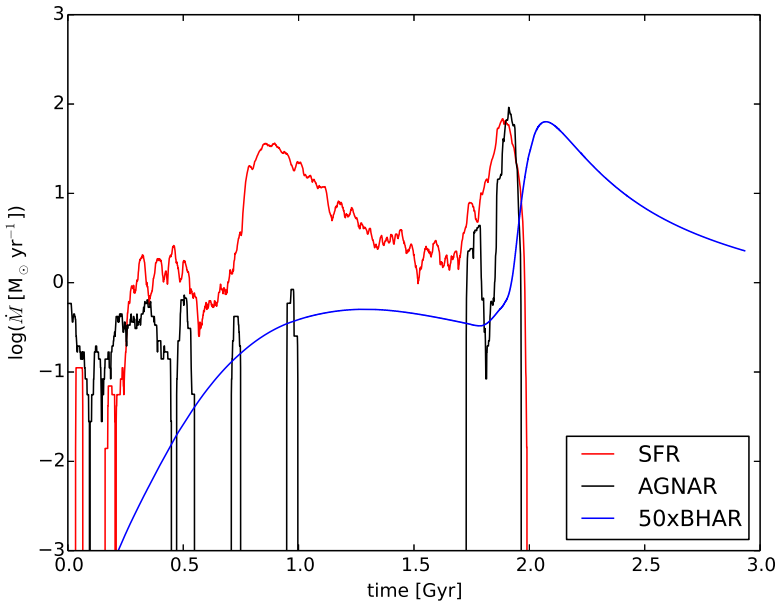

Figure 4.3.: Star formation rate (SFR), accretion rate of the AGN (AGNAR) and black hole accretion rate (BHAR) as functions of time for our standard model with $v_{\mathrm{vir}} = 160\,\mathrm{km\,s^{-1}}$.

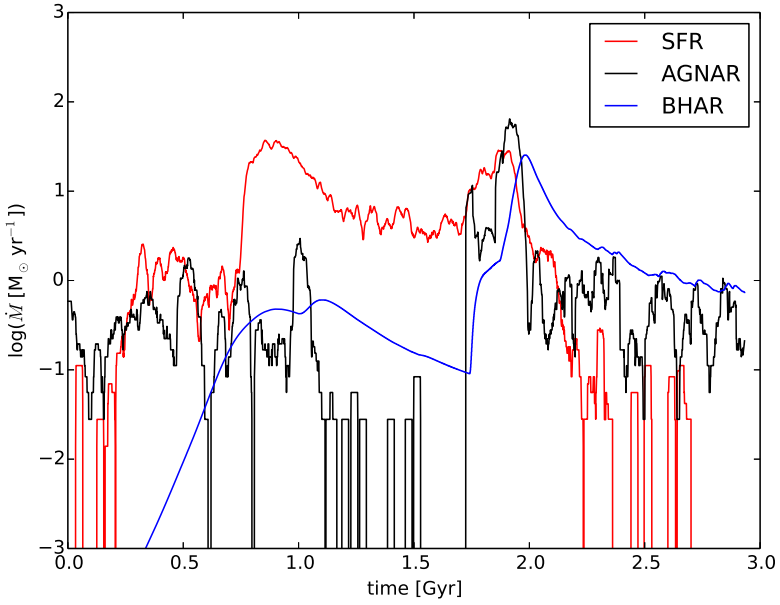

Figure 4.4.: Star formation rate (SFR), accretion rate of the AGN (AGNAR) and black hole accretion rate (BHAR) as functions of time for our standard model with $v_{\mathrm{vir}} = 160\,\mathrm{km\,s^{-1}}$, but without AGN feedback.

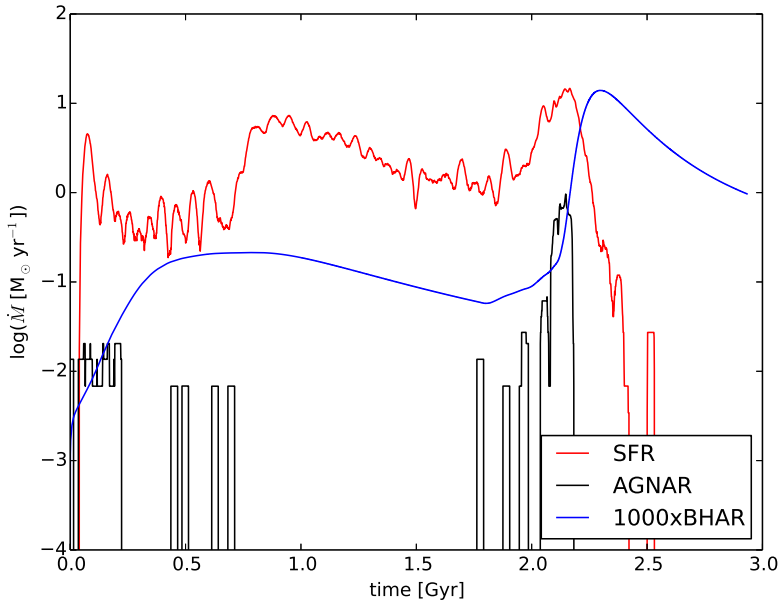

Figure 4.5.: Star formation rate (SFR), accretion rate of the AGN (AGNAR) and black hole accretion rate (BHAR) as functions of time for two galaxies with $v_{\mathrm{vir}} = 100\,\mathrm{km\,s^{-1}}$.

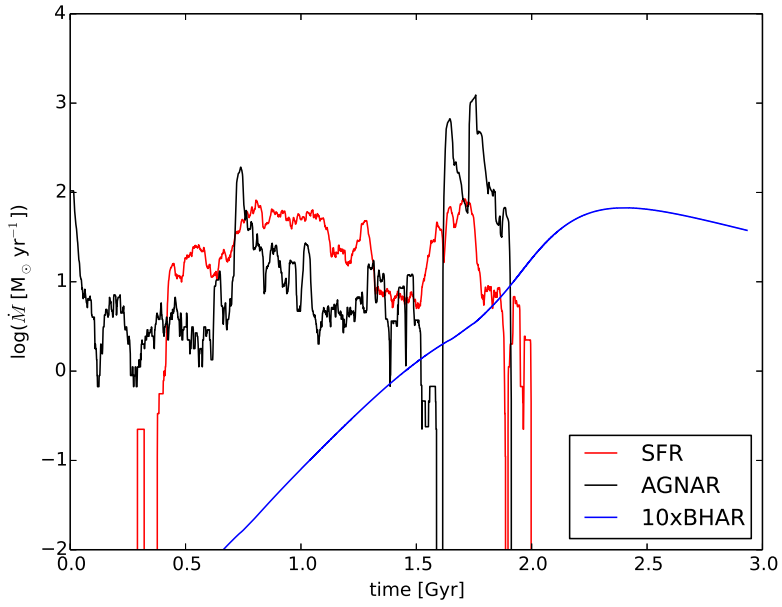

Figure 4.6.: Star formation rate (SFR), accretion rate of the AGN (AGNAR) and black hole accretion rate (BHAR) as functions of time for two galaxies with $v_{\mathrm{vir}} = 320\,\mathrm{km\,s^{-1}}$.

starburst. Furthermore, the SFR and the AGNAR are quenched due to the AGN feedback. However, the magnitude of SFR, BHAR and AGNAR of course changes, as the amount of material that is available for accretion and for star formation increases with increasing virial velocity. Furthermore, the time lag between starburst and AGN activity is shorter for low mass galaxies and larger for high mass galaxies, we will elaborate on this point in section 4.4.

4.3. The M_{BH}-σ correlation

To check the agreement of our model with the M_{BH}-σ correlation we use our standard sample introduced in section 3.7 that consists of 12 galaxy mergers with different initial masses. Fig. 4.7 shows the black hole mass M_{BH} and the merger remnant's stellar velocity dispersion σ for each merger simulation. On how to measure the latter we refer to appendix B. We also plot the observed correlation with intrinsic scatter from Gültekin et al. (2009).

The M_{BH}-σ correlation is usually fitted to a function of the form

$$\log\left(M_{\mathrm{BH}}/\mathrm{M}_{\odot}\right) = b + a \cdot \log\left(\sigma/200\,\mathrm{km\,s^{-1}}\right) \tag{4.2}$$

with slope a and normalization b. We show these parameters in Fig. 4.7 for the observed correlation and for our simulated correlation, both are consistent with each other.

As the BH is constantly growing, before the merger event as well as after the merger event, it is important at which time the black hole mass is determined. We measure the black hole mass at the time the BHAR reaches its maximum value, because as the AGN is most luminous at this time, it is more likely to be detected by observers.

But of course AGN can also be detected at other times, thus we additionally plot the range of BH masses that can be expected in these systems: The vertical bar shown in Fig. 4.7 represents the BH mass from the time of the end of the starburst[2] to the time the BHAR drops to 5% of its maximum value[3], covering a time span of about 1-1.5 Gyr. This range of black hole masses roughly corresponds to the observed scatter, thus the continuing evolution of the black hole after the merger event may contribute to the large observed scatter of the M_{BH}-σ correlation.

4.4. The timing of the starburst-AGN connection

To quantify the timing of the starburst-AGN connection it is necessary to determine the start and the end, and thus the duration of the starburst. In our approach we measure

[2] On how to measure the end of the starburst we refer to section 4.4.

[3] 5% is a rather arbitrary choice, but altering this value to, e.g., 1% or 10% only marginally changes this upper limit.

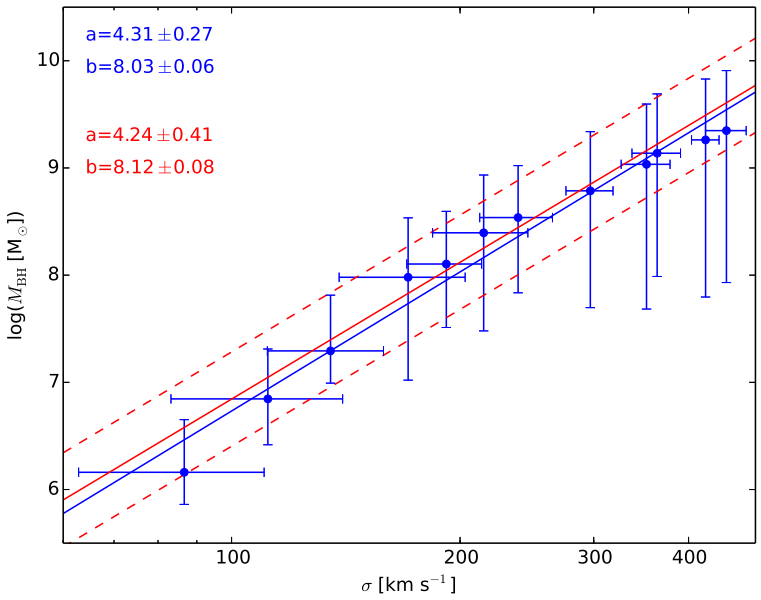

Figure 4.7.: Black hole mass $M_{\rm BH}$ as function of the galaxy's stellar velocity dispersion σ. The blue dots indicate the black hole mass at the time the black hole accretion rate reaches its maximum value, the blue line is a fit to these values. The horizontal bars indicate the error of σ, the vertical bars indicate the range of black hole mass from the time of the end of the starburst to the time the BHAR decreases to 5 % of its maximum value. The red solid line indicates the observed $M_{\rm BH}$-σ correlation with intrinsic scatter (red dashed lines) according to Gültekin et al. (2009).

the 'half mass duration' of the starburst, thus we first determine the time $t_{\rm SB}$ the star formation rate peaks, then the duration of the starburst $\Delta t_{\rm SB}$ is defined such that within the time span $[t_{\rm SB} - \Delta t_{\rm SB}/2,\, t_{\rm SB} + \Delta t_{\rm SB}/2]$, half of the total stellar mass is formed, i.e., such that

$$\frac{M_{*,\rm SB}}{M_{*,\rm tot}} = 0.5\,. \tag{4.3}$$

Here $M_{*,\rm SB}$ is the mass of stars created during the starburst, and $M_{*,\rm tot}$ is the total mass of stars created during the merger event. In section 4.2 we pointed out that the first close encounter of the galaxies causes a starburst as well, so we restrict $M_{*,\rm tot}$ to the stellar mass that is formed between 1.5 Gyr and 3 Gyr. Thus the starburst starts at $t_{\rm SB} - \Delta t_{\rm SB}/2$ and ends at $t_{\rm SB} + \Delta t_{\rm SB}/2$.

In Fig. 4.8 we show the time lag between starburst and AGN activity, i.e., the time from the end of the starburst to the time the BHAR peaks, and the duration of the starburst as functions of σ. The starburst duration is almost independent of σ with a value of about 100 Myr, although there is a slight increase to 150 Myr for low mass galaxies.

The time lag between starburst and AGN activity increases with increasing galaxy mass,

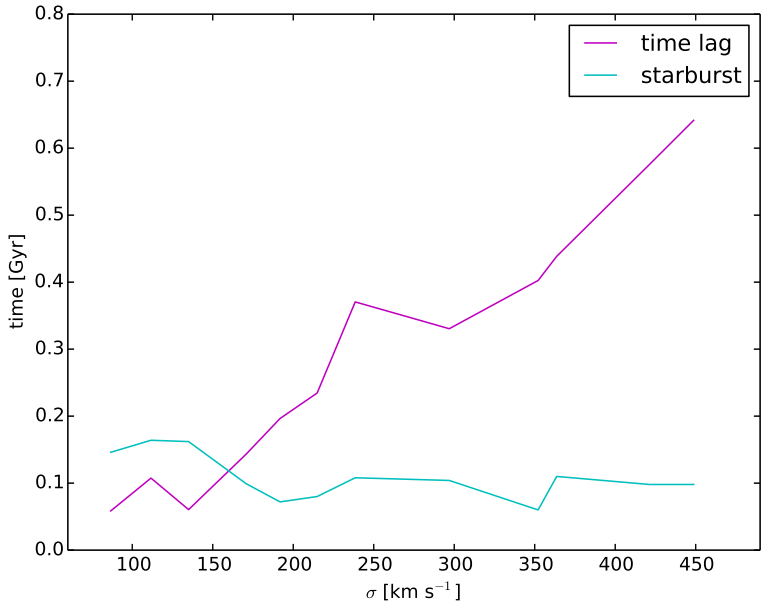

Figure 4.8.: Time lag between starburst and AGN activity and the starburst duration as functions of the galaxy's stellar velocity dispersion σ.

which is primarily caused by our choice of initial conditions. According to section 3.7 and eq. 3.61, both the AGN size and the AGN mass are proportional to the galaxy mass $M_{\rm vir}$. Inserting this into eq. 4.1 for the viscous timescale gives $\tau_{\rm visc} \sim M_{\rm vir}$ and thus explains the time lag increasing with increasing galaxy mass. The scaling of AGN size with galaxy mass has a profound effect on the time lag, which we will elaborate on in section 6.2.

5. Numerical Tests

5.1. Star formation

In this section we test our star formation algorithm, described in section 3.3. The SFR of isolated disk galaxies is known to be roughly constant over large periods of time (several Gyr). According to Kennicutt (1998) the mean SFR in these galaxies can be estimated as

$$\overline{\mathrm{SFR}} = 0.017 \, \frac{M_{\mathrm{gas}}}{\tau_{\mathrm{dyn}}} \, . \tag{5.1}$$

Here M_{gas} is the total gas mass of the galaxy and τ_{dyn} is the orbital timescale at the half gas-mass radius[1], which can be calculated as $\frac{5}{3} R_{\mathrm{d}}$ using the density distribution described by eq. 3.58.

We simulate isolated disk galaxies for a time span of 2 Gyr, using the parameters of our standard sample (see section 3.7). The SFR of our standard galaxy (with $v_{\mathrm{vir}} = 160 \, \mathrm{km \, s^{-1}}$) and the corresponding SFR expected from eq. 5.1 are plotted in Fig. 5.1, showing deviations of less than half an order of magnitude.

In Fig. 5.2 we plot the galaxies' average SFR[2] divided by the SFR expected from eq. 5.1 as function of the virial velocity. Both, the simulated average SFR and the SFR expected from eq. 5.1 differ by less than a factor of two. Our star formation algorithm demonstrates acceptable performance, considering that eq. 5.1 is only an order of magnitude estimate rather than a precise description of the SFR. For instance, eq. 5.1 gives a SFR of $0.72 \, \mathrm{M_\odot \, yr^{-1}}$ for our Milky Way, whereas the observed value is about $2 \, \mathrm{M_\odot \, yr^{-1}}$ (Chomiuk and Povich, 2011).

5.2. The erratic nature of galaxy evolution

Galaxy evolution is in general a very chaotic process, where the galaxy's gas is subject to clumping, fragmentation and the formation of flocculent spiral arms, all driven by gravitational instabilities which are triggered by small-scale density fluctuations. This can lead to large fluctuations in observed quantities of galaxies, like in the SFR, the

[1] This is the radius that encloses half of the galaxy's total gas mass.

[2] This is simply the total mass of stars formed during the simulation divided by the simulation time of 2 Gyr.

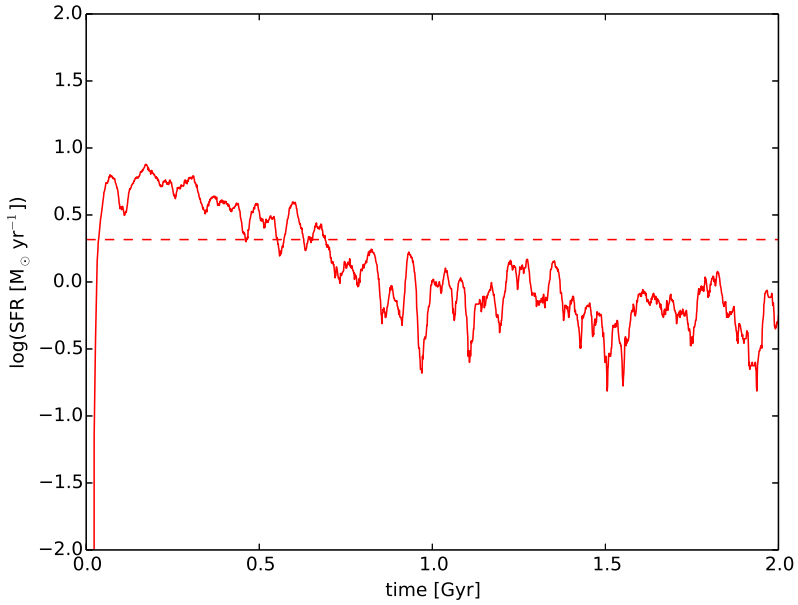

Figure 5.1.: Star formation rates for our standard galaxy. Solid line: simulated SFR, dashed line: SFR according to eq. 5.1.

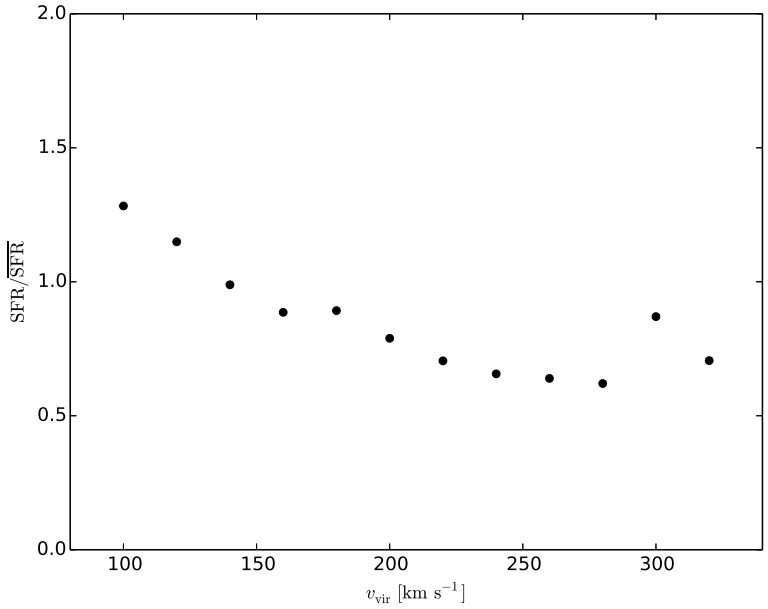

Figure 5.2.: Average SFR from simulations divided by the SFR according to eq. 5.1 for isolated galaxies with different virial velocities.

AGNAR or the BHAR. For example, the SFR of an isolated galaxy shown in Fig. 5.1 shows fluctuations, which is a result of this erratic behavior. Thus galaxies with similar global properties, like, e.g., total mass, gas fraction or size, can have quite different SFRs, AGNARs or BHARs.

Such small-scale density fluctuations are inherently included in our initial conditions: To set up, e.g., a disk with the initial density distribution eq. 3.58 from 20 000 SPH particles, we have to determine the position (r, ϕ, z) of each particle. For this we draw three random numbers from the interval $[0, 1]$, as the density distribution is uniform in the azimuthal direction we multiplicate the first random number with 2π to get the angular coordinate of the particle. For the r and z coordinate the respective random numbers have to be weighted with spatial distribution functions that are derived from the density distribution. Repeating this procedure for all particles gives a density distribution that follows eq. 3.58, but includes small-scale density fluctuations. These fluctuations influence the evolution of galaxies and galaxy mergers, and changing the sequence of random numbers will change these initial fluctuations and thus also change the evolution of these systems. We emphasize that this in not a purely numerical effect, as these fluctuations are indeed observed in galaxies. But of course, numerical effects, like, e.g., insufficient resolution, can increase these fluctuations and thus influence galaxy evolution.

To quantify the erratic nature of galaxy evolution we simulate six galaxy mergers using the parameters of our standard model, each using different random number sequences. In Fig. 5.3 we show the total stellar mass, i.e., the integrated SFR, and in Fig. 5.4 the AGN mass as functions of time for these six merger simulations. The deviations among the simulations are quite large. The average final AGN mass is $M_{\mathrm{AGN}} = (22 \pm 6) \cdot 10^8\,\mathrm{M}_\odot$ and the average final stellar mass is $M_* = (175 \pm 10) \cdot 10^8\,\mathrm{M}_\odot$. These deviations also introduce fluctuations on other quantities, especially on the starburst timing, and thus on the time lag between starburst and AGN activity and on the starburst duration. This can be seen in Fig. 4.8, as the time lag and the starburst duration are not smooth functions of the stellar velocity dispersion. We have to take the erratic nature of galaxy evolution into consideration when interpreting our results. In certain cases these fluctuations dominate our results, so that it is only possible to make statements of a general nature.

5.3. AGN particle

The AGN particle of our standard model has an initial mass of $10^6\,\mathrm{M}_\odot$, whereas one gas particle has a mass of about $6 \cdot 10^5\,\mathrm{M}_\odot$. Thus the AGN particle's mass exceeds the mass of a gas particle by less than a factor of two, at least at the start of the simulation. This small ratio can lead to stochastic motions of the AGN particle due to its interaction with its surrounding particles, because when accreting a gas particle the AGN particle absorbs not only the particle's mass, but its momentum as well. Debuhr et al. (2011) call this effect the 'Brownian motion' of the AGN particle. The gravitational interaction

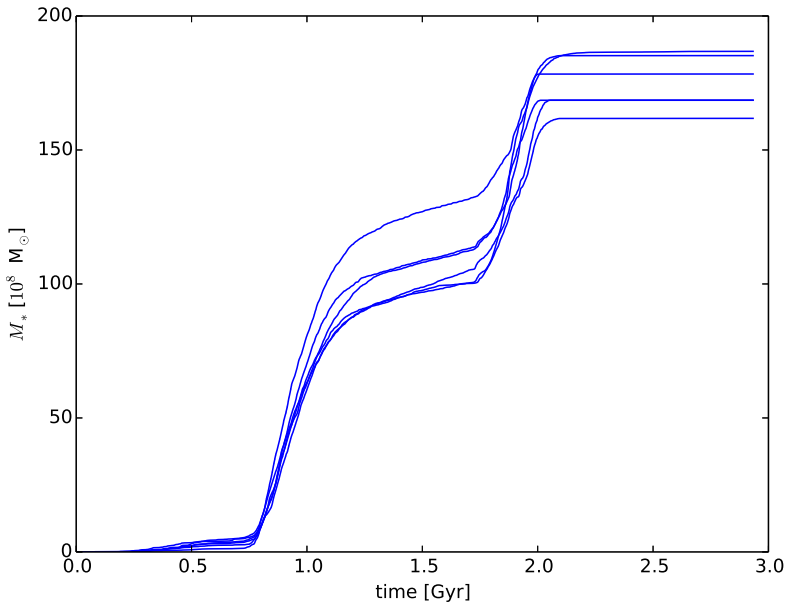

Figure 5.3.: Total stellar mass as function of time for our standard model using six different random number sequences.

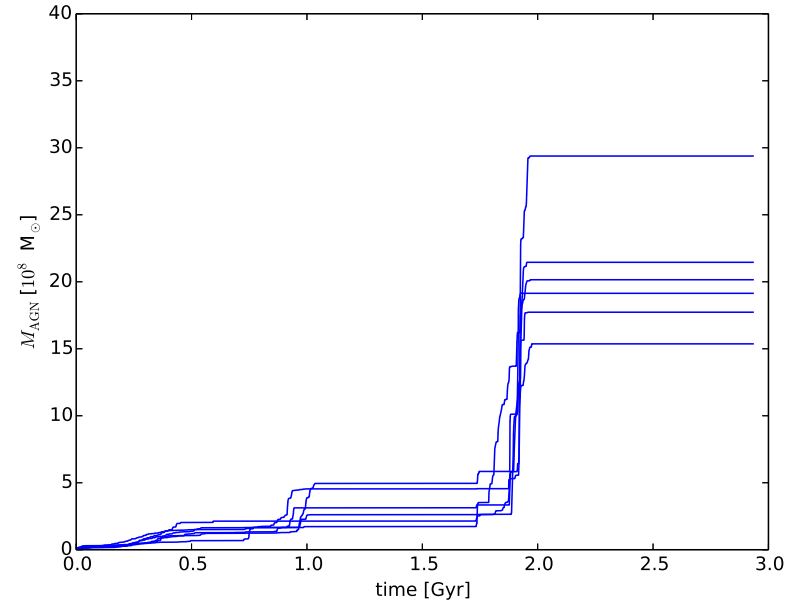

Figure 5.4.: AGN mass as function of time for our standard model using six different random number sequences.

with the surrounding particles also contributes to this effect. This Brownian motion can artificially increase the accretion rate of the AGN particle.

Several methods have been developed to compensate for this purely numerical effect. For example, Debuhr et al. (2011) suggest giving the AGN particle a large 'tracer' mass, that is about 100 times larger than the 'internal' mass, which in our model is the sum of black hole mass and accretion disk mass. Another method is to calculate the galaxy's center of mass and relocate the AGN particle to this position after each time step, likewise the AGN particle's velocity is set to the velocity of the galaxy's center of mass. However, this method is difficult to apply in merger simulations, as at a specific point in time one has to switch from relocating the AGN to the center of its original galaxy to relocating the AGN to the center of the newly forming galaxy. This transition can lead to an unrealistic behavior of the AGN particle if the two centers are not co-located.

We test both approaches by first simulating isolated galaxies using our standard parameters. Fig. 5.5 shows the AGN particle's mass versus time using the 'tracer' approach, the 'relocation' approach, for using both approaches simultaneously and for using no compensation for Brownian motion. Without compensation the AGN particle accumulates about $5 \cdot 10^8\,\mathrm{M}_\odot$ within 3 Gyr, the relocation approach reduces its mass to $3 \cdot 10^8\,\mathrm{M}_\odot$ and the tracer approach to about $1 \cdot 10^8\,\mathrm{M}_\odot$. Using both approaches simultaneously gives about the same final mass as the tracer approach, but most of the time the AGN mass is larger when using both approaches simultaneously. Thus the tracer approach shows the best performance in reducing the accretion rate of the AGN particle.

We also simulate a galaxy merger using our standard model and the tracer approach and show the AGN mass as function of time in Fig. 5.5, together with the average final AGN mass of $2.2 \cdot 10^9\,\mathrm{M}_\odot$ calculated in section 5.2. This time the tracer approach gives a larger final AGN mass, contrary to our simulations with isolated galaxies. We have not taken the fluctuations due to the erratic nature of galaxy evolution into account here, which probably exceed the deviations induced by the AGN particle's Brownian motion. To decide with certainty between the effects of Brownian motion and erratic fluctuations, it would be necessary to calculate an average final AGN mass for the simulations with the tracer approach in the same manner than in section 5.2.

However, we decided not to use any of the techniques presented in this section and accept a slight increase of the AGN particle's accretion rate, because of the following reasons:

(I) The deviations due to the AGN particle's stochastic motion seem to be smaller than the derivations due to the erratic nature of galaxy evolution.

(II) Both approaches violate fundamental principles of physics, the tracer approach violates mass conservation and the relocation approach violates momentum conservation.

(III) The methods presented in this section aim to decrease the inflow of material towards the galaxy's center. However, even isolated galaxies show an inflow of material towards their center, e.g., our Milky Way was able to build a $4 \cdot 10^6\,\mathrm{M}_\odot$ black hole within a Hubble time. So one must be careful that the applied methods do not underestimate

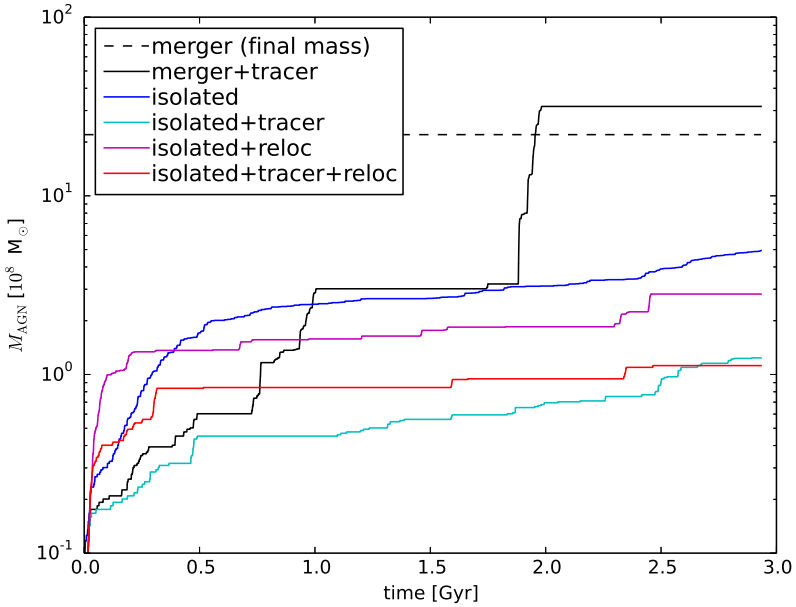

Figure 5.5.: AGN masses as functions of time for simulations of mergers and isolated galaxies using our standard parameters. We test the 'tracer' approach and the 'relocation' approach to suppress the 'Brownian motion' of the AGN particle.

the accretion flow. It has indeed been shown that the tracer approach suppresses the accretion flow to unrealistically low values.

(IV) In Figs. 5.6 and 5.7 we show the SFR, BHAR, AGNAR and the $M_{\rm BH}$-σ correlation once with and once without using the tracer approach. Both methods show acceptable deviations from each other.

5.4. Two AGN particles

In our standard model only one of the merging galaxies hosts an AGN particle in its center. However, it is now widely accepted that almost all massive galaxies host a black hole in their centers (Magorrian et al., 1998), thus our models would be more realistic with both galaxies hosting an AGN particle. In this chapter we present the results of such a calculation and show that the differences are small compared to our standard model, which justifies the use of only one AGN particle.

At some time during the merger event these two particles have to merge themselves, several methods have been developed to accomplish this (e.g., Springel et al., 2005; Booth and Schaye, 2009). We use two criteria that have to be fulfilled, first, the distance

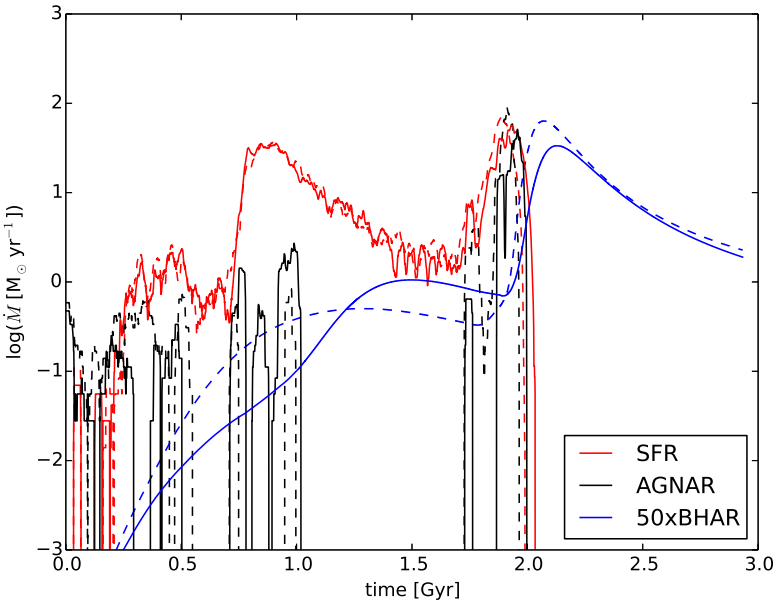

Figure 5.6.: SFR, AGNAR and BHAR as functions of time for our standard model with (solid lines) and without (dashed lines) applying the 'tracer' method.

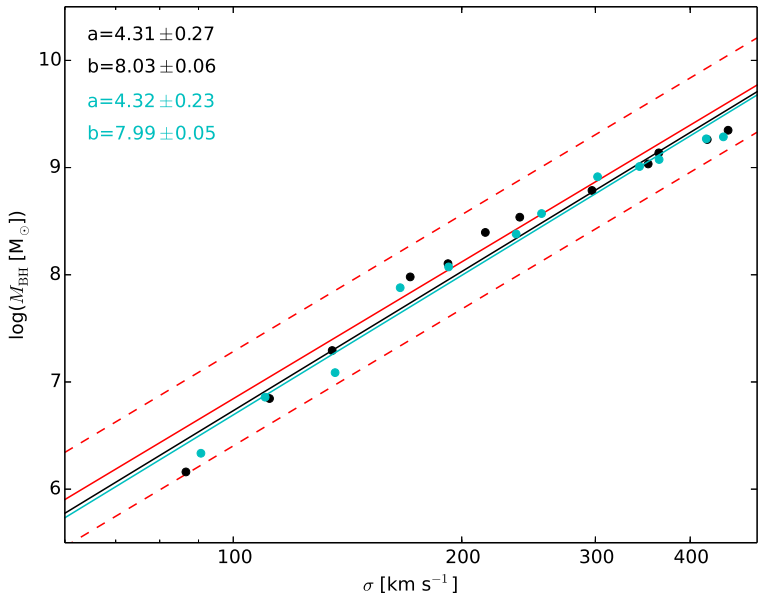

Figure 5.7.: $M_{\rm BH}$-σ correlation for our standard sample with (cyan) and without (black) applying the 'tracer' method.

between the particles has to be smaller than the AGN radius, and second, their binding energy

$$E = \frac{1}{2}\left(m_1 v_1^2 + m_2 v_2^2\right) - \frac{G m_1 m_2}{2r} \tag{5.2}$$

has to be smaller than zero, i.e., the particles are gravitationally bound to each other. Here m_1 and m_2 are the masses and v_1 and v_2 are the velocities (in a frame of reference where the center of mass of the two particles is at rest) of the AGN particles, respectively, and r is the distance between the particles. If these two criteria are fulfilled, the two AGN particles are replaced by one AGN particle whose mass is the sum of the preceding particles masses, and which has the position and the velocity of the center of mass of the preceding particles. In our model the AGN particle hosts a black hole and an accretion disk. The black hole mass of the resulting AGN particle is simply the sum of the black hole masses of both preceding particles. The resulting particles' accretion disk has the same radius as the preceding ones, its surface density is calculated by summing up the surface density profiles of both preceding particles.

In Fig. 5.8 we show SFR and BHAR and in Fig. 5.9 the M_{BH}-σ correlation in comparison with the results of our standard sample. The resulting black hole masses are slightly larger when using two AGN particles, because, firstly, it contains the initial mass of the second AGN particle, and secondly, the second AGN particle additionally accretes some material before it merges with the first AGN particle. But the differences are not very large, the M_{BH}-σ correlation is still within the observed error bounds. Thus it is justified to only use one AGN particle.

It is currently a matter of intense debate how black holes and especially accretion disks merge. So far no observational evidence has been obtained for such events, and also theoretical work tackling this problem is rare. Thus we prefer to use only one AGN particle to avoid adding a number of additional assumptions to our model that we can not verify due to the absence of theoretical work or observations in that regard.

5.5. AGN feedback radius

In section 3.6 we set the feedback radius r_{fb}, where the feedback energy is distributed among the gas particles within this radius, to $2R_{\mathrm{AGN}}$, which is a rather arbitrary choice. In this section we present calculations where this radius has been doubled, i.e., $r_{\mathrm{fb}} = 4R_{\mathrm{AGN}}$. Fig. 5.10 shows SFR, BHAR and AGNAR and Fig. 5.11 the M_{BH}-σ correlation compared to the results of the standard sample. There are no significant differences, thus the detailed choice of the feedback radius is not important. It is rather the amount of energy that is deposited in the surrounding gas that has a significant effect on the results.

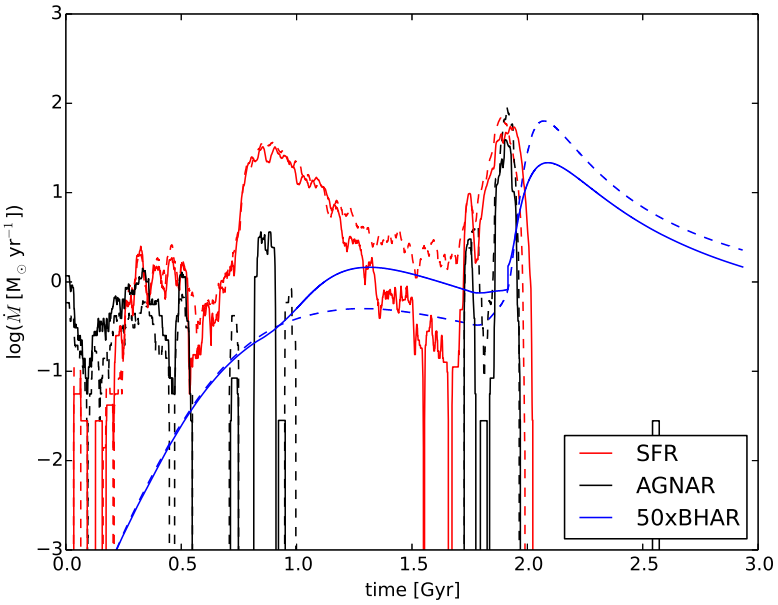

Figure 5.8.: SFR, AGNAR and BHAR as functions of time for our standard model using one (dashed lines) and two (solid lines) AGN particles.

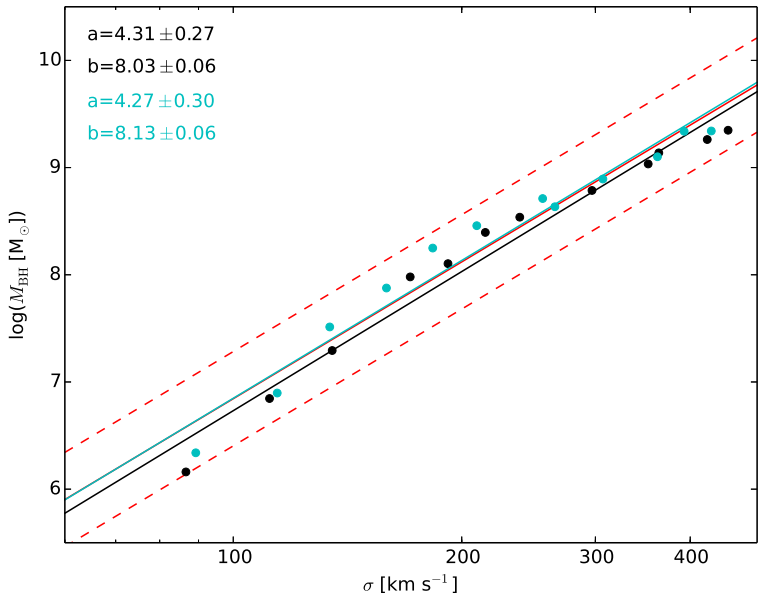

Figure 5.9.: $M_{\rm BH}$-σ correlation for our standard model using one (black) and two (cyan) AGN particles.

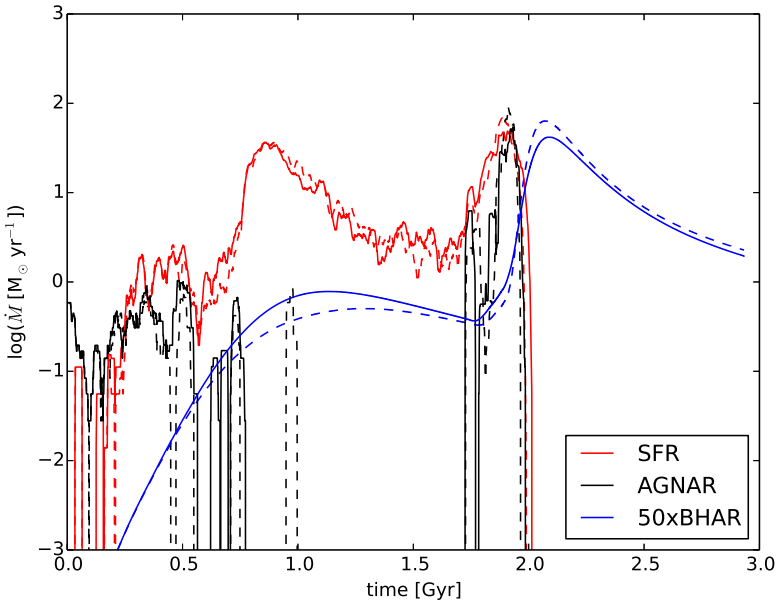

Figure 5.10.: SFR, AGNAR and BHAR as functions of time for our standard model using $r_{\rm fb} = 2R_{\rm AGN}$ (dashed lines) and $r_{\rm fb} = 4R_{\rm AGN}$ (solid lines).

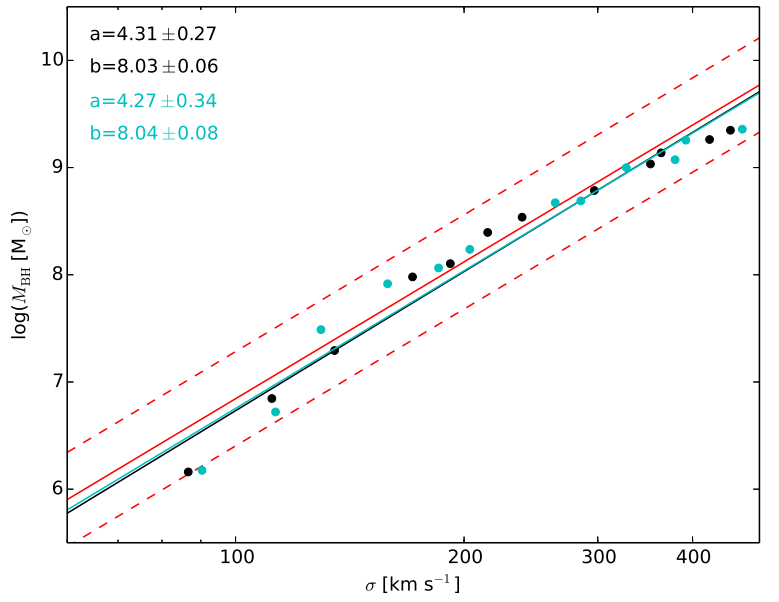

Figure 5.11.: $M_{\rm BH}$-σ correlation for our standard sample using $r_{\rm fb} = 2R_{\rm AGN}$ (black) and $r_{\rm fb} = 4R_{\rm AGN}$ (cyan).

6. Parameter study

Our galaxy model and our algorithms depend on a number of parameters, some of which are not well constrained by observations or show large variations among different galaxies. Thus it is necessary to test the robustness of our results to the variation of these parameters. We choose a set of parameters where we expect the most significant changes to occur, namely the parameter τ_{w} that determines the strength of AGN feedback, the scaling of the AGN size with galaxy mass, the β-parameter for the turbulent viscosity, the AGN size R_{AGN}, the gas fraction f_{gas} of the galaxies' disks and the inclination θ of one of the galaxies. We explore the effects on the M_{BH}-σ correlation, on the time lag between starburst and AGN activity and on the starburst duration. In a handful of simulations the erratic nature of galaxy evolution causes time lags between starburst and AGN activity that have small negative values, we ignore those for the analyses presented in this chapter.

6.1. Effect of AGN feedback

To investigate the effect of AGN feedback we vary the parameter τ_{w} that determines the strength of the wind that is ejected by the AGN according to eqs. 3.47 and 3.49. Variations of the parameter τ_{rad}, that describes the feedback due to the AGN's radiation, and the parameter τ_{w} have been investigated in Debuhr et al. (2011), in this study only the normalization b of the M_{BH}-σ correlation changes, its slope a remains unchanged. Less feedback leads to larger values of b, as less mass is removed by the feedback, and conversely more feedback leads to smaller values of b.

Here we investigate models with $\tau_{\mathrm{w}} = 1, 5, 7$, the standard model with $\tau_{\mathrm{w}} = 3$ and one model without any AGN feedback. The upper left part of Fig. 6.1 shows the M_{BH}-σ correlation for the model without AGN feedback. The normalization b indeed increases, i.e., the black hole swallows more mass, but the slope a also changes, contrary to the results of Debuhr et al. (2011).

The change of the slope a can be explained by invoking the time lag between starburst and AGN activity: For high mass galaxies feedback does not have a large effect on the galaxy, as due to the large time lag the feedback is only effective a long time after the merging event. During this time, most of the gas is inserted into the AGN or used for star formation, thus at the time the BHAR peaks there is not much mass left that can

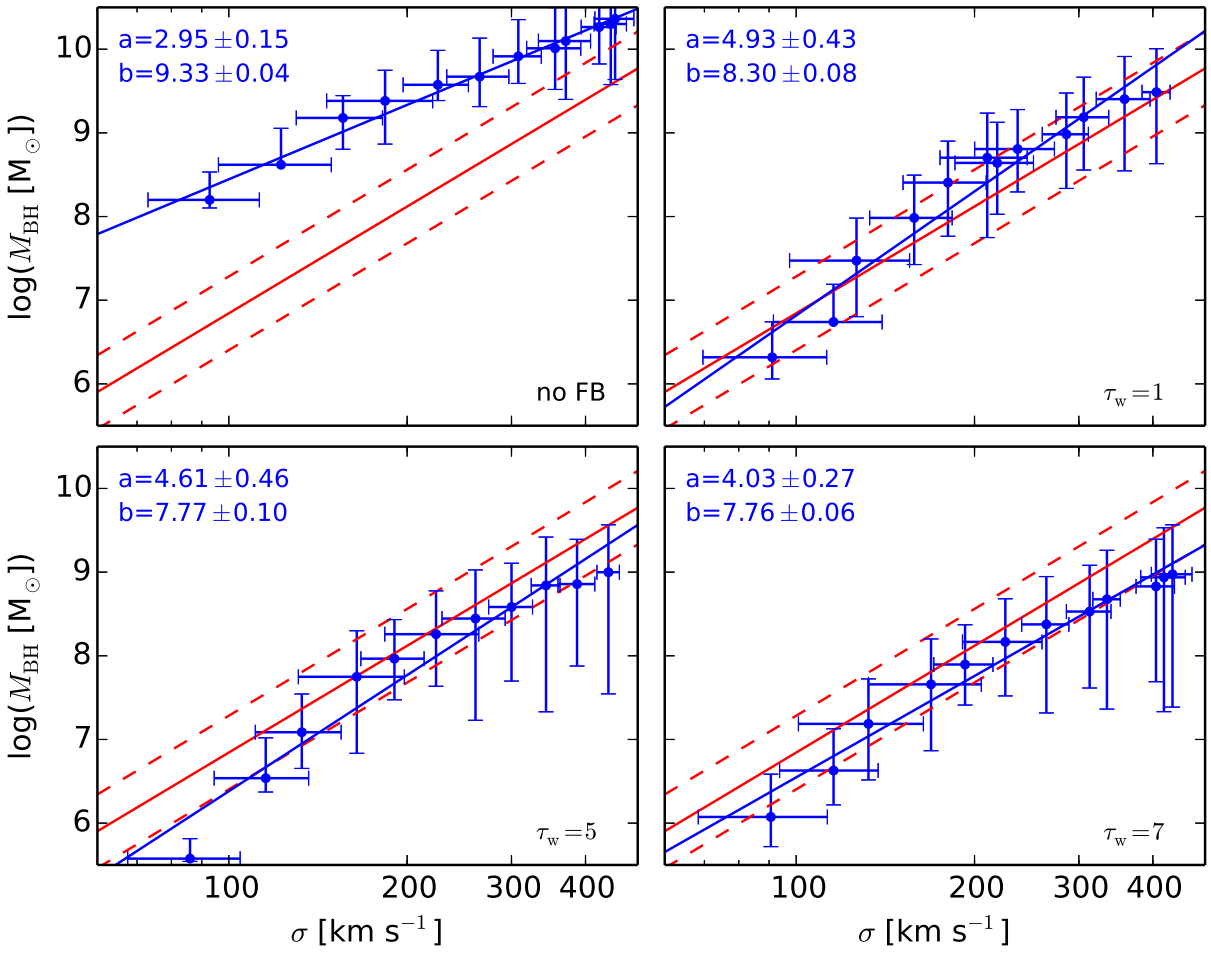

Figure 6.1.: M_{BH}-σ correlation for different modes of AGN feedback.

be removed by the feedback. Thus without feedback the black hole mass in high mass galaxies only increases by about one order of magnitude.

For low mass galaxies the time lag is much shorter, thus at the time the BHAR peaks there is still a huge amount of gas residing close to the AGN, which then gets ejected due to the AGN feedback. Without feedback all this mass is accreted by the AGN and thus the black hole mass increases by two orders of magnitude when compared to the model with feedback.

As less feedback leads to a larger AGN mass, one would expect a smaller time lag, because the viscous timescale is proportional to $M^{-0.5}$ (eq. 4.1). Fig. 6.2 shows that this is indeed true when comparing the model without AGN feedback with the standard model, but the time lags for the models with $\tau_w = 1, 3, 5, 7$ are not distinguishable from each other, as their scatter is very large. This is explained by Fig. 6.3, which shows the

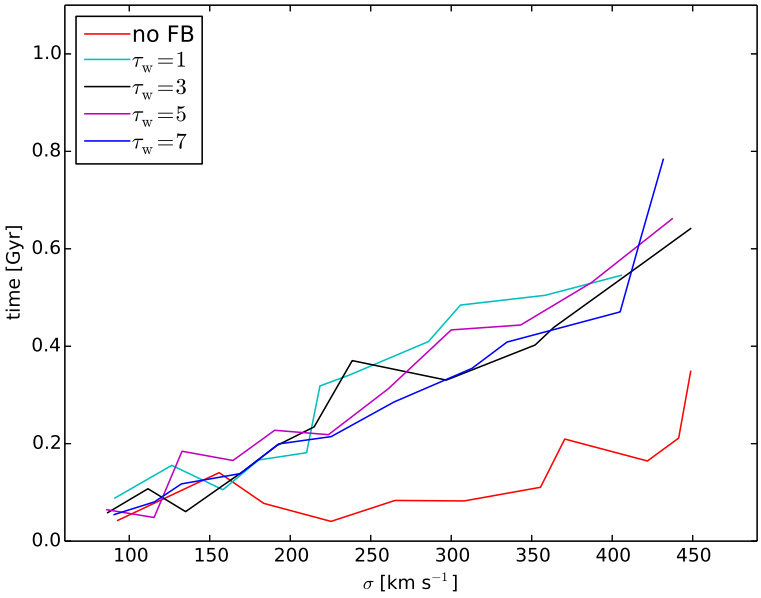

Figure 6.2.: Time lag between starburst and AGN activity for different modes of AGN feedback.

BHAR as function of time for the galaxies with $v_{\rm vir} = 320\,{\rm km\,s^{-1}}$. First we see that in the model without AGN feedback the BHAR peaks much earlier than in the models with feedback as expected. Likewise the BHAR for the models with $\tau_{\rm w} = 1, 3, 5, 7$ peaks earlier with smaller $\tau_{\rm w}$, but the difference is small. The erratic nature of merger evolution introduces a large scatter on the timing of the starburst that is transferred to the time lag between starburst and AGN activity, thus in Fig. 6.2 the time lags for the models with $\tau_{\rm w} = 1, 3, 5, 7$ are indistinguishable. However, Fig. 6.3 shows the BHAR being larger with decreasing $\tau_{\rm w}$, which translates directly to the black hole mass being larger with decreasing $\tau_{\rm w}$ for all times.

Fig. 6.4 shows the BHAR as function of time for the galaxies with $v_{\rm vir} = 120\,{\rm km\,s^{-1}}$. First for all models the BHAR peaks at approx. the same time, corresponding to the time lags in Fig. 6.2 having approx. the same value. Furthermore, there is no clear trend for the BHAR being larger or smaller with decreasing $\tau_{\rm w}$, different to the BHAR for high mass galaxies (Fig. 6.3). For low mass galaxies any such trend is completely washed out by the erratic nature of merger evolution. As for high mass galaxies the BH mass slightly increases with decreasing

$\tau_{\rm w}$	a	b
no FB	2.95 ± 0.15	9.33 ± 0.04
1	4.93 ± 0.43	8.30 ± 0.08
3	4.31 ± 0.27	8.03 ± 0.06
5	4.61 ± 0.46	7.77 ± 0.10
7	4.03 ± 0.27	7.76 ± 0.06

Table 6.1.: Parameters of the $M_{\rm BH}$-σ correlation for varying AGN feedback.

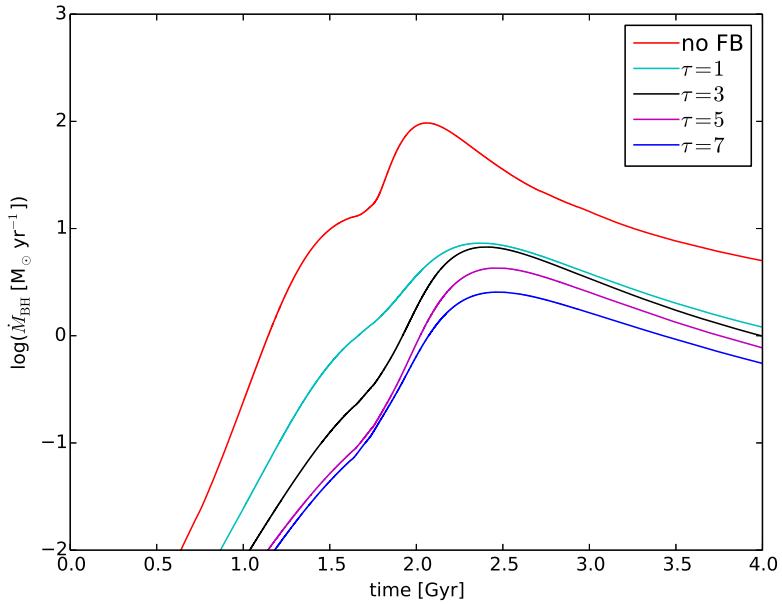

Figure 6.3.: Black hole accretion rate for galaxies with $v_{\rm vir} = 320\,{\rm km\,s^{-1}}$ for different modes of AGN feedback.

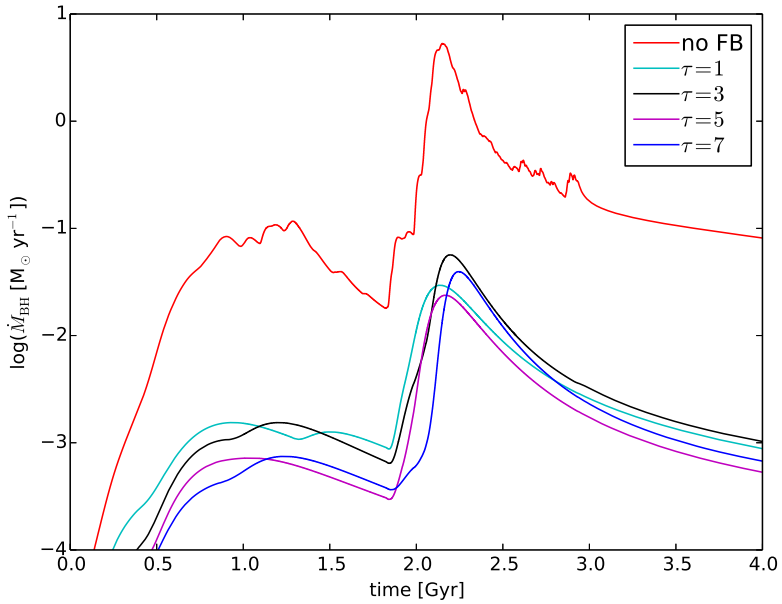

Figure 6.4.: Black hole accretion rate for galaxies with $v_{\rm vir} = 120\,{\rm km\,s^{-1}}$ for different modes of AGN feedback.

$\tau_{\rm w}$, and for low mass galaxies there is no clear trend, it is expected that the slope a of the $M_{\rm BH}$-σ correlation increases with decreasing $\tau_{\rm w}$. This is only roughly confirmed by Fig. 6.1, which also shows the $M_{\rm BH}$-σ correlation for $\tau_{\rm w} = 1, 5, 7$, and by table 6.1 that shows the parameters a and b of the $M_{\rm BH}$-σ correlation. But table 6.1 shows that the normalization b clearly increases with decreasing $\tau_{\rm w}$, confirming the general trend pointed out by Debuhr et al. (2011).

It might seem paradoxical at first sight that the slope a increases with decreasing $\tau_{\rm w}$, but decreases for the model without feedback, when compared to the standard model or the observed $M_{\rm BH}$-σ correlation. This is because two different physical effects come into play here. The change of the slope for the model without feedback is caused by the change in the time lag. For the models $\tau_{\rm w} = 1, 3, 5, 7$ the time lag does not change significantly, here the slope a is changing because the black hole mass of high mass galaxies increases with decreasing $\tau_{\rm w}$, whereas the black hole mass of low mass galaxies only shows erratic changes.

In summary, decreasing $\tau_{\rm w}$ leads to an increased black hole mass and the slope a of the $M_{\rm BH}$-σ correlation also increases slightly. The time lag between starburst and AGN activity is not affected, as changes are much smaller than the scatter of this relation.

6.2. Scaling of AGN size

In section 3.7 we assumed that the radius of the AGN $R_{\rm AGN}$ is proportional to the galaxy's mass $M_{\rm vir}$. Other scaling relations are possible, for example the AGN radius being proportional to the galaxy's scale radius $R_{\rm vir}$, thus being proportional to $M_{\rm vir}^{1/3}$.

We generalize our scaling relation as

$$R_{\rm AGN} = R_{\rm AGN,std} \left(\frac{R_{\rm vir}}{R_{\rm vir,std}} \right)^f , \tag{6.1}$$

thus a value of $f = 3$ represents our standard model. In this section we explore models with $f = 0, 1, 1.5, 2$.

Using $R_{\rm AGN} \sim M_{\rm vir}^{f/3}$ and $M_{\rm AGN} \sim M_{\rm vir}$ in the equation for the viscous time lag (eq. 4.1) and considering $M_{\rm vir} \sim \sigma^3$ (eq. B.11) yields

$$\tau_{\rm visc} = \beta^{-1} \sqrt{\frac{R_{\rm AGN}^3}{G M_{\rm AGN}}} \sim \sqrt{M_{\rm vir}^{f-1}} \sim \sigma^{\frac{3}{2}(f-1)} \tag{6.2}$$

or

$$\tau_{\rm visc} = \tau_0 \left(\frac{\sigma}{\sigma_{\rm std}} \right)^\alpha \tag{6.3}$$

with $\alpha = \frac{3}{2}(f-1)$.

Thus we expect the slope of the time lag as a function of σ to decrease with decreasing f, which is indeed confirmed by Fig. 6.5.

However, fitting the curves in Fig. 6.5 to the relation implied by eq. 6.3 and comparing the slope α to the expected value of $\frac{3}{2}(f-1)$ (see table 6.2) shows that α is greatly underestimated. To derive eq. 6.3 we assumed the AGN mass being proportional to the galaxy's virial mass. This is certainly true for the start of the simulation, as we impose this as initial condition, but as the merger event proceeds this proportionality is broken. More massive galaxy mergers drive overproportionately more mass into their AGN, i.e., galaxies with double the mass of our standard model drive *more* than double the mass into their AGN. This larger AGN mass leads to smaller time lags for high mass galaxies, and thus reduces the slope α of the time lag as function of σ as shown in Fig. 6.5.

This effect is also shown in Fig. 6.6 where we plot the 'rescaled' AGN mass

$$M_{\mathrm{AGN,sc}} = \left(\frac{M_{\mathrm{vir}}}{M_{\mathrm{vir,std}}}\right)^{-1} M_{\mathrm{AGN}} \tag{6.4}$$

as a function of time for different galaxies of our standard sample. Comparison with eq. 3.61 shows that at the start of the simulation this quantity is identical for all galaxies of our standard sample, and would stay so if the mass swallowed by the AGN would be strictly proportional to the masses of their galaxies. However, Fig. 6.6 shows large differences in this quantity, thus confirming that more massive galaxy mergers drive overproportionately more mass into their AGN.

Fig. 6.7 shows the M_{BH}-σ correlations for the $f = 0, 1, 1.5, 2$ models, and table 6.3 their values for slope a and normalization b. The normalization does not change significantly, but the slope decreases strongly with decreasing f.

This again is an effect caused by the time lags changing with galaxy mass, and its reason follows the same argument as the previous section: A smaller value of f gives a smaller (larger) time lag for high mass (low mass) galaxies, thus the feedback sets in earlier (later) and removes more (less) mass from the galaxy, leaving less (more) mass for the BH. Thus for high mass galaxies the BH mass decreases, and for low mass galaxies the BH mass increases, which therefore decreases the slope a of the M_{BH}-σ correlation.

f	α	$\frac{3}{2}(f-1)$
0	-1.52 ± 0.21	-1.5
1	-0.60 ± 0.14	0
1.5	-0.18 ± 0.09	0.75
2	0.53 ± 0.08	1.5
3	1.47 ± 0.15	3

Table 6.2.: Predicted and measured exponent for the time lag.

f	a	b
0	2.37 ± 0.16	7.90 ± 0.03
1	3.32 ± 0.13	8.09 ± 0.02
1.5	3.89 ± 0.13	8.04 ± 0.03
2	3.94 ± 0.15	8.05 ± 0.03
3	4.31 ± 0.27	8.03 ± 0.06

Table 6.3.: Parameters of the M_{BH}-σ correlation for different scalings f.

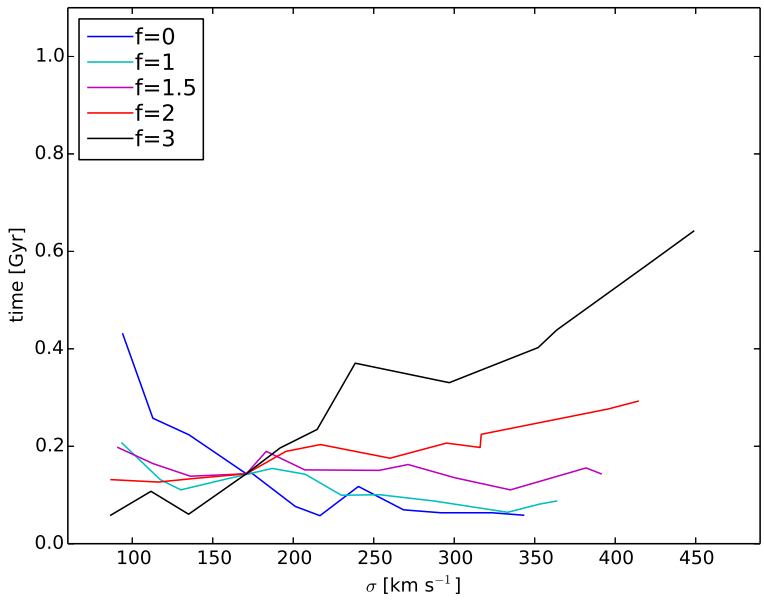

Figure 6.5.: Time lag between starburst and AGN activity for different values of the scaling f.

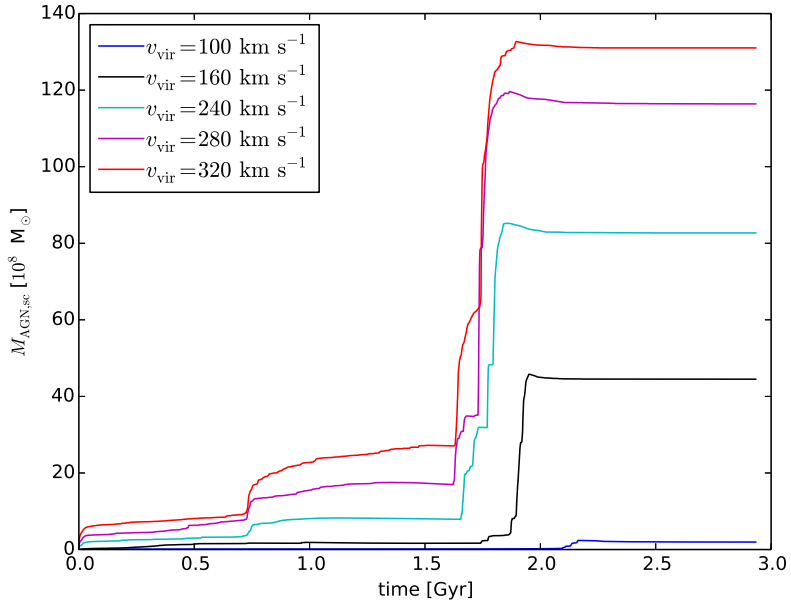

Figure 6.6.: Rescaled AGN masses as functions of time for different virial velocities.

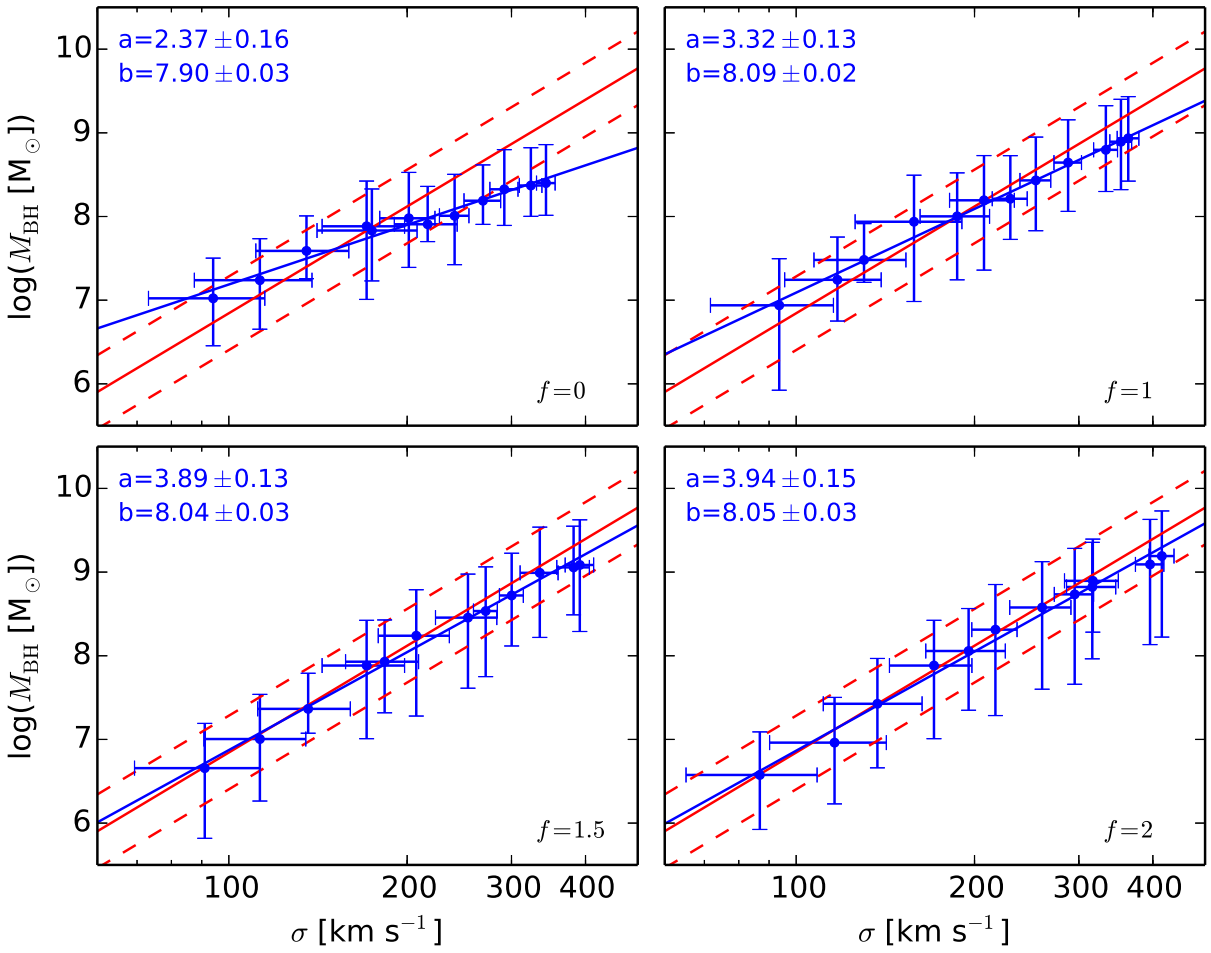

Figure 6.7.: M_{BH}-σ correlation for different values of the scaling f.

The slope a of the models with $f = 1.5$, $f = 2$ and $f = 3$ are all within the error range of the observed correlation, but the $f = 3$ model matches best, therefore we use this parameter for our standard sample.

The scaling of the AGN size has probably the most profound effect on the $M_{\rm BH}$-σ correlation and on the time lag as function of σ. Varying f not only changes the slope α, it even can change its sign. This in fact could reverse the results obtained in the previous section, in the sense that feedback is more relevant for high mass galaxies than for low mass galaxies.

Thus it is crucial for future investigations of the starburst-AGN timing to correctly describe the AGN size as a function of galaxy mass. Only the sizes of some AGN have been measured up to now (e.g., Downes and Solomon, 1998; Cattaneo et al., 2005), but a close relationship between AGN size and its host mass has yet to be discovered.

6.3. AGN size

After investigating the effect of the scaling of the AGN size in the previous section, we now vary the AGN size of our standard model, which affects, according to eq. 3.61, the AGN size of all other galaxies of the standard sample. Besides our standard model with $R_{\mathrm{AGN,std}} = 200\,\mathrm{pc}$ we investigate models with $R_{\mathrm{AGN,std}} = 100, 150, 250, 300\,\mathrm{pc}$.

Fig. 6.8 shows the time lag between starburst and AGN activity. Because $\tau_{\mathrm{visc}} \sim R_{\mathrm{AGN}}^{3/2}$, the time lag gets slightly larger with larger AGN sizes, but due to the large scatter of this relation it is futile to make any more precise statements. Fig. 6.9 shows the M_{BH}-σ correlations, whose parameters are tabulated in table 6.4. The slope a decreases with increasing AGN size, the explanation for this behavior follows the same argument as in section 6.1: High mass galaxies are hardly affected by a change in time lag and thus by a change in AGN size. But for low mass galaxies a smaller AGN size leads to a smaller time lag, thus more gas is removed by feedback and less mass is available for the BH. Unchanged BH masses for high mass galaxies and decreased masses for low mass galaxies thus lead to an increase of the slope a with decreasing AGN size.

$R_{\mathrm{AGN,std}}$ [pc]	a	b
100	4.81 ± 0.38	7.96 ± 0.08
150	4.46 ± 0.36	8.06 ± 0.08
200	4.31 ± 0.27	8.03 ± 0.06
250	4.00 ± 0.31	8.11 ± 0.07
300	4.03 ± 0.22	8.08 ± 0.05

Table 6.4.: Parameters of the M_{BH}-σ correlation for different AGN sizes.

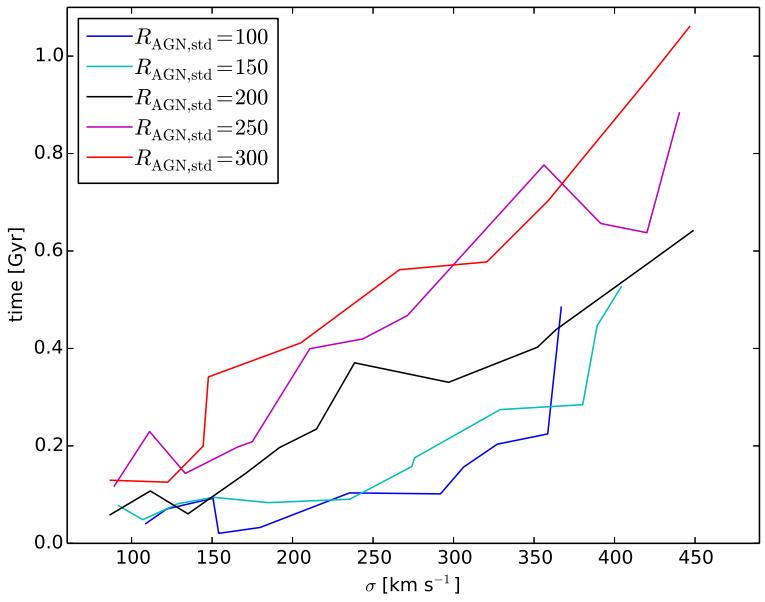

Figure 6.8.: Time lag between starburst and AGN activity for different AGN sizes.

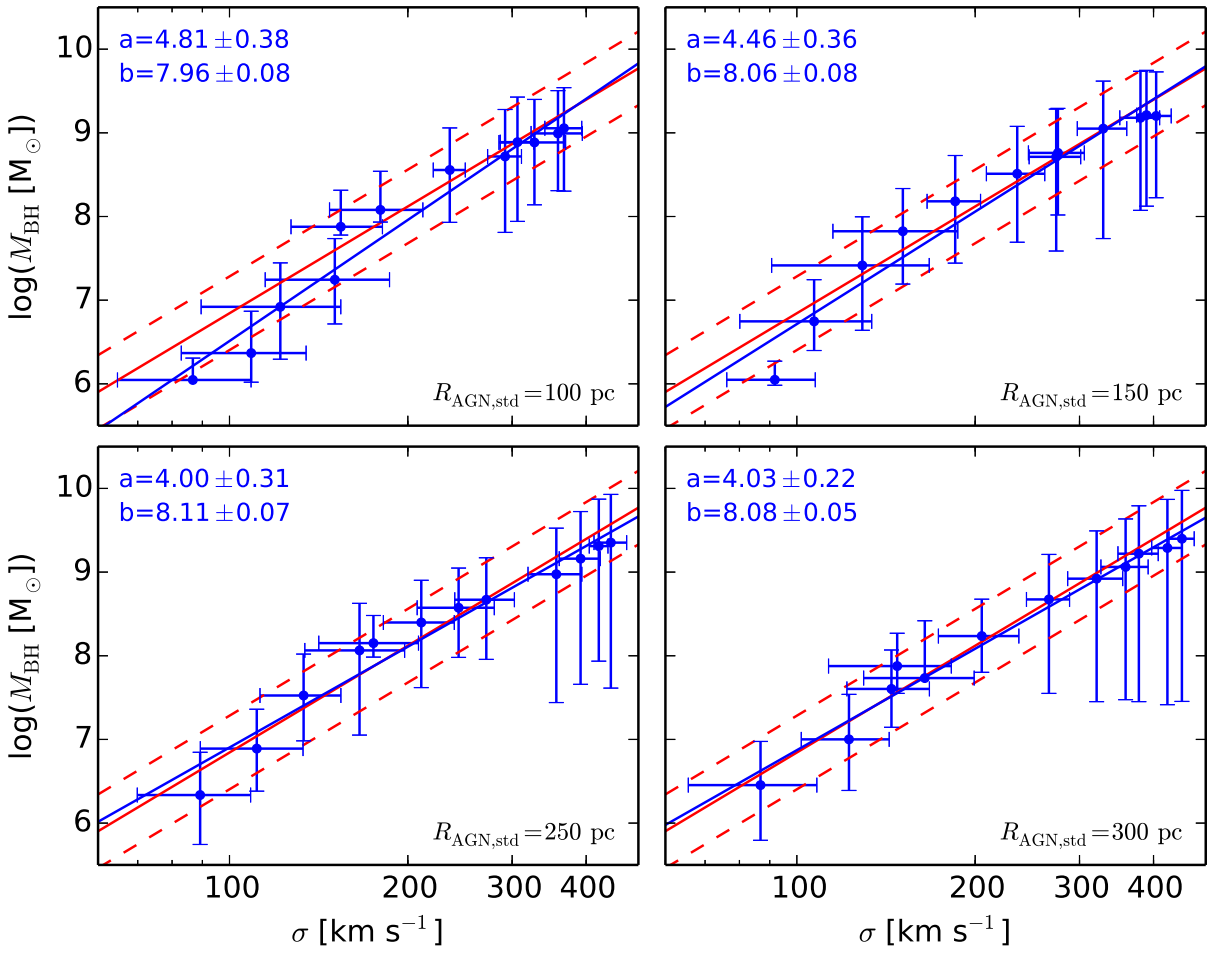

Figure 6.9.: M_{BH}-σ correlation for different values of $R_{\mathrm{AGN,std}}$.

6.4. β-parameter

The β-parameter determines the magnitude of the accretion disk's turbulent viscosity, according to Duschl et al. (2000) this parameter is of order 10^{-3} to 10^{-2}. In this section we investigate, besides our standard model with $\beta = 4 \cdot 10^{-3}$, the values $1 \cdot 10^{-3}$, $2 \cdot 10^{-3}$, $8 \cdot 10^{-3}$ and $10 \cdot 10^{-3}$.

Fig. 6.10 shows the time lag between starburst and AGN activity for different values of β. As expected from $\tau_{\mathrm{visc}} \sim 1/\beta$ the time lag increases with decreasing β. This change affects the M_{BH}-σ correlation, that is shown in Fig. 6.11 and tabulated in table 6.5.

Again low mass galaxies are most affected: large values of β lead to a smaller time lag and more mass is removed by the feedback. Thus less mass is available for the BH which steepens the M_{BH}-σ correlation.

Interestingly the change in the time lag, when varying β, is very large for high mass galaxies, but the final BH mass is not much affected by that. On the other hand low mass galaxies show only a small change in the time lag, but the change in BH mass is rather large.

β	a	b
$1 \cdot 10^{-3}$	3.94 ± 0.24	8.03 ± 0.06
$2 \cdot 10^{-3}$	4.02 ± 0.22	8.03 ± 0.05
$4 \cdot 10^{-3}$	4.31 ± 0.27	8.03 ± 0.06
$8 \cdot 10^{-3}$	4.85 ± 0.21	7.99 ± 0.04
$10 \cdot 10^{-3}$	5.04 ± 0.32	7.96 ± 0.06

Table 6.5.: Parameters of the M_{BH}-σ correlation for different values of β.

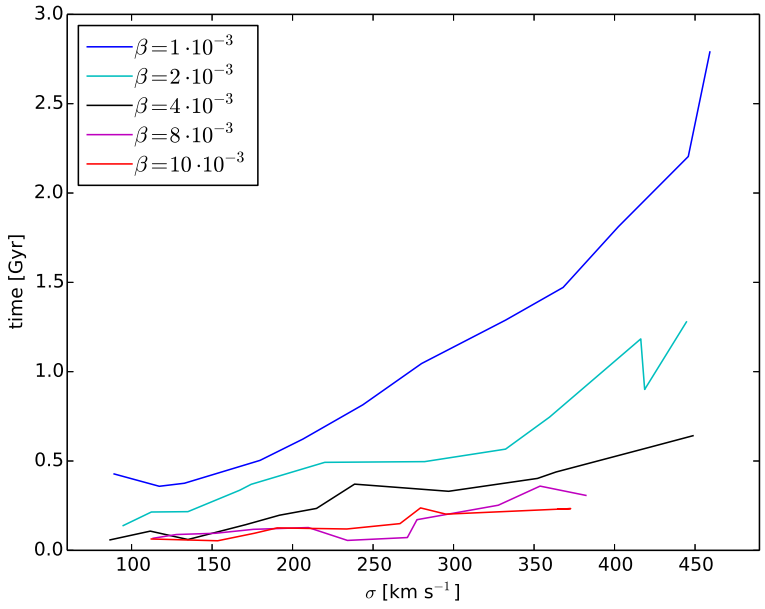

Figure 6.10.: Time lag between starburst and AGN activity for different values of β.

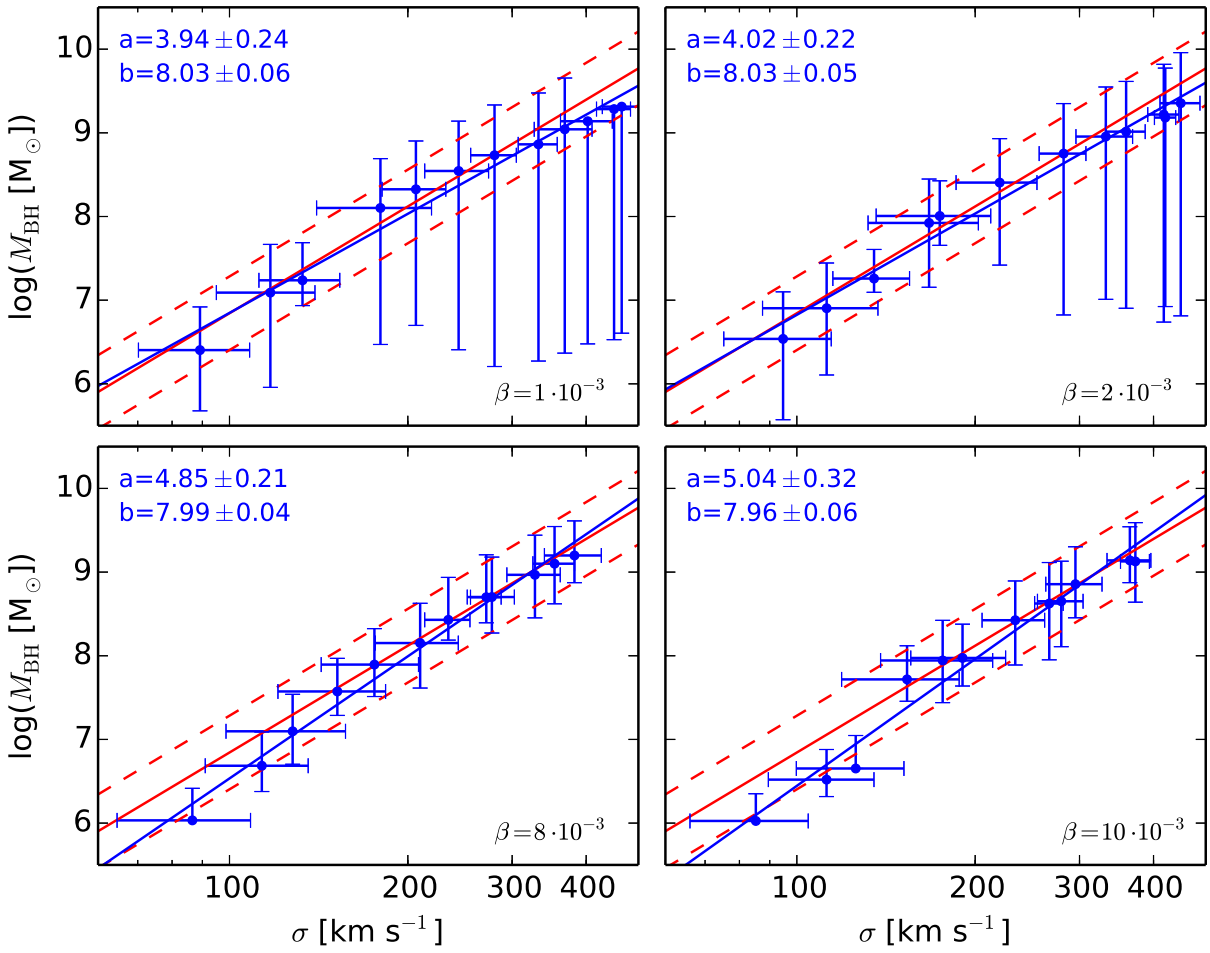

Figure 6.11.: M_{BH}-σ correlation for different values of β.

6.5. Gas content of the galaxies

Our standard model has a gas fraction of $f_{\rm gas} = 0.3$, in this chapter we investigate additional models with $f_{\rm gas} = 0.2, 0.4, 0.5, 0.6$. Fig. 6.12 shows the time lag between starburst and AGN activity, there is no clear trend when varying the gas fraction, mainly because of the large scatter of this relation that is induced by the erratic nature of galaxy evolution.

$f_{\rm gas}$	a	b
0.2	4.45 ± 0.24	7.86 ± 0.05
0.3	4.31 ± 0.27	8.03 ± 0.06
0.4	4.86 ± 0.44	8.01 ± 0.09
0.5	4.95 ± 0.48	8.06 ± 0.09
0.6	4.80 ± 0.60	8.08 ± 0.11

Table 6.6.: Parameters of the $M_{\rm BH}$-σ correlation for different gas fractions.

In general one would, on the one hand, expect a larger BHAR and BH mass with larger gas fraction, because there is more gas available for accretion. On the other hand, a larger BHAR would lead to stronger feedback, and a larger central mass would lead to the feedback setting in earlier ($\tau_{\rm visc} \sim M_{\rm AGN}^{-0.5}$), that would then remove more of the gas and lead to quenching of the BHAR.

Both effects can be seen in Figs. 6.13 and 6.14, where we plot the BHAR for different gas fractions for the $v_{\rm vir} = 120\,{\rm km\,s^{-1}}$ and the $v_{\rm vir} = 320\,{\rm km\,s^{-1}}$ galaxies, respectively. Fig. 6.14 shows that, before the merger event, the BHAR is larger for larger gas fractions, but after the merger event the situation is reversed (except for the BHARs of $f_{\rm gas} = 0.2$

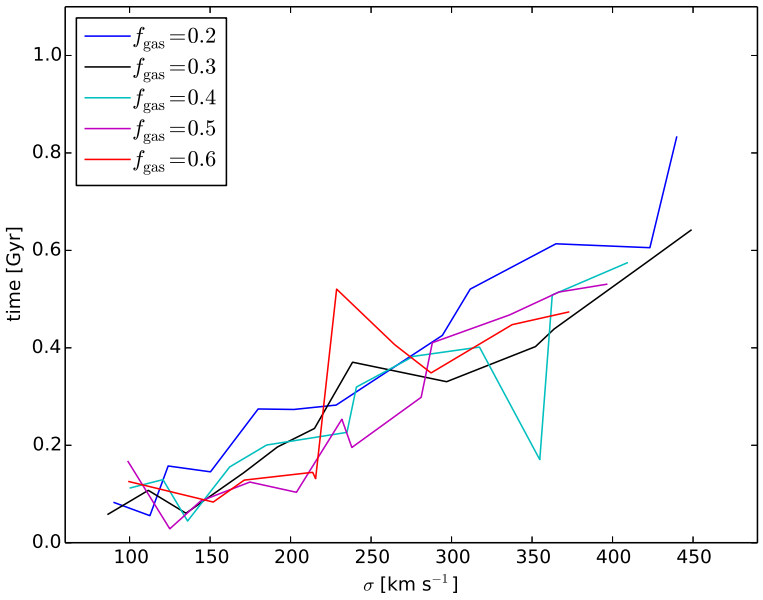

Figure 6.12.: Time lag between starburst and AGN activity for different gas fractions.

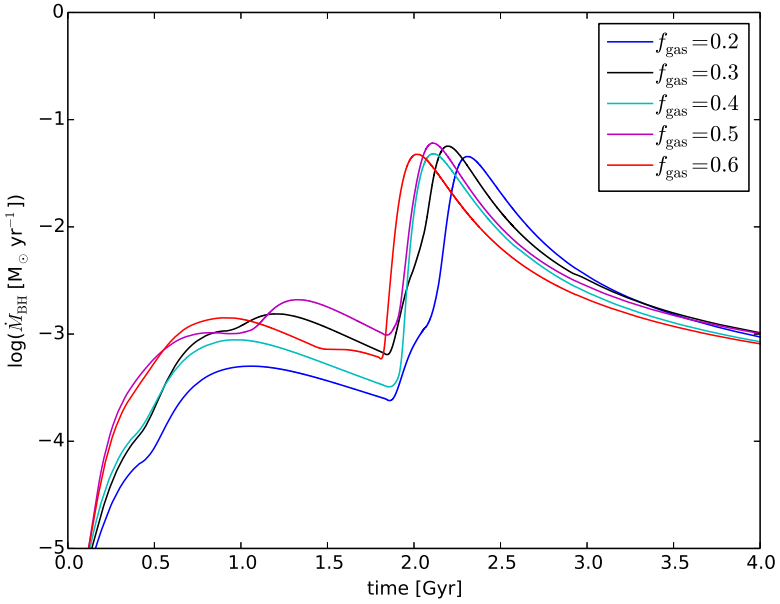

Figure 6.13.: Black hole accretion rate for galaxies with $v_{\rm vir} = 120\,{\rm km\,s^{-1}}$ for different gas fractions.

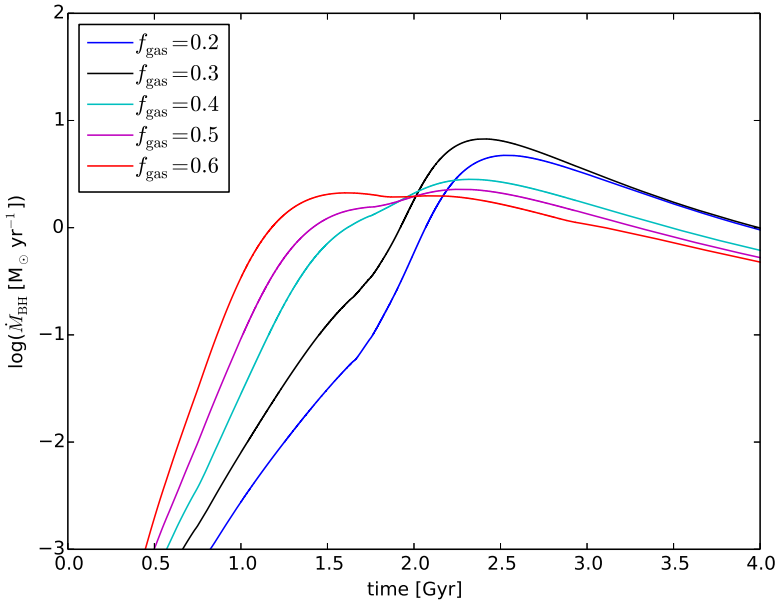

Figure 6.14.: Black hole accretion rate for galaxies with $v_{\rm vir} = 320\,{\rm km\,s^{-1}}$ for different gas fractions.

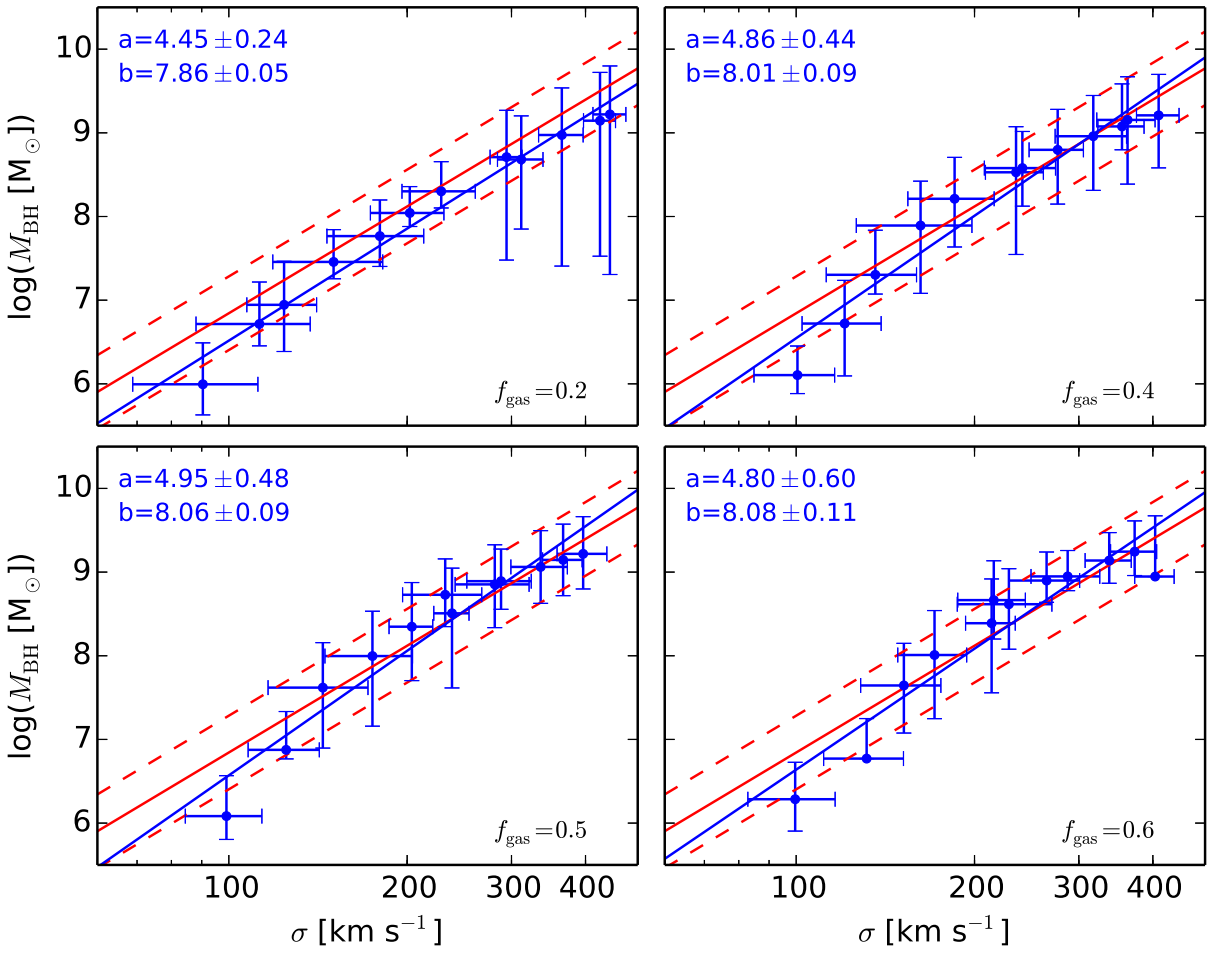

Figure 6.15.: $M_{\rm BH}$-σ correlation for different gas fractions.

and $f_{\rm gas} = 0.3$, but which are very close to one another).

In Fig. 6.13 this trend is not visible before the merger event, because of the erratic nature of galaxy evolution. But after the merger event the BHAR is again larger for smaller gas fractions as expected (except for the BHARs of $f_{\rm gas} = 0.4$ and $f_{\rm gas} = 0.5$, but which are again very close to one another). Furthermore Fig. 6.13 shows the BHARs peaking slightly later with smaller gas fraction.

However, this is not visible in the time lags of Fig. 6.12 because these small differences are washed out by the large scatter in the determination of the starburst timing. The $M_{\rm BH}$-σ correlation is shown in Fig. 6.15 and tabulated in table 6.6. The normalization b roughly rises with increasing gas fraction, thus higher gas fractions lead to more massive black holes, but the slope a does not follow a clear trend and only shows erratic changes.

6.6. Inclination

In our standard model the second galaxy has an inclination of $\theta = 30°$, in this section we explore angles of 0°, 60°, 90° and 180° (the last angle is similar to $\theta = 0°$, but with the second galaxy rotating in the opposite direction).

The $M_{\rm BH}$-σ correlation is shown in Fig. 6.16, and its parameters in table 6.7. Galactic planes being parallel to each other result in a larger normalization b, i.e., larger BH masses and a shallower slope a. For perpendicular galactic planes the BH masses are lower and the $M_{\rm BH}$-σ correlation is steeper.

Furthermore the uncertainties on σ are larger for merging galaxies with parallel galactic planes. Such merger events will lead to an elliptical galaxy that is itself rather flat and that has a high ellipticity. Thus the velocity dispersion σ will be different depending on along which axis it is measured. Nevertheless measuring σ by assuming spherical symmetry, as it is done by observers and therefore also by our algorithm (see appendix B), will result in a large error. The assumption of spherical symmetry is much more justified for merging galaxies with perpendicular galactic planes, thus in this case the error bars are smaller. The time lags shown in Fig. 6.17 show a large scatter and do not show any clear trend with varying inclination.

θ	a	b
0°	4.07 ± 0.33	8.19 ± 0.07
30°	4.31 ± 0.27	8.03 ± 0.06
60°	4.37 ± 0.35	8.06 ± 0.07
90°	4.81 ± 0.38	7.99 ± 0.08
180°	4.06 ± 0.37	8.21 ± 0.08

Table 6.7.: Parameters of the $M_{\rm BH}$-σ correlation for different values of the inclination θ.

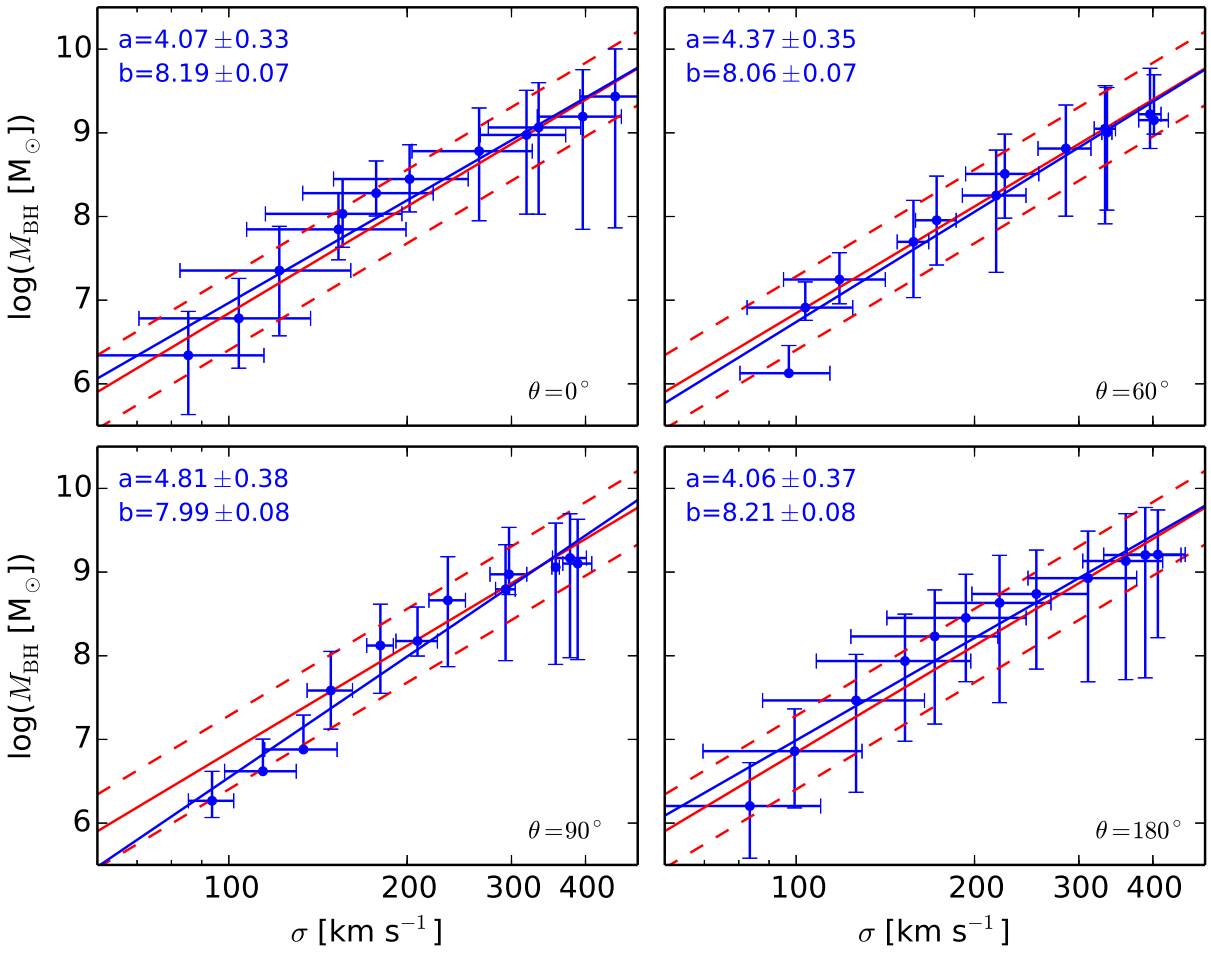

Figure 6.16.: M_{BH}-σ correlation for different inclinations.

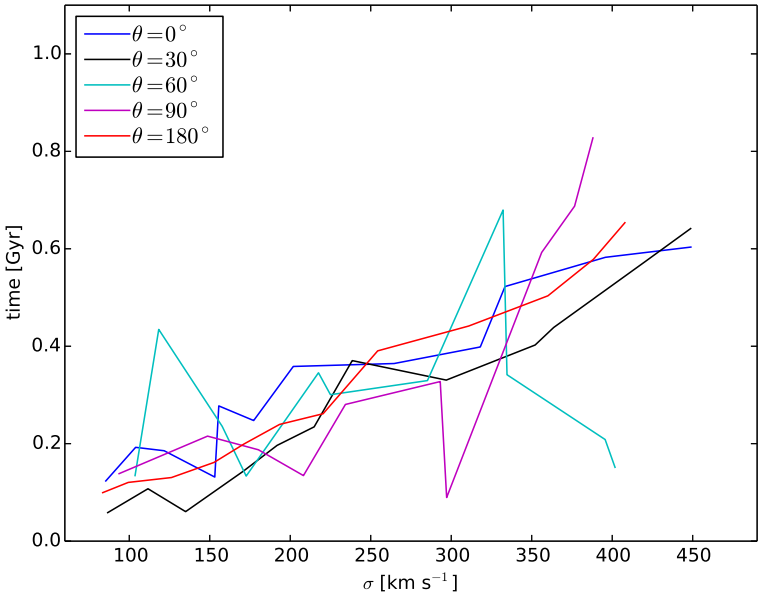

Figure 6.17.: Time lag between starburst and AGN activity for different inclinations θ.

6.7. The M_{BH}-σ correlation

Our standard model follows the observed $M_{\rm BH}$-σ correlation quite well, as we have shown in section 4.3. However, some of our parameter sets show significant deviations from the observed correlation. For example, small values of $R_{\rm AGN,std}$ overestimate the slope of the $M_{\rm BH}$-σ correlation, whereas large values of $R_{\rm AGN,std}$ slightly underestimate it. That does not necessarily mean that some these parameters are inherently wrong. Determining the $M_{\rm BH}$-σ correlation using the five samples with different $R_{\rm AGN,std}$ together gives a slope of $a = 4.32$ and a normalization of $b = 8.05$, fitting the observed correlation better than most of the single samples.

We even go one step further and calculate the $M_{\rm BH}$-σ correlation for all samples presented in this chapter, except the model without AGN feedback as this is a rather unrealistic scenario, used only for illustration purposes. This gives 24 samples with 12 merger simulations each, giving a total number of 288 mergers for the total $M_{\rm BH}$-σ correlation that we show in Fig. 6.18. The slope of this correlation is $a = 4.28$ and thus inside the observed error range, the normalization is slightly outside the observed error range with $b = 8.03$.

However, although our fit follows the observed correlation quite well, we cannot exclude the possibility that this is a result of mere chance. Our total sample is not representative of the galaxy population in our universe, because of the following reasons:

(I) Our parameter study only involved 6 parameters. We have chosen a set of parameters

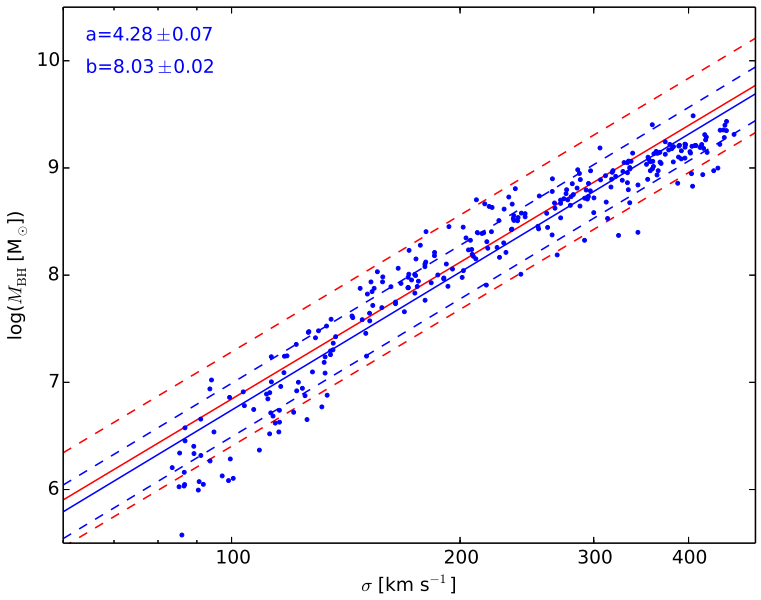

Figure 6.18.: M_{BH}-σ correlation with intrinsic scatter for all simulations presented in this chapter, except the simulations without AGN feedback.

where we expect the most significant changes to occur, but our galaxy model and our algorithms include other parameters that could influence the M_{BH}-σ correlation.

(II) Our chosen parameter ranges are, at least to some extent, arbitrary. For the feedback parameter τ_{w} we have chosen values between 1 and 7, and for $R_{\mathrm{AGN,std}}$ we used a range of 100-300 pc, but values outside this range cannot be ruled out. For the gas fraction f_{gas} we used values between 0.2 and 0.6, but there are galaxies with gas fractions outside this range. For example our Milky Way has a gas fraction of only ~ 0.15 (Yin et al., 2009).
On the other hand, the range for the viscosity parameter β is well known to be of 10^{-3} to 10^{-2} (Duschl et al., 2000). Likewise the scaling f of the AGN size is probably inside our chosen range of 0...3. A scaling of larger than 3 would result AGN larger than allowed by observations, while a scaling of smaller than 0 is rather unrealistic, implying that AGN become smaller with increasing galaxy mass. The virial velocities of our galaxies lying between 100 km s^{-1} and 320 km s^{-1} can also be motivated by observations as we explained in section 3.7.

(III) The distribution of parameters within their range is also rather arbitrary. For some parameters, like the feedback parameter τ, the AGN size $R_{\mathrm{AGN,std}}$ or the viscosity parameter β such a distribution is in general unknown. For other parameters, like the gas fraction f_{gas} or the virial velocity, such distributions could be obtained easily from observations. To investigate the effect of galaxy orientation we only varied the inclination θ. More generally, the orientation of one galaxy, i.e., the orientation of

its axis, can be described by two parameters, giving four parameters for one merger simulation. As galaxies are randomly oriented in the universe these parameters are uniformly distributed within their ranges.

As some of the relevant ranges or distributions are at present generally unknown, it is currently not possible to fully comprehend the M_{BH}-σ correlation by simulations. Thus even if a sample (e.g., the $f_{\mathrm{gas}} = 0.5$ sample) does not follow the observed correlation, it does not necessarily indicate that the galaxy model or the algorithms used are inherently wrong, but that a non representative set of parameters may have been chosen. On the other hand, success in reproducing the observed correlation is not a good indicator of the accuracy of the models and algorithms used, although it is often used in the literature (e.g., Di Matteo et al., 2005; Johansson et al., 2009; Debuhr et al., 2011). Our parameters chosen in chapter 3 match the observed correlation as shown in section 4.3, but these should only be interpreted as an 'average', rather than a representative set of parameters.

However, simulated M_{BH}-σ correlations that diverge from the observed correlations very strongly could be used to rule out the corresponding parameter sets. This is, e.g., the case for our simulations without AGN feedback. Samples with a low value for the scaling f also diverge strongly from the observed correlation, which is why we have chosen a value of $f = 3$ for our standard sample.

The 1-σ scatter of the observed M_{BH}-σ correlation is 0.44 dex and shown as red dashed lines in Fig. 6.18. We also show the 1-σ scatter of our simulated correlation as blue dashed lines, but this one is only 0.25 dex. For calculating this scatter we only used the values plotted in Fig. 6.18 and did not consider the continuing growth of the black hole. This indicates that the continuing growth of the black hole indeed contributes significantly to the large observed scatter of the M_{BH}-σ correlation, as we have argued in section 4.3. But as our total sample is not representative of the galaxy population in our universe, using different parameter ranges or distributions or varying more parameters could increase the scatter without invoking the continuing growth of the black hole.

6.8. Discussion

We have explored the effect of varying several parameters on the timing of the starburst-AGN connection and on the M_{BH}-σ correlation. In our standard sample the time lag increases with increasing galaxy mass, therefore low mass galaxies are generally affected more by AGN feedback than high mass galaxies. Thus when varying parameters the largest changes occur for low mass galaxies. Furthermore a smaller time lag leads to earlier feedback, thus more mass is removed from the galaxy and less mass is left for the BH. Conversely, a larger time lag leads to larger BH masses.

The scaling of the AGN size probably has the greatest influence on the time lag and on the M_{BH}-σ correlation as we discussed in section 6.2. In our standard sample the time lag increases with increasing galaxy mass, but varying the scaling can lead to a

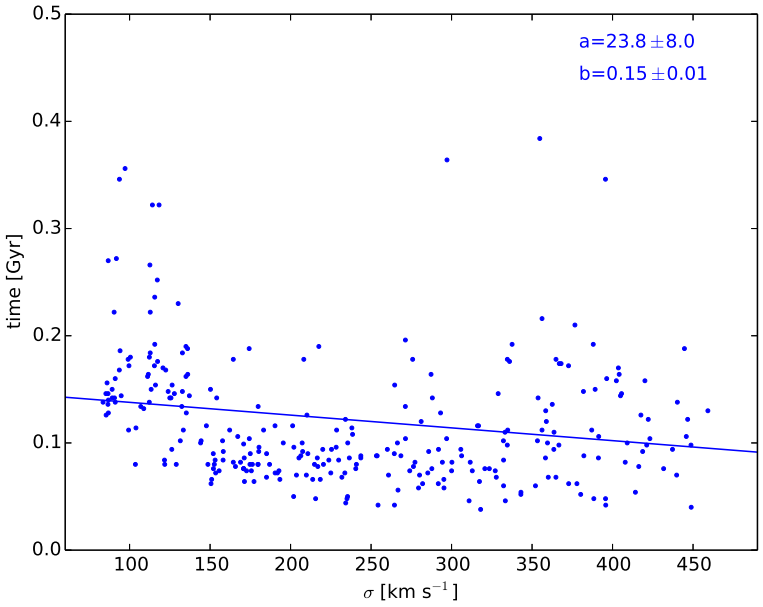

Figure 6.19.: Duration of the starburst for all simulations presented in this chapter, except the simulations without AGN feedback. The solid line is a fit to the function $t\,[\mathrm{Gyr}] = b - a \cdot 10^{-3} \cdot (\sigma \,/\, 200\,\mathrm{km\,s^{-1}})$.

constant or even to a declining time lag with increasing galaxy mass. This could actually reverse some of the findings presented in this chapter. When the time lag decreases with increasing galaxy mass high mass galaxies are more affected by feedback than low mass galaxies, thus varying parameters would mostly affect high mass galaxies. For example, setting $f = 0$ and increasing the parameter β as discussed in section 6.4 would then lead to smaller BH masses for high mass galaxies. Thus the slope a of the M_{BH}-σ correlation would show a decline instead of an increase as shown in section 6.4.

The observations give a time lag of about 200-300 Myr which corresponds to the time lag of our standard model, but when varying our model parameters the resulting time lags range from zero to almost 3 Gyr. When comparing our simulations to the observed time lags we have to consider that the observations measure the average time lag of a sample of galaxies without differentiating between galaxy properties like, e.g., galaxy mass or gas fraction. There are also some observational constraints, e.g., Wild et al. (2010) can only measure time lags that are smaller than 600 Myr. Thus the observed time lag can be regarded as an 'average' time lag of all the galaxies involved. When calculating the average time lag of the simulations presented in this chapter, but neglecting the model without AGN feedback and time lags that are larger than 600 Myr, we get a value of 234 Myr that corresponds to the observed time lag. However, the standard deviation is 149 Myr and thus rather large. As already pointed out in the last section, our results might change when selecting a sample of galaxies that is representative of the galaxy population in our universe.

In section 4.4 we measured the duration of the starburst as function of σ. Varying the parameters presented in this chapter does not change this relation whatsoever, but always gives a roughly constant duration of order of 100 Myr with a very slight increase towards lower values of σ. Therefore we show the starburst duration for all models presented in this chapter (again except the model without AGN feedback) in Fig. 6.19 together with a linear fit to the data. As the slope of the fit is very low and the scatter of this relation rather large, it is reasonable to assume that the starburst duration is a constant value and thus independent of σ. Calculating the mean value and the standard deviation of all values gives a starburst duration of 121 ± 73 Myr.

7. Conclusions of part I

In part I of this thesis we have investigated starbursts and AGN activity in galaxy mergers. We focused on time lags between these phenomena which have been observed recently, but where no satisfactory explanation has been provided so far. In our scenario the merger event drives huge amounts of gas towards the center of the newly forming galaxy due to tidal forces. The gas then forms an accretion disk and is accreted towards the central black hole. Thus the observed time lag is a viscous time lag the gas, after having formed stars, additionally needs to move to the central black hole. We developed a model that accounts for the gas forming an accretion disk and for the subsequent time evolution of this disk.

In chapter 4 we investigated the general properties and the outcome our model setup, we were able to reproduce three observational findings that are known to occur in galaxies:

(I) AGN activity is delayed with respect to the starburst by a time span of about 200 Myr in agreement with observations. This time lag is, in our scenario, principally caused by a viscous time lag the gas needs to flow through the accretion disk until it reaches the central black hole.

(II) Our results are in agreement with the observed M_{BH}-σ correlation. As already pointed out by Di Matteo et al. (2005), AGN feedback is responsible for establishing this relation.

(III) The continuing growth of the black hole after the merger event may contribute to the large observed scatter in the M_{BH}-σ correlation.

However, with our parameter study in chapter 6 we have shown that some parameter sets do not fulfill the M_{BH}-σ correlation. We have argued that such subsets are not representative for a typical galaxy population, and that a representative set of parameters has to be chosen to correctly reproduce the M_{BH}-σ correlation. As some of the parameter ranges and distributions involved are generally unknown it is currently not possible to fully comprehend the M_{BH}-σ correlation by means of simulations. Thus reproducing the M_{BH}-σ correlation is in general a bad test for the models and algorithms used. The large observed scatter of the M_{BH}-σ correlation can be partly explained by the large number of galaxy properties that influence this correlation. Galaxies are individuals that cannot be forced into a tight correlation that only depends on two parameters. The M_{BH}-σ correlation is rather influenced by a large number of galaxy properties. However, this effect only accounts for approx. half of the observed scatter, thus to explain the full

observed scatter it is necessary to involve the aforementioned continuing growth of the black hole.

The time lag of our standard model matches the observed time lag between starburst and AGN activity. Our parameter study gives a whole range of time lags with an average value of 234 ± 149 Myr that also matches the observed time lag, but with a large uncertainty. For future studies regarding time lags between starburst and AGN activity further observations, like measuring the time lag as function of the stellar velocity dispersion, are necessary to obtain a deeper insight into the timing of the starburst-AGN connection. It is also necessary to constrain some of the parameters that we used in our simulations; the most important one is the AGN size as a function of galaxy mass.

Part II.

The Galactic Center

8. Introduction to part II

8.1. Overview

When studying galactic nuclei, i.e., the physical processes that are prevalent in the centers of galaxies, it is a plausible idea to study the one that is closest to us: the center of our own Milky Way. The nearest larger galaxy[1], the Andromeda galaxy, has a distance of about 800 kpc, whereas the distance of the Milky Way's center from our solar system is only about 8 kpc, so it is 100 times closer than the Andromeda galaxy. This provides the unique opportunity to study physical processes in galactic centers in great detail. In this chapter we will first describe the properties of the Galactic Center and then present our research plans in that regard.

8.2. Properties of the Galactic Center

The center of our Milky Way hosts a black hole with a mass of about $4 \cdot 10^6\,\mathrm{M}_\odot$ (Ghez et al., 2008; Gillessen et al., 2009; Yelda et al., 2014) and is surrounded by a gaseous disk, the so-called circumnuclear disk (CND).

The properties of the CND have been investigated in a large number of studies (e.g., Becklin et al., 1982; Genzel et al., 1985; Guesten et al., 1987; Sutton et al., 1990; Zylka et al., 1995; Morris et al., 1999) with the following results: the CND has densities of $\sim 10^5\,\mathrm{cm}^{-3}$, a mass of a few $10^4\,\mathrm{M}_\odot$, temperatures of a few 100 K and an outer radius of about 4 pc. The disk's inner rim does not extend inwards as far as the black hole[2], the CND rather has an inner cavity with a radius of ∼1 pc. The CND consists of a clumpy medium, the clumps have sizes of 0.1-0.2 pc and densities of about $10^{5\ldots6}\,\mathrm{cm}^{-3}$ (Genzel, 1989; Mezger et al., 1989; Marr et al., 1993; Martín et al., 2012; Lau et al., 2013).

However, the critical Roche density at 2 pc is $\sim 10^7\,\mathrm{cm}^{-3}$ (Guesten et al., 1987), thus the clumps are not stable against tidal shearing and get destroyed within a dynamical time. Montero-Castaño et al. (2009) and Requena-Torres et al. (2012) argue that the

[1] There is a number of galaxies that are closer than the Andromeda galaxy, but which are classified as dwarf galaxies and where a galactic nucleus, in the sense of a central black hole surrounded by an accretion disk, has not been observed so far.

[2] Accretion disks around black holes usually extend to much smaller scales, namely to the so-called last stable orbit, which is, e.g., three Schwarzschild radii for non-rotating black holes.

presence of unstable clumps indicates that the disk must have been created very recently, and hence the CND is not a permanent feature, but a transient one. There are other studies that measure clump densities of $3\text{-}4 \cdot 10^7\,\mathrm{cm}^{-3}$ and therefore conclude that the CND is a non-transient phenomenon with a lifetime of $\sim 10^7$ years (Christopher et al., 2005; Martín et al., 2012). It is currently highly debated whether the CND is a transient or a permanent phenomenon. The CND furthermore has a magnetic field with a field strength of about 1 mG and a toroidal configuration (Werner et al., 1988; Hildebrand et al., 1993; Plante et al., 1995; Bradford et al., 2005).

The CND's inner cavity hosts a stellar cluster that consists mostly of Wolf-Rayet stars (Najarro et al., 1997). This type of stars is characterized by strong stellar winds that have outflow rates of $\sim 10^{-5\cdots-4}\,\mathrm{M}_\odot\,\mathrm{yr}^{-1}$ and velocities of the order of $1000\,\mathrm{km\,s}^{-1}$ (Crowther, 2007). The sum of the winds from the individual stars produces a total outflow from the central cluster that is roughly spherically symmetric with an outflow velocity of $700\,\mathrm{km\,s}^{-1}$ and a mass outflow rate of $5 \cdot 10^{-3}\,\mathrm{M}_\odot\,\mathrm{yr}^{-1}$ (Geballe et al., 1987). It is generally assumed that the stellar cluster's outflow suppresses the inflow of gas from the disk and hence that the inner cavity of the CND is maintained by the interaction of the outflow with the disk's inner rim (e.g., Genzel et al., 2010). In Fig. 8.1 we show a schematic depiction of the Galactic Center.

Thus the Galactic Center is currently in a quiescent state, where no significant black hole accretion or star formation is taking place. However, there is evidence that in the relatively recent past the situation was quite different: Chen and Amaro-Seoane (2014) argue that the central black hole was powered by an accretion disk several million years ago. The disk was more massive and reaching as far as the black hole, the disk was furthermore subject to star formation. According to Lu et al. (2013) the stars of the central stellar cluster were formed during a single starburst that happened about $4 \cdot 10^6$ years ago.

Morris et al. (1999) propose a cyclic activity in the sense of a starburst-AGN connection on small scales, where the Galactic Center is alternating between starbursts and AGN activity: The Galactic Center is currently in a quiescent state, because the winds from the central stellar cluster prevent the disk's gas from being accreted. But due to the evolution of the cluster stars these winds will subside after some time and thus the gas from the disk will start to migrate inwards, causing the accretion rate of the black hole to rise. The continuing accretion of gas by the black hole causes a high luminosity of the accretion disk. This burst of radiation compresses the inner disk gas and thus triggers star formation and the formation of a new central stellar cluster. Stellar winds will clear the central region of gas and will thus quench further black hole accretion and star formation, bringing the Galactic Center in the same state than observed today. The period of this cycle is determined by the lifetime of the cluster stars of approx. 10^7 years.

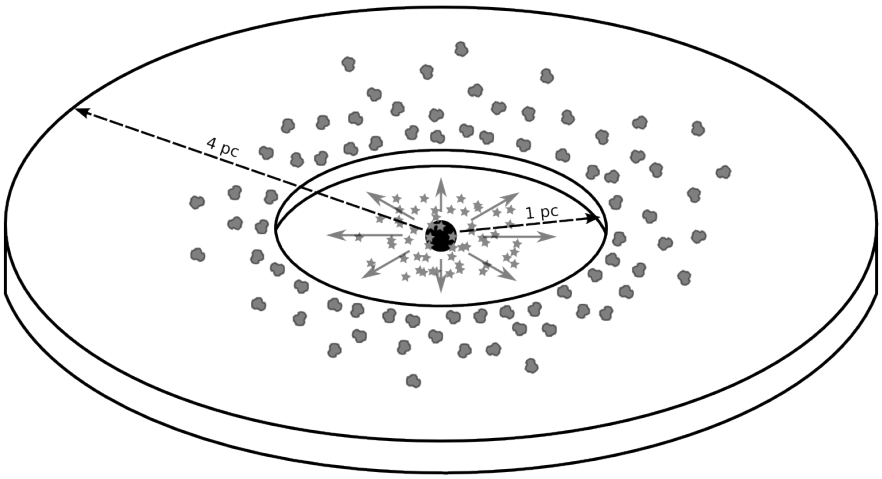

Figure 8.1.: The circumnuclear disk in the center of the Milky Way consists of a clumpy medium, it has an outer radius of 4 pc and an inner cavity with a radius of 1 pc. The cavity hosts a black hole and a stellar cluster, the latter launches a strong, spherical wind.

8.3. Outline of part II

In part II of this thesis we will question two paradigms that are prevalent in previous research on the Galactic Center. The first is that the inner cavity of the disk is maintained by the interaction of the central stellar cluster's strong winds with the inner rim of the disk, thus explaining the currently quiescent state of the Galactic Center. The second is that the clumpiness of the disk implies that the CND is a transient feature.

We will conduct this research by means of magnetohydrodynamical (MHD) simulations by using the three-dimensional simulation code AstroBEAR. Our model consists of the central black hole, the outflow from the central stellar cluster and the CND including the effects of magnetic fields. We describe our numerical methods in the next chapter.

Our results presented in chapter 10 reveal that the interaction of the central stellar cluster's outflow with the disk's inner rim actually leads to a collapse of the inner cavity, contrary to previous expectations. However, including the effects of magnetic fields stabilizes the inner cavity against collapse. We will furthermore show that this interaction causes hydrodynamical instabilities at the inner rim that lead to the formation of unstable clumps. Thus the occurrence of unstable clumps is not an indicator for a transient nature of the CND.

9. Computational methods

Accretion disks are usually described by the Navier-Stokes equations, since magnetic fields play an important role in the CND we will extend this approach by using magnetohydrodynamical methods. In the first section of this chapter we will introduce the equations of ideal MHD, followed by a brief introduction to the numerical techniques for solving these equations. We will then discuss further numerical techniques like AMR, cooling, the modeling of the outflow from the central stellar cluster and the initial conditions for our simulations.

9.1. Equations of ideal MHD

The equations of MHD are a combination of the Navier-Stokes equations and Maxwell's equations. Here we assume ideal MHD, where the resistivity of the plasma is zero, equivalent to infinite conductivity. Thus the magnetic field lines are frozen into the plasma, and field lines always follow plasma motions or vice versa. The CND consists mostly of molecular hydrogen, thus the ionization degree is very low. However, even a low ionization degree is sufficient to couple the gas to the magnetic field and thus justifies the use of ideal MHD.

The set of ideal MHD equations consist of the continuity equation

$$\frac{\partial \rho}{\partial t} + \nabla \cdot (\rho \mathbf{v}) = 0 \tag{9.1}$$

with the mass density ρ and the velocity $\mathbf{v}$; the momentum equation

$$\frac{\partial \rho \mathbf{v}}{\partial t} + \nabla \cdot (\rho \mathbf{v}\mathbf{v} - \mathbf{B}\mathbf{B}) + \nabla \left(P + \frac{\mathbf{B}^2}{2} \right) = 0 \tag{9.2}$$

with magnetic field $\mathbf{B}$ and gas pressure P; the energy equation

$$\frac{\partial \varepsilon}{\partial t} + \nabla \cdot \left[\left(\varepsilon + P + \frac{\mathbf{B}^2}{2} \right) \mathbf{v} - \mathbf{B} \left(\mathbf{B}\mathbf{v} \right) \right] = 0 \tag{9.3}$$

with the total energy density ε; and Faraday's law

$$\frac{\partial \mathbf{B}}{\partial t} + \nabla \times \mathbf{E} = 0 \tag{9.4}$$

with the electric field **E**. From Faraday's law, it follows that initially solenoidal magnetic fields remain solenoidal at all times. This set of equation is closed with Ohm's law for a perfectly conducting medium

$$\mathbf{E} = -\mathbf{v} \times \mathbf{B} \tag{9.5}$$

and the polytropic equation of state for an ideal gas

$$P = (\gamma - 1) \cdot \left(\varepsilon - \rho \frac{\mathbf{v}^2}{2} - \frac{\mathbf{B}^2}{2} \right) . \tag{9.6}$$

Gauss's law can be dropped as we assume that the plasma is electrically neutral. We use Gaussian units in a modified form, such that the factor 4π does not appear in our equations.

Solving the ideal MHD equations

To solve the equations of ideal MHD we use the adaptive-mesh-refinement MHD code AstroBEAR 3.0 that was developed by Cunningham et al. (2009) and Carroll-Nellenback et al. (2013). This high-resolution shock-capturing grid code solves conservation laws of the form

$$\frac{\partial}{\partial t}\mathbf{Q} + \frac{\partial}{\partial x}\mathbf{F}_x(\mathbf{Q}) + \frac{\partial}{\partial y}\mathbf{F}_y(\mathbf{Q}) + \frac{\partial}{\partial z}\mathbf{F}_z(\mathbf{Q}) = \mathbf{S} \, . \tag{9.7}$$

Bringing the above equations into this form gives

$$\begin{aligned}
&\frac{\partial}{\partial t}\begin{bmatrix} \rho \\ \rho v_x \\ \rho v_y \\ \rho v_z \\ \varepsilon \\ B_x \\ B_y \\ B_z \end{bmatrix} + \frac{\partial}{\partial x}\begin{bmatrix} \rho v_x \\ \rho v_x^2 + P + \mathbf{B}^2/2 - B_x^2 \\ \rho v_y v_x - B_x B_y \\ \rho v_z v_x - B_x B_z \\ (\varepsilon + P + \mathbf{B}^2/2) v_x - B_x(\mathbf{B}\cdot\mathbf{v}) \\ 0 \\ -E_z \\ E_y \end{bmatrix} \\
&+ \frac{\partial}{\partial y}\begin{bmatrix} \rho v_y \\ \rho v_x v_y - B_y B_x \\ \rho v_y^2 + P + \mathbf{B}^2/2 - B_y^2 \\ \rho v_z v_y - B_y B_z \\ (\varepsilon + P + \mathbf{B}^2/2) v_y - B_y(\mathbf{B}\cdot\mathbf{v}) \\ E_z \\ 0 \\ -E_x \end{bmatrix} + \frac{\partial}{\partial z}\begin{bmatrix} \rho v_z \\ \rho v_x v_y - B_z B_x \\ \rho v_y v_z - B_z B_y \\ \rho v_z^2 + P + \mathbf{B}^2/2 - B_z^2 \\ (\varepsilon + P + \mathbf{B}^2/2) v_z - B_z(\mathbf{B}\cdot\mathbf{v}) \\ -E_y \\ E_x \\ 0 \end{bmatrix} = \mathbf{S}
\end{aligned} \tag{9.8}$$

where **S** denotes source terms, in our scenario the gravitational force from the central black hole and the cooling of the gas.

The three-dimensional computational domain is divided into cubical cells, each denoted with the indices (i, j, k). Thus at each time step n the conservative variables in each cell have the values $\mathbf{Q}^n_{i,j,k}$. Based on this state AstroBEAR uses the finite-volume method to integrate the conservation laws. Thus by using the state $\mathbf{Q}^n_{i,j,k}$ at time step n, the conservative variables at time step $n+1$ are calculated as

$$\begin{aligned}\mathbf{Q}^{n+1}_{i,j,k} = \mathbf{Q}^n_{i,j,k} &- \frac{\Delta t}{\Delta x}\left(\tilde{\mathbf{F}}^n_{x,i+\frac{1}{2},j,k} - \tilde{\mathbf{F}}^n_{x,i-\frac{1}{2},j,k}\right) \\ &- \frac{\Delta t}{\Delta y}\left(\tilde{\mathbf{F}}^n_{y,i,j+\frac{1}{2},k} - \tilde{\mathbf{F}}^n_{y,i,j-\frac{1}{2},k}\right) \\ &- \frac{\Delta t}{\Delta z}\left(\tilde{\mathbf{F}}^n_{z,i,j,k+\frac{1}{2}} - \tilde{\mathbf{F}}^n_{z,i,j,k-\frac{1}{2}}\right) .\end{aligned} \tag{9.9}$$

$\tilde{\mathbf{F}}_x$, $\tilde{\mathbf{F}}_y$ and $\tilde{\mathbf{F}}_z$ are the respective fluxes across the cell edges. The simplest possibility for calculating those fluxes is the Euler method, where, e.g.,

$$\tilde{\mathbf{F}}^n_{x,i+\frac{1}{2},j,k} = \mathbf{F}_x\left(\mathbf{Q}^n_{i+\frac{1}{2},j,k}\right) \tag{9.10}$$

by using the flux function defined in eq. 9.8 and by using the conservative variables at time step n and at the location $(i+\frac{1}{2}, j, k)$. The conservative variables at the cell interface $i+\frac{1}{2}$ are calculated by an interpolation of the values $\mathbf{Q}^n_{i,j,k}$ and $\mathbf{Q}^n_{i+1,j,k}$. Thus the fluxes across the cell edges are only functions of the known variables $\mathbf{Q}^n_{i,j,k}$. However, AstroBEAR uses more advanced time integration methods than the Euler method, temporally averaged fluxes from time step n to time step $n+1$ are used by applying a second-order time integration scheme.

The correctness of this code has been demonstrated by comparison with analytical solutions of standard MHD test problems and with numerical solutions of various other codes. For a more detailed description of the numerical methods we refer to Cunningham et al. (2009) and Carroll-Nellenback et al. (2013). AstroBEAR is furthermore fully parallelized and good performance has been proven for the usage of up to 12228 cores.

9.2. Additional numerical techniques

As the mass of the Milky Way's central black hole exceeds the mass of the disk by about two orders of magnitude we do not consider the gravitational force of the disk. Furthermore we have not implemented any physical viscosity. Our simulations span about 13 orbital timescales, which is very short compared to the viscous timescale (which is about 100-1000 orbital timescales, Duschl et al., 2000). Thus we do not expect viscous processes to play a crucial role in our scenario. We also do not account for accretion, i.e., for mass growth of the black hole, because the numerical setup of the outflow from the central stellar cluster (see below) prohibits any kind of mass inflow towards the black hole. The last two points are justified insofar as observations of the CND do not show significant accretion of material onto the black hole.

Adaptive mesh refinement

AstroBEAR uses the numerical technique of adaptive mesh refinement (AMR) that increases (decreases) the resolution in regions that have a large (low) discretization error. A cell (i, j, k) is marked for refinement if the gradient of a representative quantity is too large, thus if the condition

$$\left| \log \left(\left| \frac{Q_{i+\frac{1}{2},j,k}}{Q_{i-\frac{1}{2},j,k}} \right| \right) \right| > q_{\mathrm{tol}} \,, \tag{9.11}$$

or a similar condition that invokes the gradients along the j- or k-direction, is fulfilled for any component Q of the tuple $\mathbf{Q}$. q_{tol} is a tolerance parameter that has usually values between 0.1 and 1. A refined cell is divided into eight cells, each having half the side length of its parent cell. A grid with basic resolution is referred to as level 0, a grid with double the basic resolution as level 1, and so on. In addition to condition 9.11 geometric regions can be specified that are set to a desired level of resolution.

Cooling

The CND is almost entirely molecular, consisting predominantly of H_2 (Harris et al., 1985). Therefore we use the cooling function developed by Lepp and Shull (1983), who calculated radiative cooling of H_2 using four vibrational lines, each with 21 rotational states. The cooling rate was fitted to an analytical function that gives the cooling rate as a function of the temperature and density of the gas. Using this approach we obtain disk temperatures of a few hundred Kelvin in accordance with observations, as we will show in section 10.1.

Outflow

To model the outflow from the central stellar cluster we define a spherical region around the black hole with a radius of 0.5 pc. In every time step of the code we set the hydrodynamic variables inside this region to specific values, namely to a density of $100\,\mathrm{cm}^{-3}$, a temperature of $10^6\,\mathrm{K}$ and a velocity of 700 km/s pointing radially outwards. These parameters give a global outflow rate of $5.5 \cdot 10^{-3}\,\mathrm{M}_\odot\,\mathrm{yr}^{-1}$ through the outer surface of this region. We emphasize that due to this numerical setup no material can enter the inner 0.5 pc.

9.3. Initial conditions and parameters

The computational domain has the dimensions $20\times20\times10\,\mathrm{pc}^3$ and consists initially of $32\times32\times16$ cells, corresponding to a spatial resolution of 0.625 pc. We allow up to 5

levels of refinement, corresponding to a maximum resolution of about 0.02 pc. The central black hole has a mass of $4.2 \cdot 10^6\,\mathrm{M}_\odot$.

The disk initially has an outer radius of 4 pc, an inner cavity with a radius of 1 pc, a thickness of 0.2 pc and a uniform density of $2{\cdot}10^5\,\mathrm{cm}^{-3}$, which gives a mass of $4.5{\cdot}10^4\,\mathrm{M}_\odot$. The initial temperature is 300 K throughout the disk. The disk is embedded in an ambient medium with a density of $1\,\mathrm{cm}^{-3}$ and a temperature of 10^6 K. The initial magnetic field is constrained to be present only within the disk, and to have a toroidal geometry and a uniform field strength of 1 mG. However, in section 10.2 we will test the effects of an initially vertical magnetic field.

At the location of the disk we always demand a resolution of at least level 4 (0.04 pc). To properly resolve the outflow we use the maximum resolution within a radius of 0.7 pc around the black hole. Because the CND consists predominantly of H_2, we use the equation of state of an ideal diatomic gas with $\gamma = 1.4$.

10. Results

In section 10.1 we will first elaborate on the general structure and the thermal properties of the CND, without considering magnetic fields, the central outflow or the inner cavity. Subsequently we will first investigate the influence of magnetic fields (but without central outflow) in section 10.2 and then the effects of the central outflow (but without magnetic fields) on the disk in section 10.3. In Section 10.4 we examine how numerical viscosity affects our results. Section 10.5 finally shows the full simulation, i.e., a simulation that includes magnetic fields, the inner cavity and the central outflow. In section 10.6 we will elaborate on the formation of clumps in the CND. All simulations presented in this chapter have a duration of 13 τ_{orb}, where $\tau_{\mathrm{orb}} = 4.5 \cdot 10^4\,\mathrm{yr}$ is the orbital timescale at 1 pc.

10.1. Thermal properties of the CND

Here we investigate the general structure and the thermal properties of the CND, the simulations presented in this section do not include magnetic fields, the central outflow or the inner cavity. Fig. 10.1 compares a simulation without cooling with a simulation where cooling is enabled. The top panel shows the 3D density structure of the CND and the middle panel shows vertical cross sections of the density. Cooling decreases the thickness of the disk as expected from standard accretion disk theory and can be explained as follows: the vertical structure of thin, stable disks is assumed to be in hydrostatical equilibrium

$$\frac{\partial P}{\partial z} = \rho g_z \tag{10.1}$$

with gas pressure

$$P = \frac{kT}{m}\rho \tag{10.2}$$

and vertical gravitational acceleration

$$g_z = -\frac{GM_{\mathrm{BH}}}{r^2}\frac{z}{r}\,. \tag{10.3}$$

Here k is the Boltzmann constant, T the temperature, m the particle mass and r the distance to the black hole. We furthermore assume that the disk is isothermal in vertical direction. Inserting the last two expressions in eq. 10.1, and solving the resulting

differential equation with the Ansatz

$$\rho = \rho_0 \exp\left[-\left(\frac{z}{h}\right)^2\right] \tag{10.4}$$

gives the height of the disk

$$h = \sqrt{\frac{2kTr^3}{GMm}}\,. \tag{10.5}$$

Thus as cooling decreases the temperature it also decreases the disk height.

The bottom panel of Fig. 10.1 shows vertical cross sections of the disk temperature. Without cooling the temperature reaches values of several thousand Kelvin at a distance of about 2 pc from the black hole, very close to the black hole the temperature even exceeds 10 000 K. With cooling enabled the disk temperature reaches values of several 100 K, and only drops below 100 K close to the disk's outer radius. Thus our cooling algorithm roughly provides temperatures of some 100 K as observed in the CND.

Fig. 10.2 shows a time sequence of the 3D density of the CND with cooling enabled. The elongated structure sticking out of the disk's outer rim is a numerical artifact due to the cubical geometry of the computational domain. But as its density is much smaller than the disk's density this artifact does not influence the development of the disk. The vertical density distribution changes from the initially uniform distribution to the exponential distribution eq. 10.4, leading to the inner part of the disk being compressed. According to Fig. 10.2 in less than two orbital timescales the disk reaches a global equilibrium state that is maintained until the end of the simulation. However, small instabilities still occur due to the nonlinearity of the MHD equations. Thus our model and our parameters provide a good basis for further investigations of the CND.

10.2. Magnetic fields

We now investigate the interaction of the disk with magnetic fields. The simulations presented in this section still omit the inner cavity and central outflow. As stated in chapter 8 the magnetic field in the CND is observed to have a uniform field strength of 1 mG. However, in this section we will only use a field strength of 0.1 mG, because strong magnetic fields require more computing time. But it is sufficient to give a general impression of the influence of magnetic fields on the disk. For the full simulation presented in section 10.5 we will use a field strength of 1 mG.

Initially toroidal field

We first use an initially toroidal magnetic field configuration, as it is observed in the CND. Initially the magnetic field is confined to the location of the disk. In Fig. 10.3

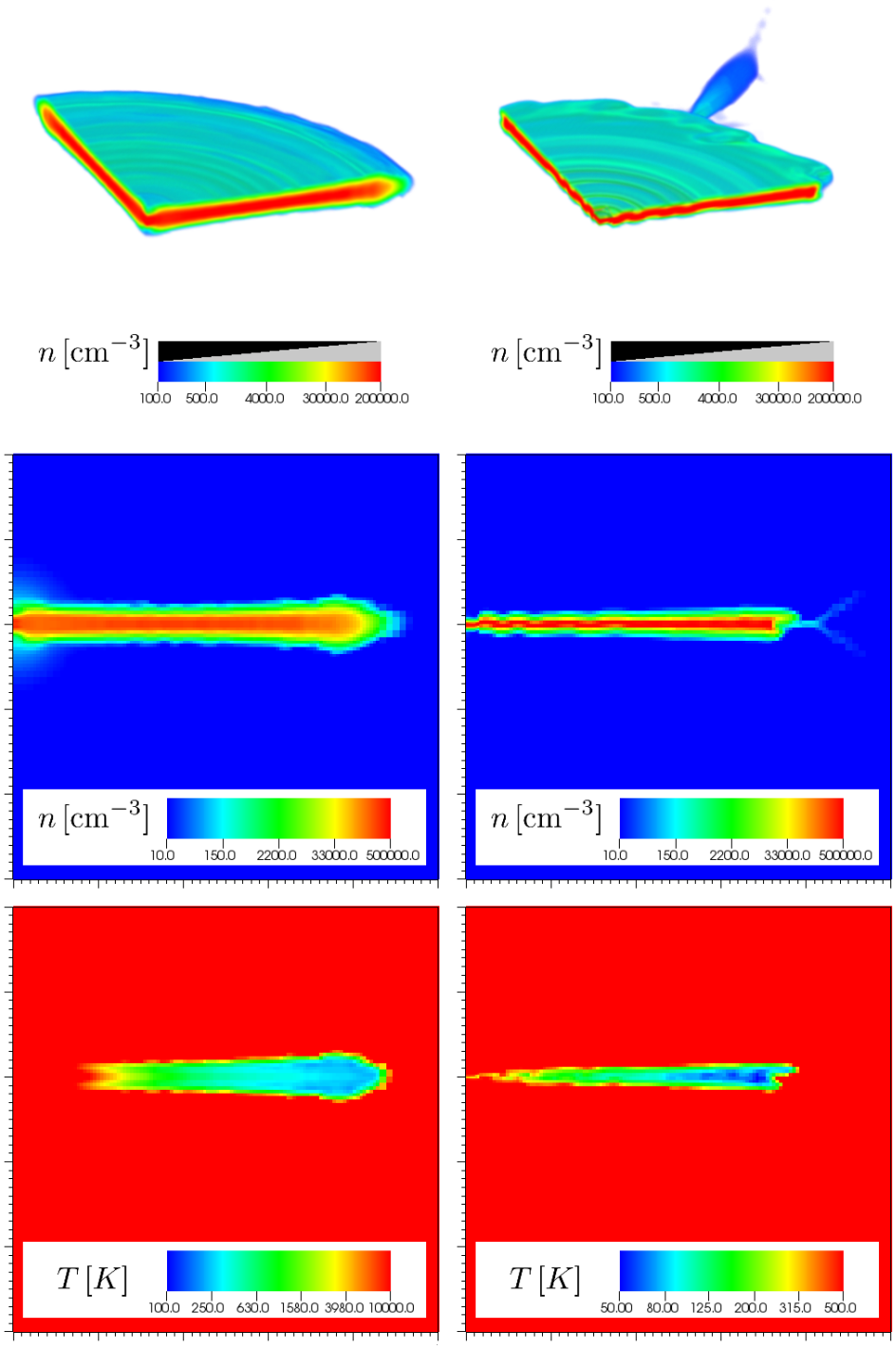

Figure 10.1.: Simulations of the CND without magnetic fields, outflow and inner cavity, all at time $10\,\tau_{\mathrm{orb}}$. Left: without cooling, right: with cooling. Top: 3D density, middle: vertical cross section of the density, bottom: vertical cross section of the temperature. Middle and Bottom: the plots show a region of size $5\times5\,\mathrm{pc}$, the black hole is located at the left edge of the plot.

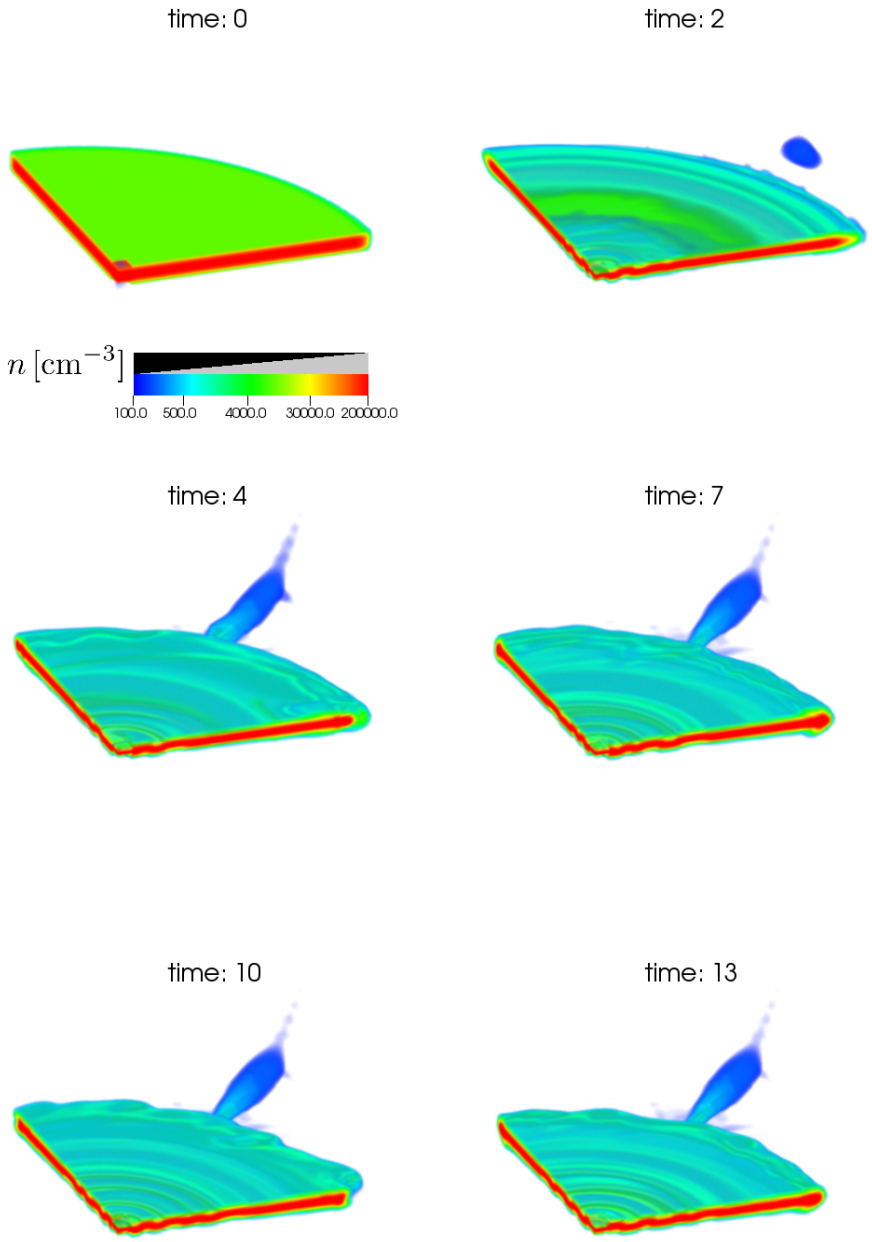

Figure 10.2.: 3D density of the CND at different times. Simulation does not include magnetic fields, outflow or inner cavity, but includes cooling. The time is given in units of τ_{orb}.

we show the magnetic field strength at the disk's midplane. The field strength in the central parsec strongly increases to up to 5 mG, but this is not relevant as in our later simulations we will cut out this part of the disk to create the inner cavity. In the other parts of the disk the field strength only increases slightly. As stated in section 10.1 the disk is being compressed in the vertical direction because of its adjustment from the initial conditions, and in the framework of ideal MHD compression of gas leads to an increase in magnetic field strength. As a result we get a magnetic field configuration that is stable over at least 13 orbital timescales and is in accordance with the observed properties of the CND, making this a good approach to model the CND's magnetic field.

Initially vertical field

The CND's magnetic field is observed to be toroidal, but the Galactic Center's magnetic field on larger scales (about 100 pc) is observed to have a vertical configuration, i.e., perpendicular to the CND. It has been argued that the rotation of the CND drags the initially vertical field into a toroidal configuration. In this section we test this scenario by presenting a simulation whose initial magnetic field has again a field strength of 0.1 mG, but its configuration is vertical throughout the whole computational domain. Fig. 10.4 shows the magnetic field strength in the disk's midplane. Again the field strength increases slightly as seen in the previous section. Furthermore after about four orbital timescales the magnetic field has adopted a toroidal configuration. At 13 orbital timescales the magnetic fields of Figs. 10.3 and 10.4 are very similar. However, there is one noteworthy difference between both approaches. The initially toroidal field has a counterclockwise orientation which is maintained at all times. The initially vertical field gets dragged into a toroidal configuration but the direction of the magnetic field reverses at the disk's midplane. But there is no noticeable difference between the outcome of both approaches. In Fig. 10.5 we plot the CND's magnetic field lines and show how the initially vertical field lines get dragged into a toroidal configuration due to the disk's rotation.

Both approaches presented in this section provide a magnetic field configuration that is in agreement with observations. However, we will use the toroidal configuration for the remainder of this thesis, because otherwise we have to simulate about four orbital timescales until we reach the observed field configuration, which consumes a huge amount of computational resources.

10.3. Interaction of the outflow with the inner rim

In this section we investigate the interaction of the outflow with the CND's inner rim, but still without magnetic fields. In Fig. 10.6 the surface density of the disk's inner region at different times is plotted, and Fig. 10.7 shows the corresponding radial density profiles in blue. As no viscosity is implemented in our simulations, one would expect

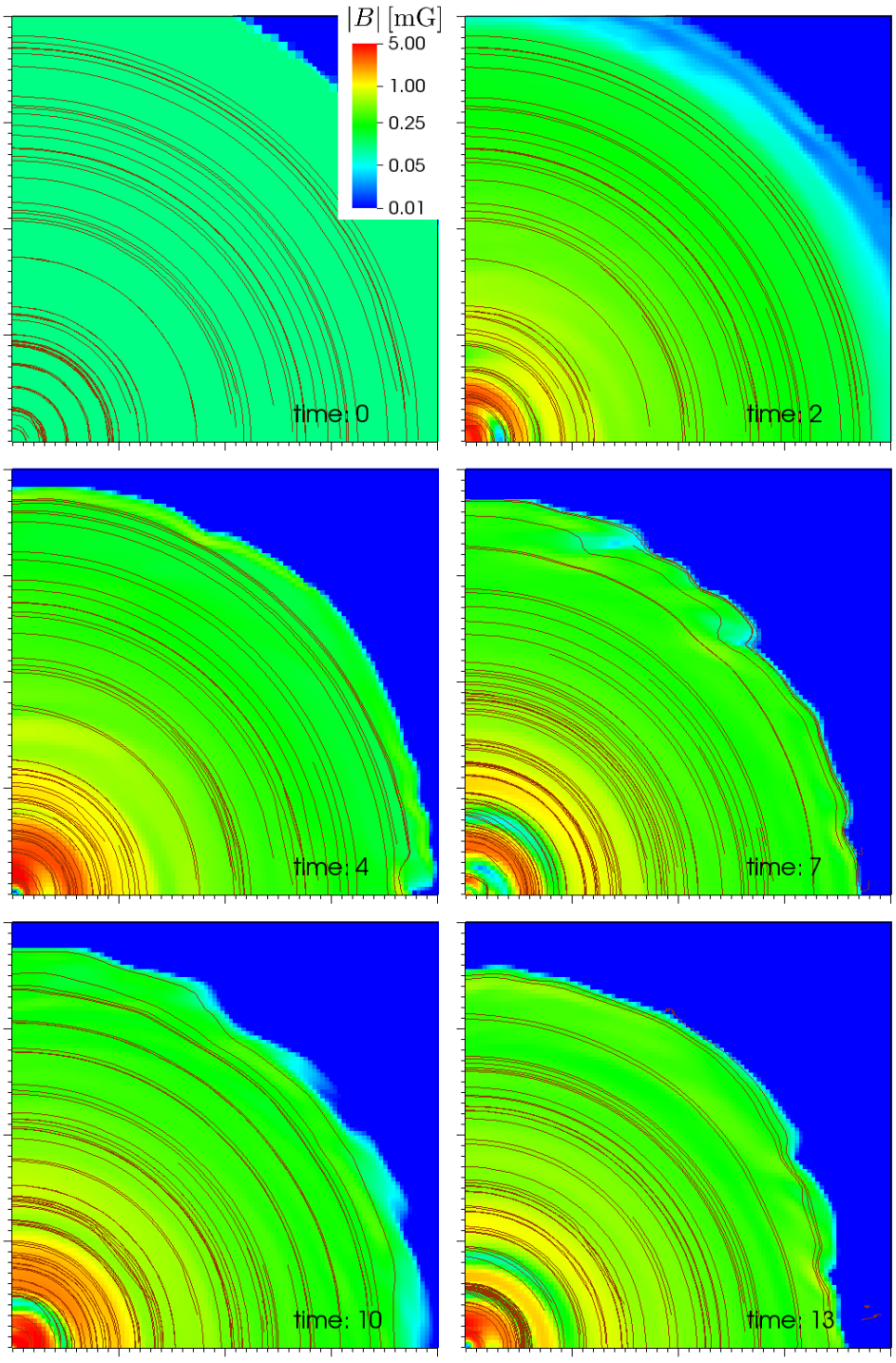

Figure 10.3.: Absolute value of the magnetic field strength at the disk's midplane for different times. The initial magnetic field is toroidal and has a uniform field strength of 0.1 mG. Each snapshot shows a region of size 4×4 pc. The time is given in units of τ_{orb}. Magnetic field lines are shown as brown lines.

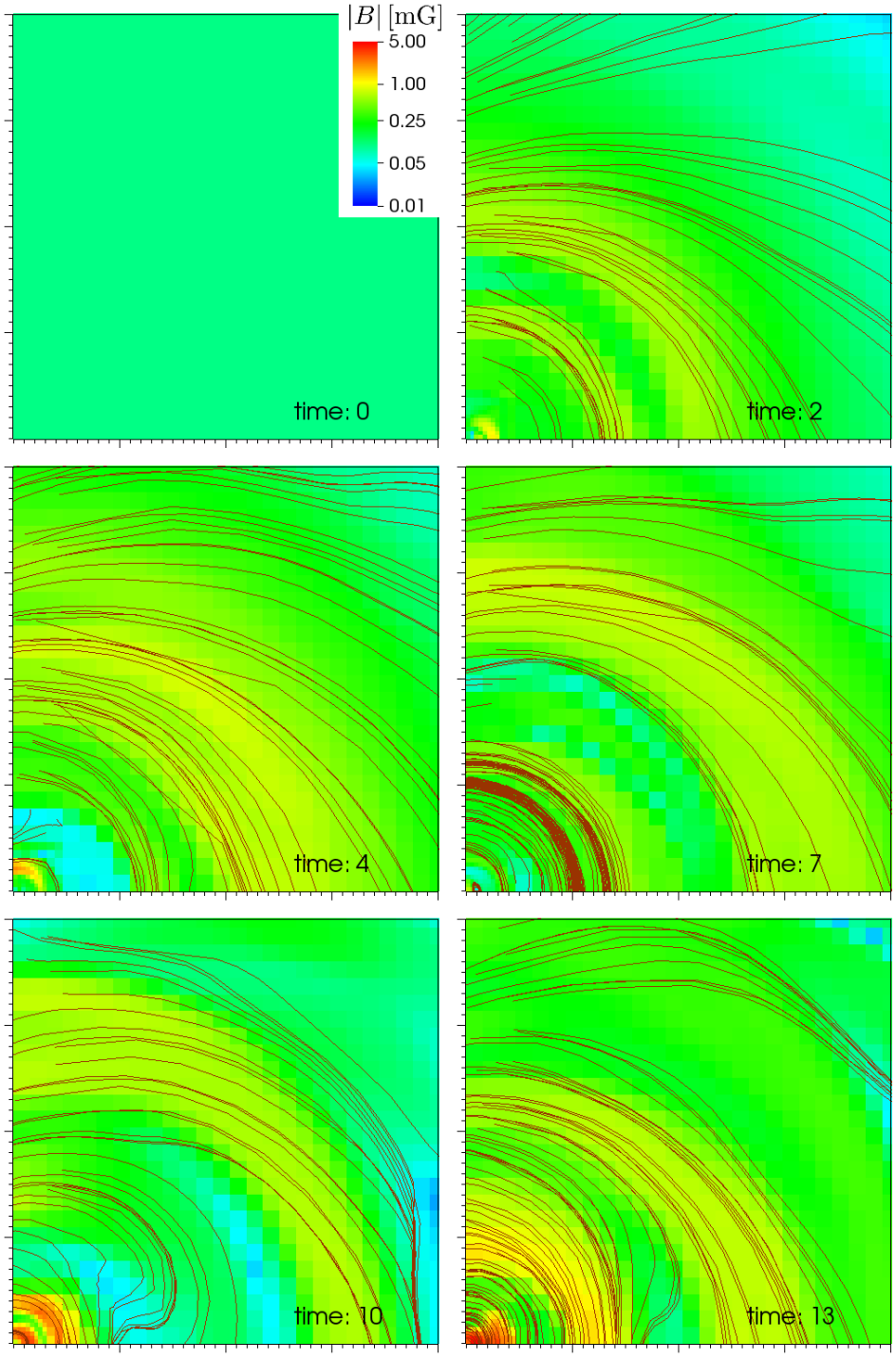

Figure 10.4.: Absolute value of the magnetic field strength at the disk's midplane for different times. The initial magnetic field is vertical and has a uniform field strength of 0.1 mG. Each snapshot shows a region of size 4×4 pc. The time is given in units of τ_{orb}. Magnetic field lines are shown as brown lines.

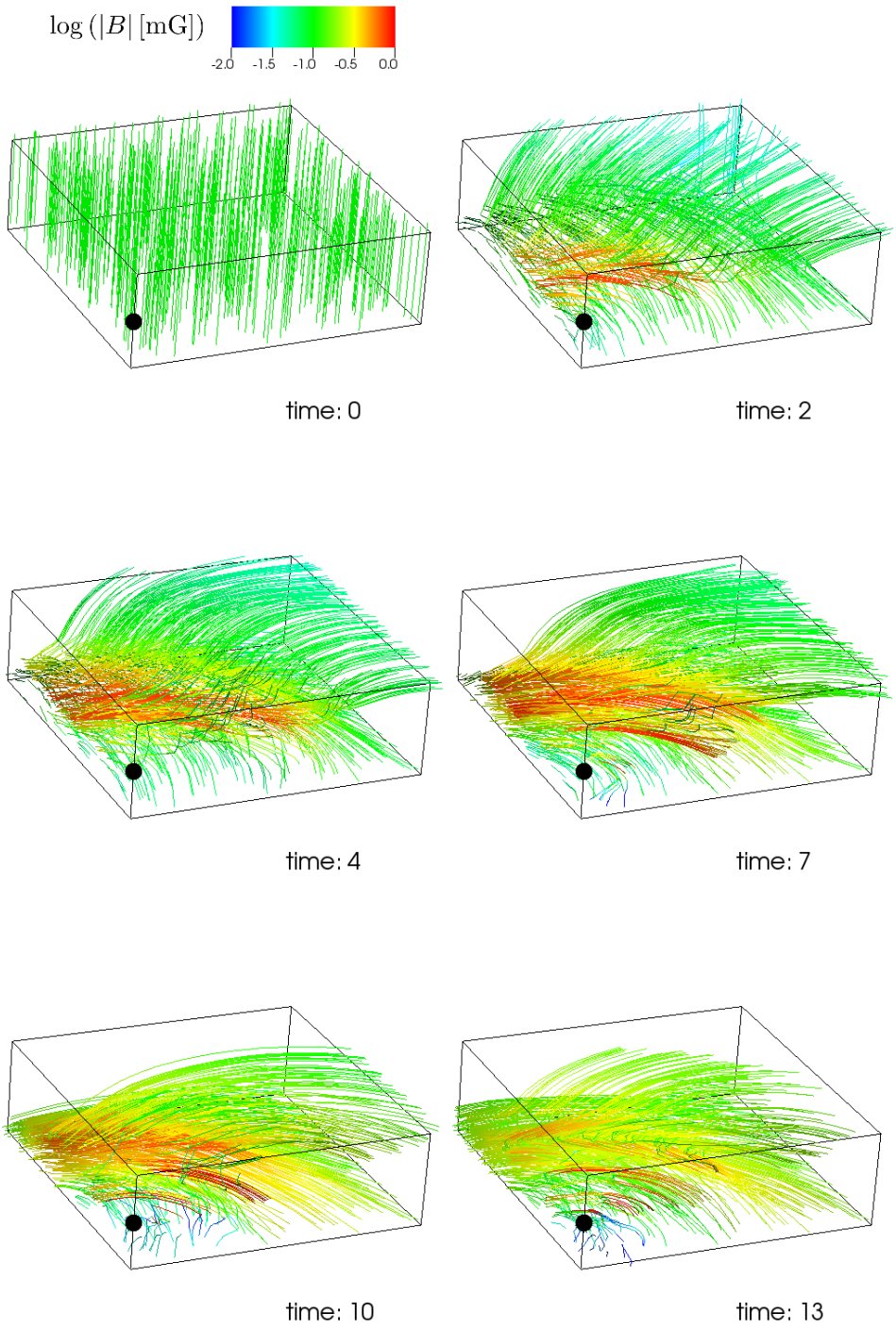

Figure 10.5.: Magnetic field lines in a box of size 4×4×1.6 pc. The initial magnetic field is vertical and has a uniform field strength of 0.1 mG. The time is given in units of $\tau_{\rm orb}$. The black dot marks the location of the black hole.

the disk's inner rim to be pushed outwards by the outflow, or at least that the inner cavity maintains a stable configuration if the outflow's momentum is not strong enough to push the inner rim outwards.

But Figs. 10.6 and 10.7 show that within four orbital timescales the density in the inner cavity increases by more than two orders of magnitude, from about $1\,M_\odot pc^{-2}$ to some $100\,M_\odot pc^{-2}$. Only very close to the outflow object, within a distance of 0.1 pc, are there still some low-density regions in the form of a "sawtooth pattern". Thus the inner rim quickly moves inwards until it has reached the location of the outflow object. We emphasize again that due to the numerical setup no material can enter the inner 0.5 pc where the outflow is launched, thus the inner rim stops migrating inwards at this radius. Contrary to what one would expect and what has been previously assumed in the literature, the interaction of outflow and CND's inner rim causes the latter to shrink. The outflow from the central stellar cluster does not maintain the inner cavity, it destroys it.

The extraction of angular momentum in the absence of physical viscosity can be explained as follows: By interacting with the CND's inner rim the outflow is adding mass to the inner rim. Thus its mass increases, but its angular momentum does not change, as the outflow does not carry any angular momentum. As a result, the specific angular momentum, the angular momentum per unit mass, decreases and thus angular momentum can be efficiently extracted from the disk.

Furthermore the interaction of the outflow with the CND's inner rim creates instabilities at their interface as shown in Fig. 10.6. The nature of this instability is probably a combination of Kelvin-Helmholtz and Rayleigh-Taylor instability: Our model consists of two fluids (the outflow and the disk) with different densities separated by an interface and with a velocity difference across the interface. The only difference to the classical Kelvin-Helmholtz instability is that the velocity of one of the fluids (in this case the outflow, i.e., the lighter fluid) is perpendicular to the interface. This in turn implies the lighter fluid being pushed into the other, and thus suggests the occurrence of a Rayleigh-Taylor instability.

10.4. The effect of numerical viscosity

Here we show that the shrinkage of the inner cavity shown in Section 10.3 is not caused by numerical viscosity by running a simulation without magnetic fields and without a central outflow. An accretion disk without physical viscosity, magnetic fields or a central outflow would retain a stable inner cavity at all times. However, numerical viscosity will lead to a small accretion rate of material towards the center and hence the inner rim will shrink on long timescales. Fig. 10.8 shows the disk's surface density for different times, and Fig. 10.7 the corresponding radial density profiles in magenta. As the disk has to relax from its initial conditions (the initial pressure and the initial density both

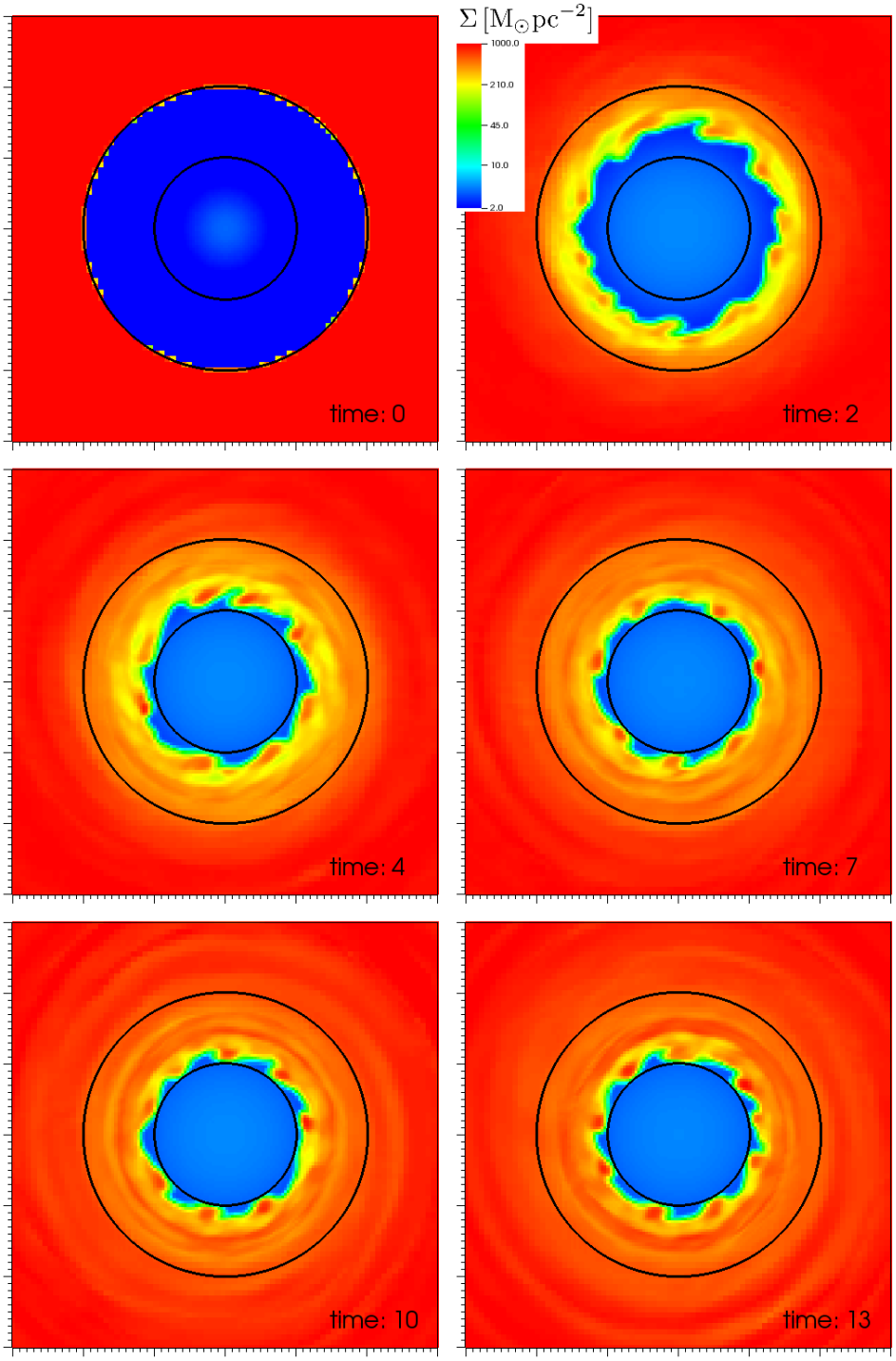

Figure 10.6.: Surface density of the inner disk for different times, this simulation does not include magnetic fields. Each snapshot shows a region of size $3\times3\,\mathrm{pc}$. The time is given in units of τ_{orb}. The outer black circle marks the location of the disk's initial inner rim, the inner black circle marks the region where the outflow is launched.

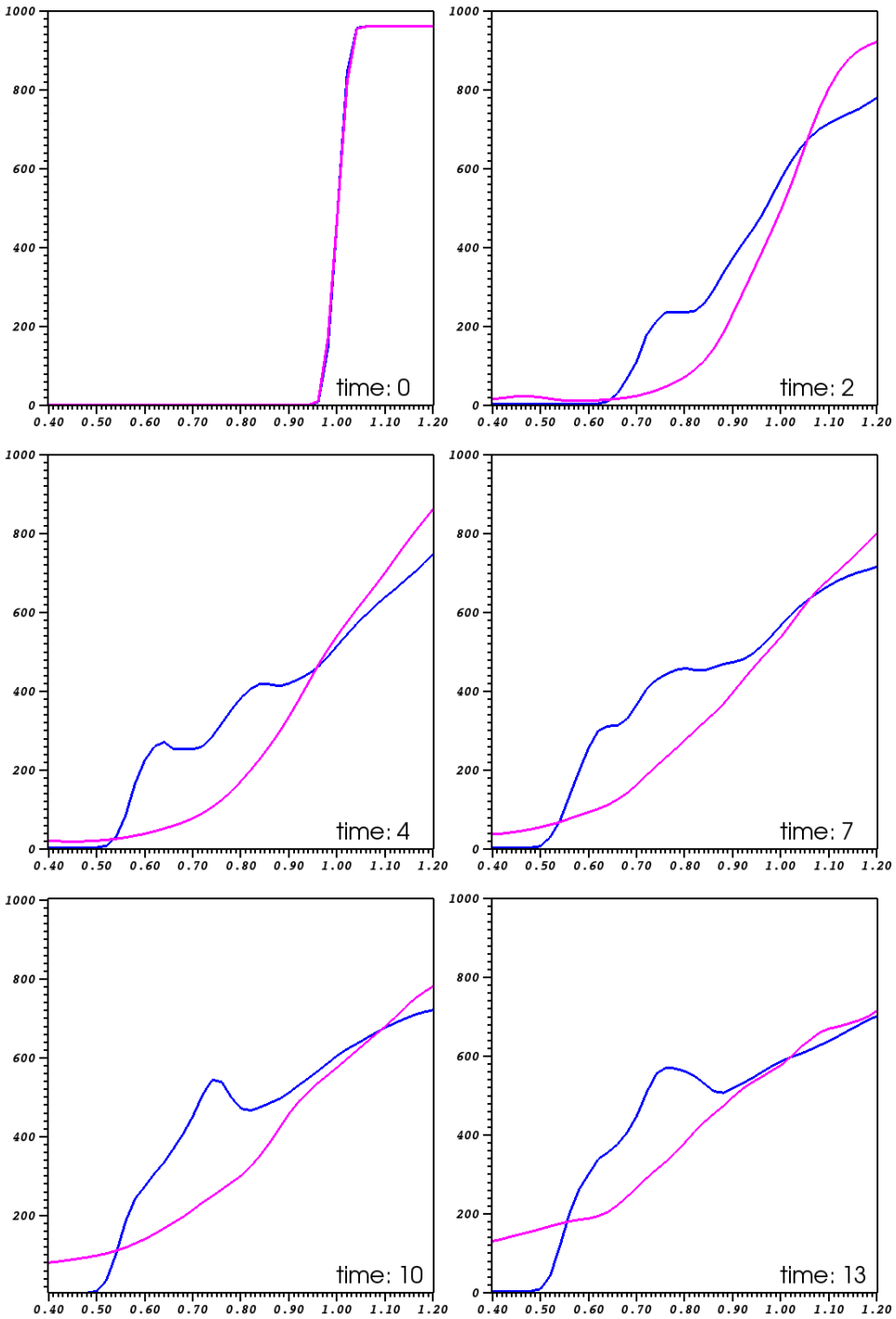

Figure 10.7.: Radial profiles for the surface density. Blue: without magnetic fields but with outflow. Magenta: without magnetic fields and without central outflow. The time is given in units of τ_{orb}. The profiles have been calculated by using radial bins of the surface density with a bin size of 0.02 pc

have discontinuities) and due to numerical viscosity the inner rim slowly moves inwards and the inner cavity gets populated by a low-density gas. After four orbital timescales the density inside the inner cavity is 20-30 times smaller than the disk's density. After 13 orbital timescales the density is about a factor 5 smaller than the disk's density. But according to Fig. 10.7, the surface density in the inner cavity is always a factor of about 2-4 lower than the surface density of last section's simulation, so we can rule out numerical viscosity as the explanation for the shrinkage of the inner cavity.

10.5. Full simulation

The simulation presented in this section now includes magnetic fields as described in Section 9.3. Fig. 10.9 shows again the surface density of the CND's inner region at different times, and Fig. 10.10 shows the corresponding surface density profiles compared to the simulation with outflow but without magnetic field. Clumps and streams are formed at the disk's inner rim and move inwards.

But aside from that the density inside the inner cavity stays relatively low; with values of about $100\,\mathrm{M}_\odot\,\mathrm{pc}^{-2}$ it is still about 10 times lower than the density of the disk. Thus magnetic fields seem to play an important role in maintaining a stable inner cavity and in preventing the CND's inner rim from shrinking. As the magnetic field is frozen into the plasma in the framework of ideal MHD, any chunk of material that moves towards the black hole deforms the otherwise toroidal magnetic field lines. This deformation results in a restoring force, the magnetic tension force $(\vec{B}\cdot\nabla)\vec{B}/4\pi$, that counteracts the inwards movement of matter and thus stabilizes the disk against collapse.

In Fig. 10.11 we show the absolute value of the magnetic field with magnetic field lines. The magnetic field basically keeps its initial toroidal configuration; only inside the inner cavity is it deformed by the clumps and streams of matter that are moving inwards. These streams have very high field strengths of 2-3 mG, because in the framework of ideal MHD the high density of the clumps implies a high magnetic energy density.

10.6. Clumping in the circumnuclear disk

As already shown in Section 10.5 the interaction of the disk's inner rim with the central outflow creates instabilities that lead to the formation of streams and clumps, which then move inwards. In Fig. 10.12 we show the density at the midplane of the disk for different times. The clumps have densities of about $10^5\,\mathrm{cm}^{-3}$ and sizes of 0.1-0.2 pc, which correspond to the observed properties of the clumps in the CND. However, these clumps are not stable against tidal shearing and thus get destroyed after a short period of time.

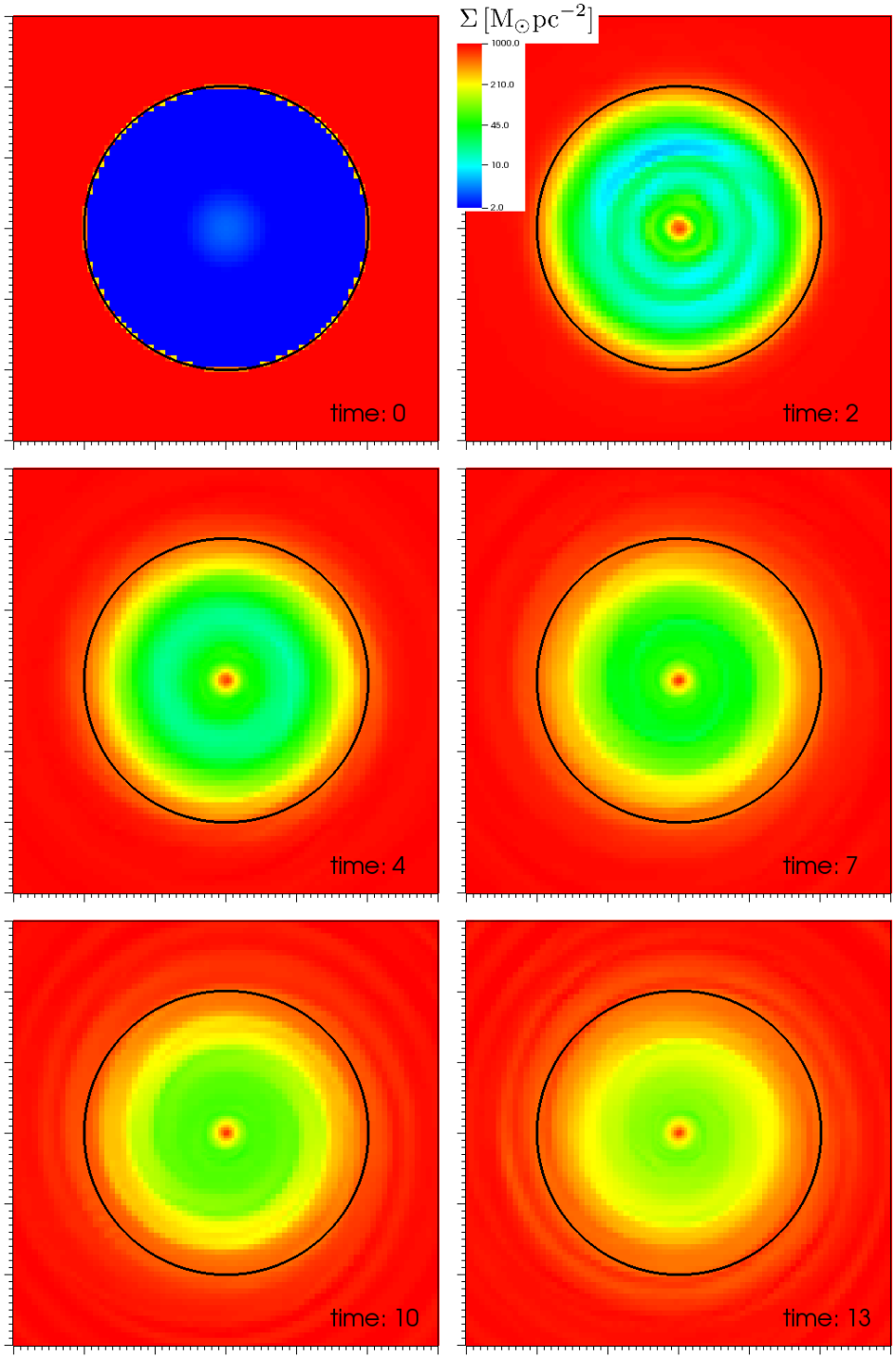

Figure 10.8.: Surface density of the inner disk for different times, this simulation does not include magnetic fields and the central outflow. Each snapshot shows a region of size $3\times3\,\mathrm{pc}$. The time is given in units of τ_{orb}. The black circle marks the location of the disk's initial inner rim.

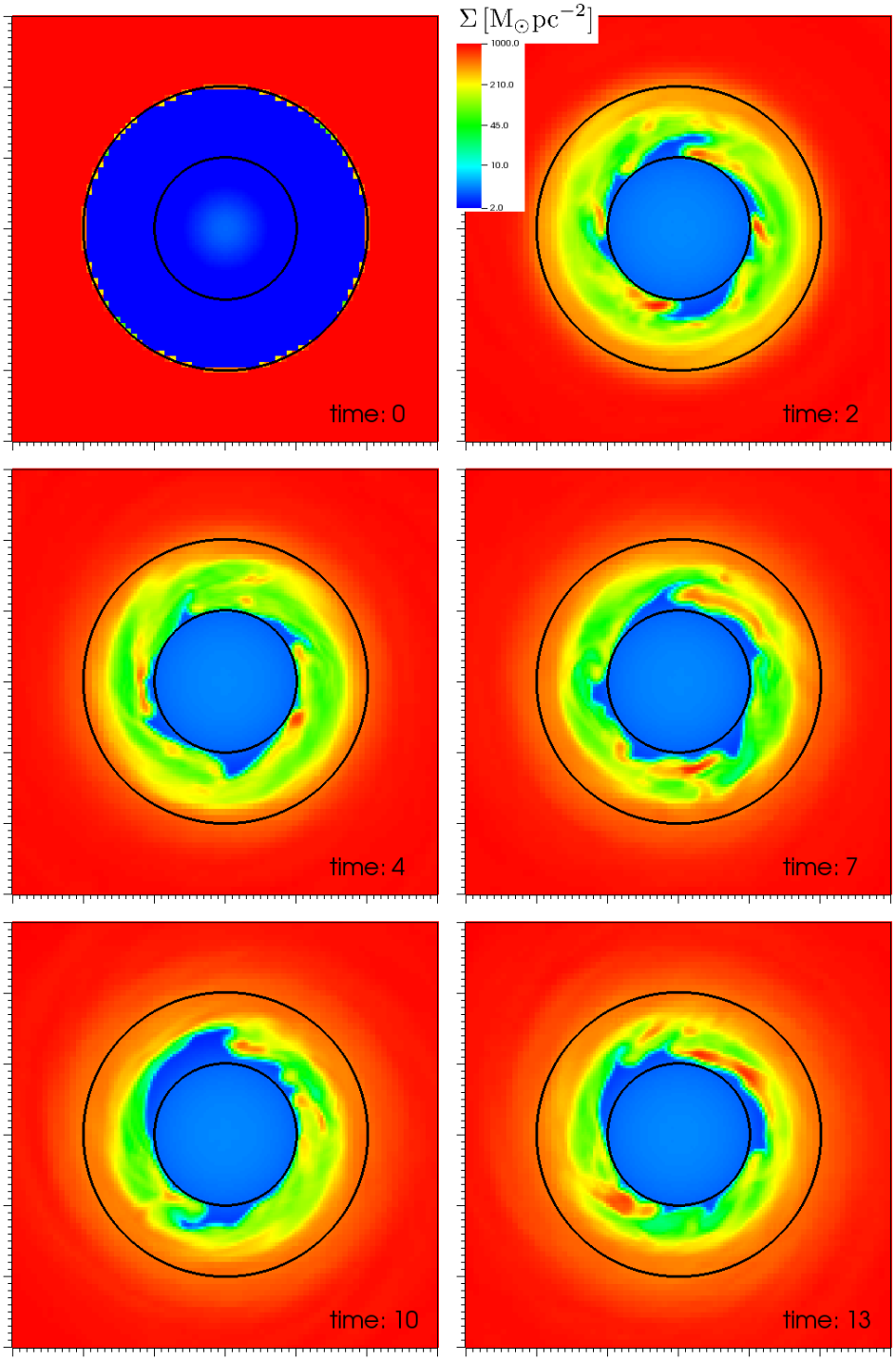

Figure 10.9.: Surface density of the inner disk for different times, this simulation includes magnetic fields and the central outflow. Each snapshot shows a region of size $3\times3\,\mathrm{pc}$. The time is given in units of τ_{orb}. The outer black circle marks the location of the disk's initial inner rim, the inner black circle marks the region where the outflow is launched.

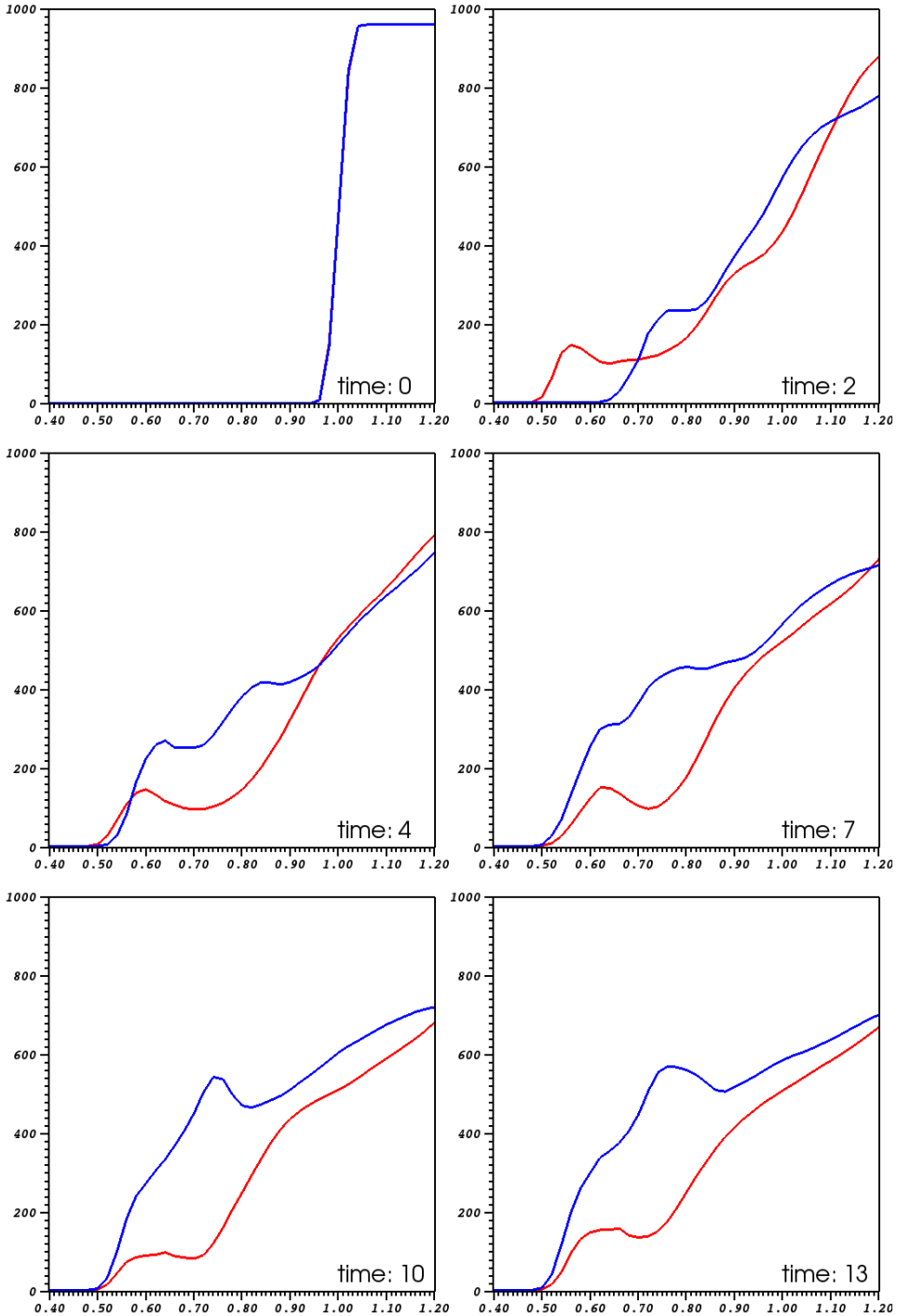

Figure 10.10.: Radial profiles for the surface density. Blue: without magnetic field but with central outflow. Red: with magnetic fields and with central outflow. The time is given in units of τ_{orb}. The profiles have been calculated by using radial bins of the surface density with a bin size of 0.02 pc

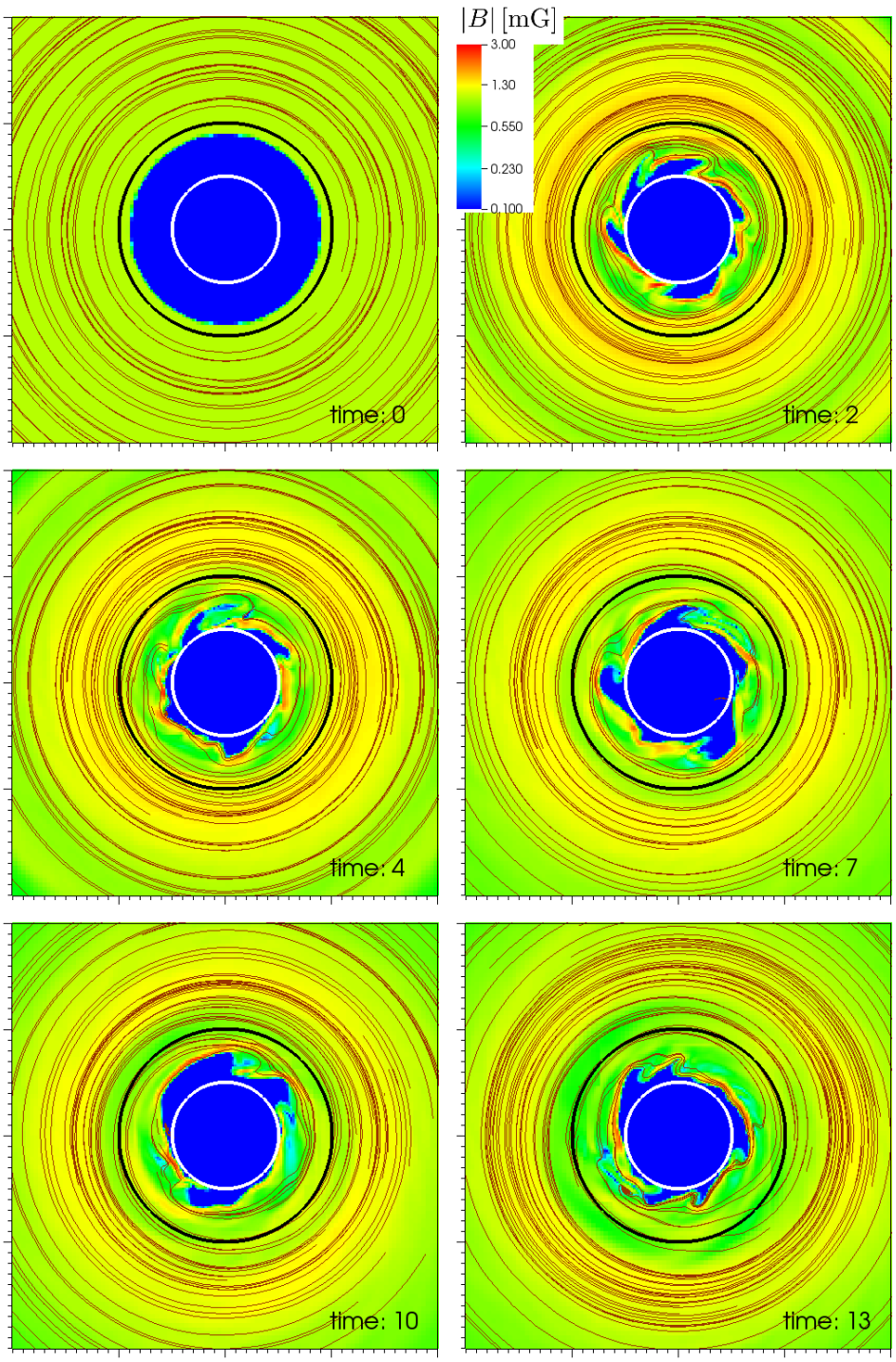

Figure 10.11.: Absolute value of the magnetic field strength at the disk's midplane for different times. Each snapshot shows a region of size $4\times4\,\mathrm{pc}$. The time is given in units of τ_{orb}. The black circle marks the location of the disk's initial inner rim, the white circle marks the region where the outflow is launched. Magnetic field lines are shown as brown lines.

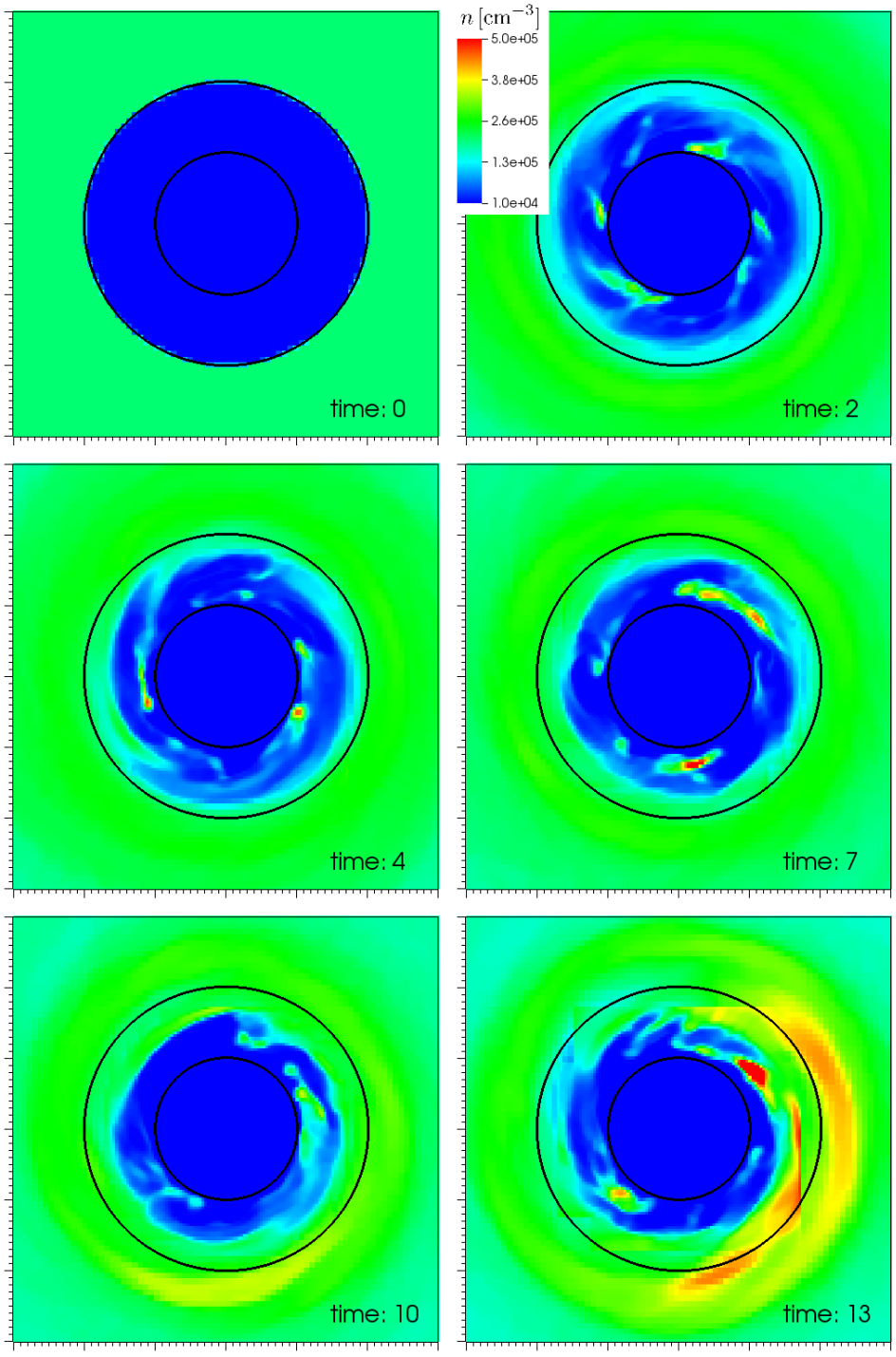

Figure 10.12.: Density at the disk's midplane for different times. Each snapshot shows a region of size 3×3 pc. The time is given in units of τ_{orb}. The outer black circle marks the location of the disk's initial inner rim, the inner black circle marks the region where the outflow is launched.

Previously it has been argued that the presence of unstable clumps in the vicinity of the black hole suggests that the CND is a transient feature. Our results show that this must not necessarily be true, as we have demonstrated that such clumps can be created at the CND's inner rim due to its interaction with the central outflow.

11. Conclusions of part II

In part II of this thesis we have investigated the interaction of the CND's inner rim with the outflow from the central stellar cluster. The results of our simulations show that it is not the outflow that maintains the CND's inner cavity, contrary to what has previously been assumed. On the contrary, the interaction of the outflow with the inner rim extracts angular momentum from the latter, and causes the inner rim to shrink within a few orbital timescales.

We have provided a qualitative explanation for the angular momentum extraction, but it would be worthwhile to develop a more sophisticated model that provides the timescale and the efficiency of angular momentum extraction. In our simulations the inner rim moves from 1 pc to 0.5 pc within about four orbital timescales, and is thus potentially much more efficient than angular momentum extraction due to viscous processes, which takes at least 100 orbital timescales. This mechanism might actually be a new method for angular momentum extraction of accretion disks, that could also be relevant, e.g., for protoplanetary disks around young stars. However, including magnetic fields in our simulations prevents the inner rim from shrinking and supports a stable inner cavity.

Furthermore the interaction of the inner rim with the outflow creates instabilities, which lead to the formation of clumps. We have argued that these instabilities are probably a combination of Kelvin-Helmholtz and Rayleigh-Taylor instability, but only a stability analysis of this system would reveal the true nature of this instability. The clumps produced have the same properties as the clumps that are observed in the CND. However, they are not stable against tidal shearing. Thus the presence of unstable clumps in the CND cannot be used to argue that the CND is a transient phenomenon.

Our results explain how the inner cavity is maintained and thus why the Galactic Center is currently in a quiescent state. However, although the stellar cluster's wind does not maintain the inner cavity, it still exerts a ram pressure onto the CND's inner rim. Therefore it is possible that the disk will start to migrate inwards as soon as the cluster stars perish and their winds subside. This could lead to a subsequent episode of black hole accretion and star formation. In our future work we will investigate the development of the CND due to the fading of the stellar cluster's wind. Thus our research presented in part II of this thesis represents a first step for investigating the limit cycle idea proposed by Morris et al. (1999), aiming to reveal the possibility of a starburst-AGN connection in the Galactic Center.

12. Summary

In this thesis we investigated starbursts and active nuclei in galaxies. These processes are predominantly observed in galaxy mergers, but there is also evidence for a recent starburst and AGN activity in the center of our own Galaxy. Thus we investigated these phenomena on two scales: on large scales due to galaxy mergers, and on small scales in the Galactic Center. The detailed outcome of these two approaches we already summarized in the conclusions of part I and part II, in this chapter we will close with some general remarks about the starburst-AGN connection and on how the results of the two parts of this thesis are connected to each other.

In part II we elaborated on the possibility of a cyclic activity, where the Milky Way's center is alternating between starbursts and AGN activity. Whereas this scenario is possibly applicable to the centers of other isolated disk galaxies, it is questionable if merger systems are subject to such a cycle. The most crucial point here is if AGN feedback can trigger star formation, as is required for establishing a cyclic starburst and AGN activity. In our merger simulations AGN feedback completely quenches star formation, but due to a limited resolution star formation on small scales might be suppressed. Zubovas et al. (2013) point out that the gas around AGN, if properly resolved, forms a two-phase medium consisting of cold high-density and hot low-density regions. AGN feedback will then blow away the low-density gas and compress the high-density gas, thus triggering star formation in the cold high-density regions. If such a cyclic activity can be established in merger systems, the long term AGN activity, that is shaped by the merger event, would be subdivided into cycles of $\sim 10^7$ yrs. Thus as we cannot resolve such short timescales (and such small spatial scales) in the simulations presented in part I, the BHARs that we showed in part I could be interpreted as BHARs averaged over timescales $> 10^7$ yrs.

Thus it is of great interest to further investigate the possibility of cyclic starburst and AGN activity in the Galactic Center. Our Milky Way provides a unique opportunity to study these processes in great detail and can provide a basis for understanding the formation and evolution of galactic centers in general.

A. List of acronyms

AGN	active galactic nucleus
AGNAR	accretion rate of the AGN particle
AMR	adaptive mesh refinement
BH	black hole
BHAR	black hole accretion rate
CND	circumnuclear disk
FB	feedback
GC	Galactic Center
SF	star formation
SFR	star formation rate

B. The stellar velocity dispersion

The stellar velocity dispersion σ is defined as the statistical dispersion around the mean velocity of the stars of a galaxy. This is a very important quantity in astrophysics, as it is easy to measure and leads to some important scaling relations for elliptical galaxies. The most important ones are the Faber-Jackson relation $L \sim \sigma^4$, that relates the stellar velocity dispersion to the galaxy's luminosity L, the relation between galaxy mass and stellar velocity dispersion and the $M_{\rm BH}$-σ correlation[1] that we widely use in this thesis. The stellar velocity dispersion is usually determined by measuring the Doppler width of spectral lines, thus it is only possible to determine the stellar velocity dispersion along the line-of-sight. Therefore it is principally used in systems that are believed to be isotropic, e.g., thermally supported rather than rotationally supported systems, like galactic bulges or elliptical galaxies.

How to measure σ

We measure the stellar velocity dispersion of our merger remnants following Debuhr et al. (2011), who use a method analogous to observers. First we determine the remnant's center of mass and choose a random axis through this center. For observers this axis is always the line-of-sight. We then project all stars onto an area perpendicular to this axis and determine their distances to the axis and their line-of sight velocities $v_{\rm los}$, i.e., the velocity component parallel to the axis. We furthermore determine the half-mass radius $R_{\rm e}$, i.e., the radius that encloses half of the total stellar mass. The stars within $R_{\rm e}$ are then divided into a number of N cylindrical bins each with mass m_i. In each bin i the mean line-of-sight velocity is then calculated as

$$\overline{v}_{{\rm los},i} = \frac{1}{N_i} \sum_{j=1}^{N_i} v_{{\rm los},j} \tag{B.1}$$

and the stellar velocity dispersion as

$$\sigma_i^2 = \frac{1}{N_i} \sum_{j=1}^{N_i} \left(\overline{v}_{{\rm los},i} - v_{{\rm los},j}\right)^2 \tag{B.2}$$

[1] It is thought that the $M_{\rm BH}$-σ correlation is valid also for disk galaxies, when measuring the stellar velocity dispersion of the galaxy's bulge.

where N_i is the number of stars in bin i. We then calculate the total stellar velocity dispersion weighted the with the mass profile:

$$\sigma^2 = \frac{\sum_{i=1}^{N} \sigma_i^2 m_i}{\sum_{i=1}^{N} m_i} \tag{B.3}$$

This calculation is repeated for 500 randomly chosen axes, the value of σ that is used throughout this thesis is obtained by calculating the mean value and the standard deviation of these 500 values.

Measurement errors in elliptical galaxies

Elliptical galaxies are characterized by their ellipticity, which has a value of

$$E = 10 \cdot \left(1 - \frac{b}{a}\right) \tag{B.4}$$

rounded to the nearest integer, where a is the galaxy's projected major axis and b the projected minor axis. Thus a spherical galaxy with $a = b$ has an ellipticity of 0, and is classified as E0, galaxies with the highest observed ellipticity are about E7. However, only the projected ellipticity can be observed, therefore for observers it is not possible to differentiate between, e.g., a spherical galaxy and an oblate face-on galaxy.

For non-isotropic systems, like galaxies with a high ellipticity, the stellar velocity dispersion σ will depend on the direction along it is measured. Thus using the above approach, where isotropy is assumed, for non-isotropic systems will lead to large standard deviations. This effect we investigate in section 6.6. Merger events with a high inclination around $\theta = 90°$ will lead to elliptical galaxies with low ellipticities, which results in a small standard deviation for σ. Merger events with a low inclination around $\theta = 0°$ tend to form flat systems with high ellipticities, thus the standard deviation for σ is large. This measurement error is in general not accessible for observers, as they only measure the stellar velocity dispersion along the line-of-sight.

Scaling relations

As stated above the stellar velocity dispersion is related to important scaling relations. For an isotropic, virialized elliptical galaxy we can use the virial theorem with kinetic energy E_k and potential energy E_p.

$$2\,\langle E_\mathrm{k}\rangle = -\,\langle E_\mathrm{p}\rangle \tag{B.5}$$

A spherical distribution of matter with constant density, mass M and radius R has the potential energy

$$\langle E_\mathrm{p}\rangle = -\frac{3}{5}\frac{GM^2}{R}\,. \tag{B.6}$$

Assuming the galaxy consists of N stars, each with mass m, the kinetic energy is

$$\langle E_{\mathrm{k}} \rangle = \frac{m}{2} \sum_{i=1}^{N} \langle \vec{v}_i^2 \rangle = \frac{M}{2} \left[\langle v_x^2 \rangle + \langle v_y^2 \rangle + \langle v_z^2 \rangle \right] = \frac{3}{2} M \sigma^2 \tag{B.7}$$

with

$$\sigma^2 \equiv \langle v_x^2 \rangle = \langle v_y^2 \rangle = \langle v_z^2 \rangle \ . \tag{B.8}$$

Combining both terms in the virial theorem gives

$$\sigma^2 = \frac{2}{5} \frac{GM}{R} \, , \tag{B.9}$$

thus the galaxy's stellar velocity dispersion can be related to its mass and size:

$$\boxed{M \sim R \, \sigma^2} \tag{B.10}$$

If, e.g., $R \sim M^{1/3}$, as it is the case for our galaxy model (eq. 3.53), we get

$$M \sim \sigma^3 \, . \tag{B.11}$$

If we assume a constant surface brightness

$$\frac{L}{4\pi R^2} = \mathrm{const} \, , \tag{B.12}$$

which gives $R \sim \sqrt{L}$, and the galaxy's mass being proportional to its luminosity $M \sim L$, eq. B.10 yields the Faber-Jackson relation

$$\boxed{L \sim \sigma^4} \, . \tag{B.13}$$

This relation is well tested by observations and is used, e.g., to measure distances to other galaxies.

Bibliography

Bate M. R., Bonnell I. A., and Price N. M., Modelling accretion in protobinary systems, *MNRAS*, 277:362–376, November 1995.

Becklin E. E., Gatley I., and Werner M. W., Far-infrared observations of Sagittarius A - The luminosity and dust density in the central parsec of the Galaxy, *ApJ*, 258: 135–142, July 1982.

Beifiori A., Courteau S., Corsini E. M., and Zhu Y., On the correlations between galaxy properties and supermassive black hole mass, *MNRAS*, 419:2497–2528, January 2012.

Blank M., Das Wachstum Schwarzer Löcher in aktiven galaktischen Kernen, Diploma thesis, Christian-Albrechts-Universität zu Kiel, 2010.

Blank M. and Duschl W. J., A fresh look at the starburst-AGN connection, *Journal of Physics Conference Series*, 372(1):012053, July 2012.

Blank M. and Duschl W. J., Time lags between starburst and AGN activity in galaxy mergers, In Sjouwerman L. O., Lang C. C., and Ott J., editors, *IAU Symposium*, volume 303 of *IAU Symposium*, pages 379–381, May 2014a.

Blank M. and Duschl W. J., Viscous time lags between starburst and AGN activity, *in preparation*, October 2014b.

Blank M., Morris M. R., Frank A., Carroll-Nellenback J. J., and Duschl W. J., The inner cavity of the circumnuclear disk, *in preparation*, October 2014.

Bondi H., On spherically symmetrical accretion, *MNRAS*, 112:195, 1952.

Bondi H. and Hoyle F., On the mechanism of accretion by stars, *MNRAS*, 104:273, 1944.

Booth C. M. and Schaye J., Cosmological simulations of the growth of supermassive black holes and feedback from active galactic nuclei: method and tests, *MNRAS*, 398: 53–74, September 2009.

Bradford C. M., Stacey G. J., Nikola T., Bolatto A. D., Jackson J. M., Savage M. L., and Davidson J. A., Warm Molecular Gas Traced with CO J = 7-6 in the Galaxy's Central 2 Parsecs: Dynamical Heating of the Circumnuclear Disk, *ApJ*, 623:866–876, April 2005.

Carroll-Nellenback J. J., Shroyer B., Frank A., and Ding C., Efficient parallelization for AMR MHD multiphysics calculations; implementation in AstroBEAR, *Journal of Computational Physics*, 236:461–476, March 2013.

Cattaneo A., Combes F., Colombi S., Bertin E., and Melchior A.-L., Spectral and morphological properties of quasar hosts in smoothed particle hydrodynamics simulations of active galactic nucleus feeding by mergers, *MNRAS*, 359:1237–1249, June 2005.

Chen X. and Amaro-Seoane P., A Rapidly Evolving Region in the Galactic Center: Why S-stars Thermalize and More Massive Stars are Missing, *ApJ*, 786:L14, May 2014.

Choi E., Ostriker J. P., Naab T., and Johansson P. H., Radiative and Momentum-based Mechanical Active Galactic Nucleus Feedback in a Three-dimensional Galaxy Evolution Code, *ApJ*, 754:125, August 2012.

Chomiuk L. and Povich M. S., Toward a Unification of Star Formation Rate Determinations in the Milky Way and Other Galaxies, *AJ*, 142:197, December 2011.

Christopher M. H., Scoville N. Z., Stolovy S. R., and Yun M. S., HCN and HCO^+ Observations of the Galactic Circumnuclear Disk, *ApJ*, 622:346–365, March 2005.

Crank J., Nicolson P., and Hartree D. R., A practical method for numerical evaluation of solutions of partial differential equations of the heat-conduction type, *Proceedings of the Cambridge Philosophical Society*, 43:50, 1947.

Crowther P. A., Physical Properties of Wolf-Rayet Stars, *ARA&A*, 45:177–219, September 2007.

Cunningham A. J., Frank A., Varnière P., Mitran S., and Jones T. W., Simulating Magnetohydrodynamical Flow with Constrained Transport and Adaptive Mesh Refinement: Algorithms and Tests of the AstroBEAR Code, *ApJS*, 182:519–542, June 2009.

Davies R. I., Müller Sánchez F., Genzel R., Tacconi L. J., Hicks E. K. S., Friedrich S., and Sternberg A., A Close Look at Star Formation around Active Galactic Nuclei, *ApJ*, 671:1388–1412, December 2007.

Debuhr J., Quataert E., and Ma C.-P., The growth of massive black holes in galaxy merger simulations with feedback by radiation pressure, *MNRAS*, 412:1341–1360, April 2011.

Debuhr J., Quataert E., and Ma C.-P., Galaxy-scale outflows driven by active galactic nuclei, *MNRAS*, 420:2221–2231, March 2012.

Di Matteo T., Springel V., and Hernquist L., Energy input from quasars regulates the growth and activity of black holes and their host galaxies, *Nature*, 433:604–607, February 2005.

Downes D. and Solomon P. M., Rotating Nuclear Rings and Extreme Starbursts in Ultraluminous Galaxies, *ApJ*, 507:615–654, November 1998.

Duschl W. J., Strittmatter P. A., and Biermann P. L., A note on hydrodynamic viscosity and selfgravitation in accretion disks, *A&A*, 357:1123–1132, May 2000.

Eddington A. S., Das Strahlungsgleichgewicht der Sterne, *Z. Phys.*, 7:351–397, December 1921.

Ferrarese L. and Merritt D., A Fundamental Relation between Supermassive Black Holes and Their Host Galaxies, *ApJ*, 539:L9–L12, August 2000.

Friedli D. and Benz W., Secular evolution of isolated barred galaxies. II. Coupling between stars and interstellar medium via star formation., *A&A*, 301:649, September 1995.

Geballe T. R., Wade R., Krisciunas K., Gatley I., and Bird M. C., The broad-line region at the center of the Galaxy, *ApJ*, 320:562–569, September 1987.

Gebhardt K., Bender R., Bower G., Dressler A., Faber S. M., Filippenko A. V., Green R., Grillmair C., Ho L. C., Kormendy J., Lauer T. R., Magorrian J., Pinkney J., Richstone D., and Tremaine S., A Relationship between Nuclear Black Hole Mass and Galaxy Velocity Dispersion, *ApJ*, 539:L13–L16, August 2000.

Genzel R., The Circumnuclear Disk (review), In Morris M., editor, *The Center of the Galaxy*, volume 136 of *IAU Symposium*, page 393, 1989.

Genzel R., Crawford M. K., Townes C. H., and Watson D. M., The neutral-gas disk around the galactic center, *ApJ*, 297:766–786, October 1985.

Genzel R., Lutz D., Sturm E., Egami E., Kunze D., Moorwood A. F. M., Rigopoulou D., Spoon H. W. W., Sternberg A., Tacconi-Garman L. E., Tacconi L., and Thatte N., What Powers Ultraluminous IRAS Galaxies?, *ApJ*, 498:579–605, May 1998.

Genzel R., Eisenhauer F., and Gillessen S., The Galactic Center massive black hole and nuclear star cluster, *Reviews of Modern Physics*, 82:3121–3195, October 2010.

Ghez A. M., Salim S., Weinberg N. N., Lu J. R., Do T., Dunn J. K., Matthews K., Morris M. R., Yelda S., Becklin E. E., Kremenek T., Milosavljevic M., and Naiman J., Measuring Distance and Properties of the Milky Way's Central Supermassive Black Hole with Stellar Orbits, *ApJ*, 689:1044–1062, December 2008.

Gillessen S., Eisenhauer F., Trippe S., Alexander T., Genzel R., Martins F., and Ott T., Monitoring Stellar Orbits Around the Massive Black Hole in the Galactic Center, *ApJ*, 692:1075–1109, February 2009.

Gingold R. A. and Monaghan J. J., Smoothed particle hydrodynamics - Theory and application to non-spherical stars, *MNRAS*, 181:375–389, November 1977.

Graham A. W., Fundamental Planes and the Barless M_{bh}-σ Relation for Supermassive Black Holes, *ApJ*, 680:143–153, June 2008.

Graham A. W. and Scott N., The M_{BH}-$L_{spheroid}$ Relation at High and Low Masses, the Quadratic Growth of Black Holes, and Intermediate-mass Black Hole Candidates, *ApJ*, 764:151, February 2013.

Guesten R., Genzel R., Wright M. C. H., Jaffe D. T., Stutzki J., and Harris A. I., Aperture synthesis observations of the circumnuclear ring in the Galactic center, *ApJ*, 318:124–138, July 1987.

Gültekin K., Richstone D. O., Gebhardt K., Lauer T. R., Tremaine S., Aller M. C., Bender R., Dressler A., Faber S. M., Filippenko A. V., Green R., Ho L. C., Kormendy J., Magorrian J., Pinkney J., and Siopis C., The M-σ and M-L Relations in Galactic Bulges, and Determinations of Their Intrinsic Scatter, *ApJ*, 698:198–221, June 2009.

Harris A. I., Jaffe D. T., Silber M., and Genzel R., CO 7-6 submillimeter emission from the galactic center - Warm molecular gas and the rotation curve in the central 10 parsecs, *ApJ*, 294:L93–L97, July 1985.

Hernquist L., Structure of merger remnants. II - Progenitors with rotating bulges, *ApJ*, 409:548–562, June 1993.

Hildebrand R. H., Davidson J. A., Dotson J., Figer D. F., Novak G., Platt S. R., and Tao L., Polarization of the Thermal Emission from the Dust Ring at the Center of the Galaxy, *ApJ*, 417:565, November 1993.

Hopkins P. F., Dynamical delays between starburst and AGN activity in galaxy nuclei, *MNRAS*, 420:L8–L12, February 2012.

Hopkins P. F., Quataert E., and Murray N., Self-regulated star formation in galaxies via momentum input from massive stars, *MNRAS*, 417:950–973, October 2011.

Hoyle F. and Lyttleton R. A., The effect of interstellar matter on climatic variation, *Proceedings of the Cambridge Philosophical Society*, 35:405, 1939.

Jappsen A.-K., Klessen R. S., Larson R. B., Li Y., and Mac Low M.-M., The stellar mass spectrum from non-isothermal gravoturbulent fragmentation, *A&A*, 435:611–623, May 2005.

Johansson P. H., Naab T., and Burkert A., Equal- and Unequal-Mass Mergers of Disk and Elliptical Galaxies with Black Holes, *ApJ*, 690:802–821, January 2009.

Katz N., Dissipational galaxy formation. II - Effects of star formation, *ApJ*, 391:502–517, June 1992.

Katz N., Weinberg D. H., and Hernquist L., Cosmological Simulations with TreeSPH, *ApJS*, 105:19, July 1996.

Kennicutt R. C., Jr., The star formation law in galactic disks, *ApJ*, 344:685–703, September 1989.

Kennicutt R. C., Jr., The Global Schmidt Law in Star-forming Galaxies, *ApJ*, 498: 541–552, May 1998.

Khochfar S., *Origin and properties of elliptical galaxies in a hierarchical universe*, PhD thesis, University of Heidelberg, 2003.

Kormendy J. and Richstone D., Inward Bound—The Search For Supermassive Black Holes In Galactic Nuclei, *ARA&A*, 33:581, 1995.

Lau R. M., Herter T. L., Morris M. R., Becklin E. E., and Adams J. D., SOFIA/FORCAST Imaging of the Circumnuclear Ring at the Galactic Center, *ApJ*, 775:37, September 2013.

Lepp S. and Shull J. M., The kinetic theory of H2 dissociation, *ApJ*, 270:578–582, July 1983.

Lu J. R., Do T., Ghez A. M., Morris M. R., Yelda S., and Matthews K., Stellar Populations in the Central 0.5 pc of the Galaxy. II. The Initial Mass Function, *ApJ*, 764: 155, February 2013.

Lucy L. B., A numerical approach to the testing of the fission hypothesis, *AJ*, 82:1013–1024, December 1977.

Magorrian J., Tremaine S., Richstone D., Bender R., Bower G., Dressler A., Faber S. M., Gebhardt K., Green R., Grillmair C., Kormendy J., and Lauer T., The Demography of Massive Dark Objects in Galaxy Centers, *AJ*, 115:2285–2305, June 1998.

Marconi A. and Hunt L. K., The Relation between Black Hole Mass, Bulge Mass, and Near-Infrared Luminosity, *ApJ*, 589:L21–L24, May 2003.

Marr J. M., Wright M. C. H., and Backer D. C., HCO(+), H(C-13)N, and H(C-12)N aperture synthesis observations of the circumnuclear ring in the Galactic center, *ApJ*, 411:667–673, July 1993.

Martín S., Martín-Pintado J., Montero-Castaño M., Ho P. T. P., and Blundell R., Surviving the hole. I. Spatially resolved chemistry around Sagittarius A, *A&A*, 539:A29, March 2012.

Merritt D. and Ferrarese L., The M-σ Relation for Supermassive Black Holes, *ApJ*, 547: 140–145, January 2001.

Mezger P. G., Zylka R., Salter C. J., Wink J. E., Chini R., Kreysa E., and Tuffs R., Continuum observations of SGR A at mm/submm wavelengths, *A&A*, 209:337–348, January 1989.

Mo H. J., Mao S., and White S. D. M., The formation of galactic discs, *MNRAS*, 295: 319–336, April 1998.

Moe M., Arav N., Bautista M. A., and Korista K. T., Quasar Outflow Contribution to AGN Feedback: Observations of QSO SDSS J0838+2955, *ApJ*, 706:525–534, November 2009.

Monaghan J. J., Smoothed particle hydrodynamics, *ARA&A*, 30:543–574, 1992.

Montero-Castaño M., Herrnstein R. M., and Ho P. T. P., Gas Infall Toward Sgr A* from the Clumpy Circumnuclear Disk, *ApJ*, 695:1477–1494, April 2009.

Morris M., Ghez A. M., and Becklin E. E., The galactic center black hole: clues for the evolution of black holes in galactic nuclei, *Advances in Space Research*, 23:959–968, 1999.

Najarro F., Krabbe A., Genzel R., Lutz D., Kudritzki R. P., and Hillier D. J., Quantitative spectroscopy of the HeI cluster in the Galactic center., *A&A*, 325:700–708, September 1997.

Navarro J. F., Frenk C. S., and White S. D. M., The Structure of Cold Dark Matter Halos, *ApJ*, 462:563, May 1996.

Navarro J. F., Frenk C. S., and White S. D. M., A Universal Density Profile from Hierarchical Clustering, *ApJ*, 490:493, December 1997.

Ostriker J. P., Peebles P. J. E., and Yahil A., The size and mass of galaxies, and the mass of the universe, *ApJ*, 193:L1–L4, October 1974.

Plante R. L., Lo K. Y., and Crutcher R. M., The magnetic fields in the galactic center: Detection of H1 Zeeman splitting, *ApJ*, 445:L113–L116, June 1995.

Power C., Nayakshin S., and King A., The accretion disc particle method for simulations of black hole feeding and feedback, *MNRAS*, 412:269–276, March 2011.

Price D. J., splash: An Interactive Visualisation Tool for Smoothed Particle Hydrodynamics Simulations, *PASA*, 24:159–173, October 2007.

Price D. J., Smoothed particle hydrodynamics and magnetohydrodynamics, *Journal of Computational Physics*, 231:759–794, February 2012.

Pringle J. E., Accretion discs in astrophysics, *ARA&A*, 19:137–162, 1981.

Requena-Torres M. A., Güsten R., Weiß A., Harris A. I., Martín-Pintado J., Stutzki J., Klein B., Heyminck S., and Risacher C., GREAT confirms transient nature of the circum-nuclear disk, *A&A*, 542:L21, June 2012.

Salpeter E. E., Accretion of Interstellar Matter by Massive Objects., *ApJ*, 140:796–800, August 1964.

Sanders D. B., Soifer B. T., Elias J. H., Madore B. F., Matthews K., Neugebauer G., and Scoville N. Z., Ultraluminous infrared galaxies and the origin of quasars, *ApJ*, 325:74–91, February 1988.

Scannapieco C., Tissera P. B., White S. D. M., and Springel V., Feedback and metal enrichment in cosmological smoothed particle hydrodynamics simulations - I. A model for chemical enrichment, *MNRAS*, 364:552–564, December 2005.

Schawinski K., Virani S., Simmons B., Urry C. M., Treister E., Kaviraj S., and Kushkuley B., Do Moderate-Luminosity Active Galactic Nuclei Suppress Star Formation?, *ApJ*, 692:L19–L23, February 2009.

Schmidt M., The Rate of Star Formation., *ApJ*, 129:243, March 1959.

Shakura N. I. and Sunyaev R. A., Black holes in binary systems. Observational appearance., *A&A*, 24:337–355, 1973.

Smith M. C., Ruchti G. R., Helmi A., Wyse R. F. G., Fulbright J. P., Freeman K. C., Navarro J. F., Seabroke G. M., Steinmetz M., Williams M., Bienaymé O., Binney J., Bland-Hawthorn J., Dehnen W., Gibson B. K., Gilmore G., Grebel E. K., Munari U., Parker Q. A., Scholz R.-D., Siebert A., Watson F. G., and Zwitter T., The RAVE survey: constraining the local Galactic escape speed, *MNRAS*, 379:755–772, August 2007.

Springel V., Modelling star formation and feedback in simulations of interacting galaxies, *MNRAS*, 312:859–879, March 2000.

Springel V., The cosmological simulation code GADGET-2, *MNRAS*, 364:1105–1134, December 2005.

Springel V., Smoothed Particle Hydrodynamics in Astrophysics, *ARA&A*, 48:391–430, September 2010.

Springel V. and Hernquist L., Cosmological smoothed particle hydrodynamics simulations: a hybrid multiphase model for star formation, *MNRAS*, 339:289–311, February 2003.

Springel V. and White S. D. M., Tidal tails in cold dark matter cosmologies, *MNRAS*, 307:162–178, July 1999.

Springel V., Di Matteo T., and Hernquist L., Modelling feedback from stars and black holes in galaxy mergers, *MNRAS*, 361:776–794, August 2005.

Sutton E. C., Danchi W. C., Jaminet P. A., and Masson C. R., CO J = 3-2 observations of the neutral disk in Sagittarius A West, *ApJ*, 348:503–514, January 1990.

Tremaine S., Gebhardt K., Bender R., Bower G., Dressler A., Faber S. M., Filippenko A. V., Green R., Grillmair C., Ho L. C., Kormendy J., Lauer T. R., Magorrian J., Pinkney J., and Richstone D., The Slope of the Black Hole Mass versus Velocity Dispersion Correlation, *ApJ*, 574:740–753, August 2002.

van der Kruit P. C. and Searle L., Surface photometry of edge-on spiral galaxies. III - Properties of the three-dimensional distribution of light and mass in disks of spiral galaxies, *A&A*, 110:61–78, June 1982.

Veilleux S., The Starburst-AGN Connection, In L. Tacconi & D. Lutz, editor, *Starburst Galaxies: Near and Far*, page 88, 2001.

Werner M. W., Davidson J. A., Morris M., Novak G., Platt S. R., and Hildebrand R. H., The polarization of the far-infrared radiation from the Galactic center, *ApJ*, 333:729–734, October 1988.

Wild V., Heckman T., and Charlot S., Timing the starburst-AGN connection, *MNRAS*, 405:933–947, June 2010.

Xiang-Grüß M., *Large-scale structure of disc galaxies*, PhD thesis, Christian-Albrechts-Universität zu Kiel, 2009.

Yelda S., Ghez A. M., Lu J. R., Do T., Meyer L., Morris M. R., and Matthews K., Properties of the Remnant Clockwise Disk of Young Stars in the Galactic Center, *ApJ*, 783:131, March 2014.

Yin J., Hou J. L., Prantzos N., Boissier S., Chang R. X., Shen S. Y., and Zhang B., Milky Way versus Andromeda: a tale of two disks, *A&A*, 505:497–508, October 2009.

Zubovas K., Nayakshin S., King A., and Wilkinson M., AGN outflows trigger starbursts in gas-rich galaxies, *MNRAS*, 433:3079–3090, August 2013.

Zylka R., Mezger P. G., Ward-Thompson D., Duschl W. J., and Lesch H., Anatomy of the Sagittarius A complex. 4: SGR A* and the Central Cavity revisited, *A&A*, 297: 83–97, May 1995.

Acknowledgements

I would like to thank all those who have supported me in writing this thesis.
In particular I thank

my advisor Prof. Wolfgang J. Duschl for giving me the opportunity to conduct research on the fascinating field of astronomy, for his pleasant support and the possibility to pursue my goals with a high degree of freedom,

the Kiel astronomy group for continuous entertainment over the last years,

Prof. Mark R. Morris for our excellent collaboration and his hospitality during my stay in Los Angeles,

the UCLA astronomy group for enriching my time in the United States,

Prof. Adam Frank and his group for their support with the usage of the AstroBEAR code,

Peter Scicluna for carefully proof-reading my thesis,

Prof. Ralf Klessen, Prof. Volker Springel and Dr. Meng Xiang-Grüß for making available some of the numerical tools that we used for the calculations presented in this thesis,

and the Fulbright Commission for sponsoring my research visit in the United States.

Erklärung

Hiermit erkläre ich, dass

diese Arbeit - abgesehen von der Beratung durch meinen Betreuer - nach Inhalt und Form die eigene Arbeit ist,

diese Arbeit weder ganz noch zum Teil an anderer Stelle im Rahmen eines Prüfungsverfahrens vorgelegen hat,

Teile dieser Arbeit veröffentlicht wurden: Blank und Duschl (2012), Blank und Duschl (2014); und zur Veröffentlichung vorgesehen sind: Blank und Duschl (2014, in Vorbereitung), Blank et al. (2014, in Vorbereitung)

und dass diese Arbeit unter Einhaltung der Regeln guter wissenschaftlicher Praxis der Deutschen Forschungsgemeinschaft entstanden ist.

Marvin Blank